Cosmic Star-Formation History

Piero Madau[1] and Mark Dickinson[2]

[1]Department of Astronomy and Astrophysics, University of California, Santa Cruz, California 95064; email: pmadau@ucolick.org

[2]National Optical Astronomy Observatory, Tucson, Arizona 85719; email: med@noao.edu

Annu. Rev. Astron. Astrophys. 2014. 52:415–86

First published online as a Review in Advance on June 18, 2014

The *Annual Review of Astronomy and Astrophysics* is online at astro.annualreviews.org

This article's doi:
10.1146/annurev-astro-081811-125615

Keywords

cosmology, galaxy formation, evolution, star formation, stellar populations

Abstract

Over the past two decades, an avalanche of new data from multiwavelength imaging and spectroscopic surveys has revolutionized our view of galaxy formation and evolution. Here we review the range of complementary techniques and theoretical tools that allow astronomers to map the cosmic history of star formation, heavy element production, and reionization of the Universe from the cosmic "dark ages" to the present epoch. A consistent picture is emerging, whereby the star-formation rate density peaked approximately 3.5 Gyr after the Big Bang, at $z \approx 1.9$, and declined exponentially at later times, with an e-folding timescale of 3.9 Gyr. Half of the stellar mass observed today was formed before a redshift $z = 1.3$. About 25% formed before the peak of the cosmic star-formation rate density, and another 25% formed after $z = 0.7$. Less than ∼1% of today's stars formed during the epoch of reionization. Under the assumption of a universal initial mass function, the global stellar mass density inferred at any epoch matches reasonably well the time integral of all the preceding star-formation activity. The comoving rates of star formation and central black hole accretion follow a similar rise and fall, offering evidence for coevolution of black holes and their host galaxies. The rise of the mean metallicity of the Universe to about 0.001 solar by $z = 6$, one Gyr after the Big Bang, appears to have been accompanied by the production of fewer than ten hydrogen Lyman-continuum photons per baryon, a rather tight budget for cosmological reionization.

1. INTRODUCTION

The origin and evolution of galaxies are among the most intriguing and complex chapters in the formation of cosmic structure, and observations in this field have accumulated at an astonishing pace. Multiwavelength imaging surveys with the *Hubble* (HST) and *Spitzer* space telescopes and ground-based facilities, together with spectroscopic follow-up with 8-m-class telescopes, have led to the discovery of galaxies with confirmed redshifts as large as $z = 7.5$ (Finkelstein et al. 2013) as well as compelling photometric candidates as far back as $z \approx 11$ (Coe et al. 2013) when the Universe was only 3% of its current age. Following the seminal work of Steidel et al. (1996), color-selection criteria that are sensitive to the presence of intergalactic HI absorption features in the spectral energy distribution (SED) of distant sources have been used to build increasingly large samples of star-forming galaxies at $2.5 \lesssim z \lesssim 9$ (e.g., Madau et al. 1996, Steidel et al. 2003, Giavalisco et al. 2004a, Bouwens et al. 2011b). Infrared (IR)-optical color selection criteria efficiently isolate both actively star-forming and passively evolving galaxies at $z \approx 2$ (Franx et al. 2003, Daddi et al. 2004). Photometric redshifts have become an unavoidable tool for placing faint galaxies onto a cosmic timeline. *Spitzer*, *Herschel*, and submillimeter telescopes have revealed that dusty galaxies with star-formation rates (SFRs) of order $100\,M_\odot$ year^{-1} or more were abundant when the Universe was only 2–3 Gyr old (Barger et al. 1998, Daddi et al. 2005, Gruppioni et al. 2013). Deep near-infrared (NIR) observations are now commonly used to select galaxies on the basis of their optical rest-frame light and to chart the evolution of the global stellar mass density (SMD) at $0 < z < 3$ (Dickinson et al. 2003). The *Galaxy Evolution Explorer* (GALEX) satellite has quantified the UV galaxy luminosity function (LF) of galaxies in the local Universe and its evolution at $z \lesssim 1$. Ground-based observations and, subsequently, UV and IR data from GALEX and *Spitzer* have confirmed that star-formation activity was significantly higher in the past (Lilly et al. 1996, Le Floc'h et al. 2005, Schiminovich et al. 2005). In the local Universe, various galaxy properties (colors, surface mass densities, and concentrations) have been observed by the Sloan Digital Sky Survey (SDSS) to be "bimodal" around a transitional stellar mass of $3 \times 10^{10}\,M_\odot$ (Kauffmann et al. 2003), showing a clear division between faint, blue, active galaxies and bright, red, passive systems. The number and total stellar mass of blue galaxies appear to have remained nearly constant since $z \sim 1$, whereas those of red galaxies (around L_*) have been rising (Faber et al. 2007). At redshifts $0 < z < 2$ at least, and perhaps earlier, most star-forming galaxies are observed to obey a relatively tight "main-sequence" correlation between their SFRs and stellar masses (Brinchmann et al. 2004, Daddi et al. 2007, Elbaz et al. 2007, Noeske et al. 2007). A minority of starburst galaxies have elevated SFRs above this main sequence as well as a growing population of quiescent galaxies that fall below it.

With the avalanche of new data, galaxy taxonomy has been enriched by the addition of new acronyms such as LBGs, LAEs, EROs, BzKs, DRGs, DOGs, LIRGs, ULIRGs, and SMGs. Making sense of it all and fitting it together into a coherent picture remain one of astronomy's great challenges, in part because of the observational difficulty of tracking continuously transforming galaxy subpopulations across cosmic time and in part because theory provides only a partial interpretative framework. The key idea of standard cosmological scenarios is that primordial density fluctuations grow by gravitational instability driven by cold, collisionless dark matter, leading to a "bottom-up" ΛCDM (cold dark matter) scenario of structure formation (Peebles 1982). Galaxies form hierarchically: Low-mass objects ("halos") collapse earlier and merge to form increasingly larger systems over time—from ultrafaint dwarfs to clusters of galaxies (Blumenthal et al. 1984). Ordinary matter in the Universe follows the dynamics dictated by the dark matter until radiative, hydrodynamic, and star-formation processes take over (White & Rees 1978). The "dark side" of galaxy formation can be modeled with high accuracy and has been explored in detail

through *N*-body numerical simulations of increasing resolution and size (e.g., Davis et al. 1985; Dubinski & Carlberg 1991; Moore et al. 1999; Springel et al. 2005, 2008; Diemand et al. 2008; Stadel et al. 2009; Klypin et al. 2011). However, the same does not hold for the baryons. Several complex processes are still poorly understood, for example, baryonic dissipation inside evolving CDM halos, the transformation of cold gas into stars, the formation of disks and spheroids, the chemical enrichment of gaseous material on galactic and intergalactic scales, and the role played by "feedback" [the effect of the energy input from stars, supernovae (SNe), and massive black holes on their environment] in regulating star formation and generating galactic outflows. The purely phenomenological treatment of complex physical processes that is at the core of semianalytic schemes of galaxy formation (e.g., White & Frenk 1991, Kauffmann et al. 1993, Somerville & Primack 1999, Cole et al. 2000) and—at a much higher level of realism—the "subgrid modeling" of star formation and stellar feedback that must be implemented even in the more accurate cosmological hydrodynamic simulations (e.g., Katz et al. 1996, Yepes et al. 1997, Navarro & Steinmetz 2000, Springel & Hernquist 2003, Keres et al. 2005, Ocvirk et al. 2008, Governato et al. 2010, Guedes et al. 2011, Hopkins et al. 2012, Kuhlen et al. 2012, Zemp et al. 2012, Agertz et al. 2013) are sensitive to poorly determined parameters and suffer from various degeneracies, a weakness that has traditionally prevented robust predictions to be made in advance of specific observations.

Ideally, an in-depth understanding of galaxy evolution would encompass the full sequence of events that led from the formation of the first stars after the end of the cosmic dark ages to the present-day diversity of forms, sizes, masses, colors, luminosities, metallicities, and clustering properties of galaxies. This is a daunting task, and it is perhaps not surprising that an alternative way to look at and interpret the bewildering variety of galaxy data has become very popular in the past two decades. The method focuses on the emission properties of the galaxy population as a whole, traces the evolution with cosmic time of the galaxy luminosity density from the far-UV (FUV) to the far-infrared (FIR), and offers the prospect of an empirical determination of the global history of star formation and heavy element production of the Universe, independently of the complex evolutionary phases of individual galaxy subpopulations. The modern version of this technique relies on some basic properties of stellar populations and dusty starburst galaxies:

1. The UV-continuum emission in all but the oldest galaxies is dominated by short-lived massive stars. Therefore, for a given stellar initial mass function (IMF) and dust content, it is a direct measure of the instantaneous star-formation rate density (SFRD).
2. The rest-frame NIR light is dominated by near-solar-mass-evolved stars that make up the bulk of a galaxy's stellar mass and can then be used as a tracer of the total SMD.
3. Interstellar dust preferentially absorbs UV light and reradiates it in the thermal IR, so that the FIR emission of dusty starburst galaxies can be a sensitive tracer of young stellar populations and the SFRD.

By modeling the emission history of all stars in the Universe at UV, optical, and IR wavelengths from the present epoch to $z \approx 8$ and beyond, one can then shed light on some key questions in galaxy formation and evolution studies: Is there a characteristic cosmic epoch of the formation of stars and heavy elements in galaxies? What fraction of the luminous baryons observed today were already locked into galaxies at early times? Are the data consistent with a universal IMF? Do galaxies reionize the Universe at a redshift greater than 6? Can we account for all the metals produced by the global star-formation activity from the Big Bang to the present? How does the cosmic history of star formation compare with the history of mass accretion onto massive black holes as traced by luminous quasars?

This review focuses on the range of observations, methods, and theoretical tools that are allowing astronomers to map the rate of transformation of gas into stars in the Universe, from the cosmic dark ages to the present epoch. Given the limited space available, it is impossible to provide a thorough survey of such a huge community effort without leaving out significant contributions or whole subfields. We have therefore tried to refer only briefly to earlier findings and present recent observations in more detail, limiting the number of studies cited and highlighting key research areas. In doing so, we hope to provide a manageable overview of how the field has developed and matured in line with new technological advances and theoretical insights and of the questions with which astronomers still struggle nowadays.

The remainder of this review is organized as follows: The equations of cosmic chemical evolution that govern the consumption of gas into stars and the formation and dispersal of heavy elements in the Universe as a whole are given in Section 2. We turn to the topic of measuring mass from light and draw attention to areas of uncertainty in Section 3. Large surveys, key data sets, and the analyses thereof are highlighted in Section 4. An up-to-date determination of the star-formation history (SFH) of the Universe is provided and its main implications are discussed in Section 5. Finally, we summarize our conclusions in Section 6. Unless otherwise stated, all results presented here will assume a "cosmic concordance cosmology" with parameters $(\Omega_M, \Omega_\Lambda, \Omega_b, h) = (0.3, 0.7, 0.045, 0.7)$.

2. THE EQUATIONS OF COSMIC CHEMICAL EVOLUTION

To pursue and cast light into a quantitative form of the idea of a history of cosmic star formation and metal enrichment—not of any particular type of galaxy but of the Universe as a whole—it is useful to start by generalizing the standard equations of galaxy evolution (Tinsley 1980) over all galaxies and intergalactic gas in the Universe. In a representative cosmological comoving volume with density ρ_* in long-lived stars and stellar remnants (white dwarfs, neutron stars, black holes) and gas density ρ_g and in which new stars are formed at the rate ψ, the equations of cosmic chemical evolution can be written as

$$\begin{aligned} \frac{\mathrm{d}\rho_*}{\mathrm{d}t} &= (1-R)\psi \\ \frac{\mathrm{d}\rho_g}{\mathrm{d}t} &= -\frac{\mathrm{d}\rho_*}{\mathrm{d}t} \\ \rho_g \frac{\mathrm{d}Z}{\mathrm{d}t} &= y(1-R)\psi. \end{aligned} \tag{1}$$

Here, Z is the metallicity in the gas and newly born stars, R is the "return fraction" or the mass fraction of each generation of stars that is put back into the interstellar medium (ISM) and intergalactic medium (IGM), and y is the net metal yield or the mass of new heavy elements created and ejected into the ISM/IGM by each generation of stars per unit mass locked into stars. The above equations govern the formation, destruction, and distribution of heavy elements as they cycle through stars and are ultimately dispersed into the ISM/IGM. By treating all galaxies as a single stellar system and all baryons in the ISM/IGM as its gas reservoir, their solution enables the mean trends of galaxy populations to be calculated with the fewest number of free parameters. The equations state that, for every new mass element locked forever into long-lived stars and stellar remnants, $\Delta\rho_*$, the metallicity of the ISM/IGM increases as $\Delta Z = y\Delta\rho_*/\rho_g$, whereas the mass of heavy elements in the ISM/IGM changes as $\Delta(Z\rho_g) = (y - Z)\Delta\rho_*$. The latter expression is a consequence of metals being released into the gas from mass loss during post-main-sequence stellar evolution as well as being removed from the ISM/IGM when new stars condense out.

However, compared with the source term, the metal sink term can be neglected at early epochs when $Z \ll y$.

At redshift z, Equation 1 can be integrated to give the following:

1. The total mass density of long-lived stars and stellar remnants accumulated from earlier episodes of star formation,

$$\rho_*(z) = (1-R)\int_0^{t(z)} \psi \, \mathrm{d}t = (1-R)\int_z^{\infty} \psi \frac{\mathrm{d}z'}{H(z')(1+z')},$$
$$\rho_*(z) = (1-R)\int_0^{t(z)} \psi \, \mathrm{d}t = (1-R)\int_z^{\infty} \psi \frac{\mathrm{d}z'}{H(z')(1+z')}, \quad (2)$$

   where $H(z') = H_0[\Omega_M(1+z')^3 + \Omega_\Lambda]^{1/2}$ is the Hubble parameter in a flat cosmology.
2. The total mass density of gas,

$$\rho_g(z) = \rho_{g,\infty} - \rho_*(z), \quad (3)$$

   where $\rho_{g,\infty}$ is the comoving density of gas at some suitable high redshift where there are no stars or heavy elements.
3. The total mass density of heavy elements in the ISM/IGM,

$$Z(z)\rho_g(z) = y(1-R)\int_0^{t(z)} \psi \, \mathrm{d}t - (1-R)\int_0^{t(z)} Z\psi \, \mathrm{d}t$$
$$\equiv [y - \langle Z_*(z)\rangle]\rho_*(z), \quad (4)$$

   where the term $\langle Z_*\rangle\rho_*$ is the total metal content of stars and remnants at that redshift. Note that the instantaneous total metal ejection rate, E_Z, is the sum of a recycle term and a creation term (Maeder 1992),

$$E_Z = ZR\psi + y(1-R)\psi, \quad (5)$$

   where the first term is the amount of heavy elements initially lost from the ISM when stars formed that are now being rereleased, and the second represents the new metals synthesized by stars and released during mass loss.

For a given universal stellar IMF, the quantities R and y can be derived using the following formulas:

$$R = \int_{m_0}^{m_u} (m - w_m)\phi(m)\mathrm{d}m \quad (6)$$

$$y(1-R) = \int_{m_0}^{m_u} m y_m \phi(m)\mathrm{d}m, \quad (7)$$

where m is mass of a star, w_m is its remnant mass, $\phi(m)$ is the IMF [normalized so that $\int_{m_l}^{m_u} m\phi(m)\mathrm{d}m = 1$], and y_m is the stellar yield, i.e., the fraction of mass m that is converted to metals and ejected. (In this review, the term "yield" generally indicates the net yield y of a stellar population as defined in Equation 7; instead, we explicitly speak of "stellar yields" to indicate the y_m resulting from nucleosynthesis calculations.) The above equations have been written under the simplifying assumptions of "instantaneous recycling" (where the release and mixing of the products of nucleosynthesis by all stars more massive than m_0 occur on a timescale that is much shorter than the Hubble time, whereas stars with $m < m_0$ live forever), "one zone" (where the heavy elements are well mixed at all times within the volume under consideration), "closed box" (flows of gas in and out of the chosen volume are negligible), and "constant IMF and metal yield."

Recall now that the main-sequence timescale is shorter than 0.6 Gyr (the age of the Universe at $z = 8.5$) for stars more massive than $2.5\,M_\odot$, whereas stars less massive than $0.9\,M_\odot$ never

evolve off the main sequence. [Stellar evolutionary models by Schaller et al. (1992) show that, for $m < 7\,M_\odot$, solar-metallicity stars have longer lifetimes than their metal-poor counterparts, whereas the opposite is true for $m > 9\,M_\odot$.] So over the redshift range of interest here, the instantaneous recycling approximation may break down in the limited mass range $0.9 < m < 2.5\,M_\odot$. For illustrative purposes, in the following we adopt the initial-final mass values for white dwarfs tabulated by Weidemann (2000), which can be fit to few-percent accuracy over the interval $1\,M_\odot < m < 7\,M_\odot$ as $w_m = 0.444 + 0.084m$. We also assume that all stars with $8\,M_\odot < m < m_{BH} = 40\,M_\odot$ return all but a $w_m = 1.4\,M_\odot$ remnant, and stars above m_{BH} collapse to black holes without ejecting material into space, i.e., $w_m = m$. Few stars form with masses above $40\,M_\odot$, so the impact of the latter simplifying assumption on chemical evolution is minimal. Thus, taking $m_0 = 1\,M_\odot$ as the dividing stellar mass for instantaneous recycling and a Salpeter (1955) IMF with $\phi(m) \propto m^{-2.35}$ in the range $m_l = 0.1\,M_\odot < m < m_u = 100\,M_\odot$, one derives a return fraction of $R = 0.27$. Under the same assumptions, a Chabrier (2003) IMF,

$$\phi(m) \propto \begin{cases} e^{-(\log m - \log m_c)^2/2\sigma^2}/m & (m < 1\,M_\odot) \\ m^{-2.3} & (m > 1\,M_\odot) \end{cases} \quad (8)$$

(with $m_c = 0.08\,M_\odot$ and $\sigma = 0.69$) is more weighted toward short-lived massive stars and yields a larger return fraction, $R = 0.41$. In the instantaneous recycling approximation, the fraction of "dark" stellar remnants formed in each generation is

$$D = \int_{m_0}^{m_u} w_m \phi(m) \mathrm{d}m. \quad (9)$$

The two IMFs produce a dark remnant mass fraction of $D = 0.12$ and $D = 0.19$, respectively. The stellar nucleosynthetic yields depend on metallicity, rotation, and the mass limit for black hole formation m_{BH}. By integrating over the IMF the subsolar metallicity stellar yields (where the effect of mass loss is negligible) tabulated by Maeder (1992) from $10\,M_\odot$ to $m_{BH} = 40\,M_\odot$, we obtain $y = 0.016$ for a Salpeter and $y = 0.032$ for a Chabrier IMF. When integrated to $m_{BH} = 60\,M_\odot$, the same tabulation implies $y = 0.023$ (with $R = 0.29$) and $y = 0.048$ (with $R = 0.44$) for a Salpeter and Chabrier IMF, respectively. Notice that some of the uncertainties associated with the IMF and the mass cutoff m_{BH} become smaller when computing the term $y(1 - R)$ in the equations (Equation 1). For massive stars at solar metallicities, stellar winds eject large amounts of helium and carbon into the ISM before these are processed into heavier elements, but the effect on the integrated metal yields ($10-40\,M_\odot$) is weak (Maeder 1992). Total stellar yields (including the wind and pre-SN contributions) obtained from rotating stellar models at solar metallicity have been presented by Hirschi et al. (2005). Over the same range $10-40\,M_\odot$, in this case we derive $y = 0.019$ for Salpeter and $y = 0.038$ for Chabrier. For comparison, the zero-metallicity stellar yields of Chieffi & Limongi (2004) imply $y = 0.015$ for Salpeter and $y = 0.030$ for Chabrier.

Although disfavored by many observations, a Salpeter IMF in the mass range $0.1-100\,M_\odot$ is used as a reference throughout the rest of this review. Similarly, for consistency with prior work, we assume the canonical metallicity scale where solar metallicity is $Z_\odot = 0.02$, rather than the revised value $Z_\odot = 0.014$ of Asplund et al. (2009).

3. MEASURING MASS FROM LIGHT

Fundamentally, deriving the history of star formation in galaxies involves inferring mass from light. We observe the emission from galaxies at various wavelengths, and from those measurements, we try to infer either the rates at which the galaxies are forming stars or their integrated stellar masses. **Figure 1** illustrates the sensitivity of today's premier multiwavelength surveys to the SFRs and

stellar masses of galaxies at high redshift. Rest-frame UV, IR, submillimeter and radio emission, as well as nebular lines such as Hα are all used to measure SFRs and are discussed in this section. In the absence of extinction, UV measurements are more sensitive than current IR or radio data by orders of magnitude, but in practice, dust attenuation is often severe. Long-wavelength data are essential to gain a comprehensive picture of cosmic star formation but are limited by current instrumental sensitivities, although ALMA (Atacama Large Millimeter Array) enables dramatic improvements at submillimeter wavelengths that are particularly valuable at higher redshifts. NIR to mid-infrared (MIR) measurements are critical for deriving stellar masses. Their sensitivity to stellar mass depends critically on the mass-to-light ratio of the stellar population in a distant galaxy, hence on its age, SFH, and extinction. **Figure 1*b*** illustrates two limiting cases: a maximum-*M/L* model defined as a passively evolving stellar population as old as the Universe and a minimum-*M/L* model defined as a very young, unreddened, actively star-forming galaxy. In principle, surveys should be mass-complete to the maximum-*M/L* limits. Much less massive galaxies with young, low-*M/L* stellar populations can easily be detected, but observations would miss dusty or evolved galaxies with lower masses. The HST WFC3 camera has significantly improved NIR sensitivity compared with most ground-based imaging, but it samples only optical rest-frame light at $z < 3$. *Spitzer*'s IRAC remains the premier resource for deriving stellar masses at higher redshifts, and *James Webb Space Telescope* (JWST) will provide a major advance.

The conversions from light to mass are derived or calibrated using stellar population synthesis models, which encode our knowledge of stellar evolution and of the SEDs of stars, and compute the emergent spectrum for a galaxy with given properties. This knowledge is imperfect, although astronomers have made great progress developing population synthesis models and improving the libraries of empirical and theoretical stellar spectra that they use (for a recent review, see Conroy 2013).

A galaxy (or the Universe as a whole) consists of stars that span a wide range of masses, ages, and metal abundances. The light from those stars may be attenuated by dust before it emerges from the galaxy; the dust dims and generally reddens the galaxy spectrum, and the heated dust re-emits energy in the IR. A galaxy spectrum arises from a composite stellar population whose true distribution of properties is generally unknown. For nearby galaxies, resolved color-magnitude diagrams can reveal the actual distributions of stellar properties, but for most galaxies, we can observe only their integrated light and properties of the emergent spectrum (particularly broadband colors) are often degenerate to different intrinsic properties. An often-noted example is the degeneracy between age, metallicity, and dust attenuation, all of which can redden the spectrum of a galaxy. Observations at higher spectral resolution, for example, of individual spectral lines, can help to resolve some degeneracies (e.g., to constrain stellar metallicities, population ages from absorption line strengths, or reddening from emission line ratios), but never all: The inherently composite nature of stellar populations requires that we make simplifying assumptions when interpreting the light, assumptions that generally cannot be uniquely tested for individual galaxies. Examples of such assumptions include the form of the IMF, the stellar metallicity distribution, the wavelength dependence of dust attenuation, or the precise SFH of the galaxy. The hope is that these assumptions can be made as reasonably as possible, that their impact on derived masses or SFRs can be estimated, and that ultimately they may be tested or constrained by observations in various ways.

The IMF underlies the relation between mass, light, and stellar population age. It controls the ratio of hot, bright stars that dominate the light to cool, faint stars that usually dominate the mass. It regulates the luminosity and color evolution of the integrated stellar population, as stars with different masses evolve at different rates. It also affects the time evolution of the integrated stellar mass, which changes as more massive stars lose gas to the ISM via winds or detonate as SNe.

It is essentially impossible to constrain the IMF from photometric measurements of the integrated light from galaxies: The color of a galaxy does not uniquely reveal its underlying IMF, as there are too many degeneracies to permit useful constraints. Even detailed spectroscopy does not usually offer strong constraints on the IMF overall, although certain spectral features can be useful diagnostics of the number of stars in a given mass range (e.g., Leitherer et al. 1999). The most direct constraints on the IMF come from counting stars as a function of mass in resolved, nearby stellar populations, but they must be very nearby (within our Galaxy and its satellites) to detect subsolar dwarf stars that dominate the mass of a stellar system. The next-best constraints come from integrated measurements of the mass-to-light ratio for star clusters or galaxies, using kinematics (velocity dispersions or rotation curves) to derive a mass for comparison to the luminosity. However, these measurements are difficult to make for faint galaxies at high redshift and require careful modeling to account for the role of dark matter and many other effects.

For lack of better information, astronomers often assume that the IMF is universal, with the same shape at all times and in all galaxies. Although the IMF of various stellar populations within the Milky Way appears to be invariant (for a review, see Bastian et al. 2010), recent studies suggest that the low-mass IMF slope may be a function of the global galactic potential, becoming increasingly shallow (bottom light) with decreasing galaxy velocity dispersion (Conroy & van Dokkum 2012, Geha et al. 2013). It is still unknown, however, how galaxy to galaxy variations may affect the "cosmic" volume-averaged IMF as a function of redshift. In Section 5, we see how a universal IMF can provide a reasonably consistent picture of the global SFH. The exact shape of the IMF at low stellar masses is fairly unimportant for deriving relative stellar masses or SFRs for galaxies. Low-mass stars contribute most of the mass but almost none of the light and do not evolve over a

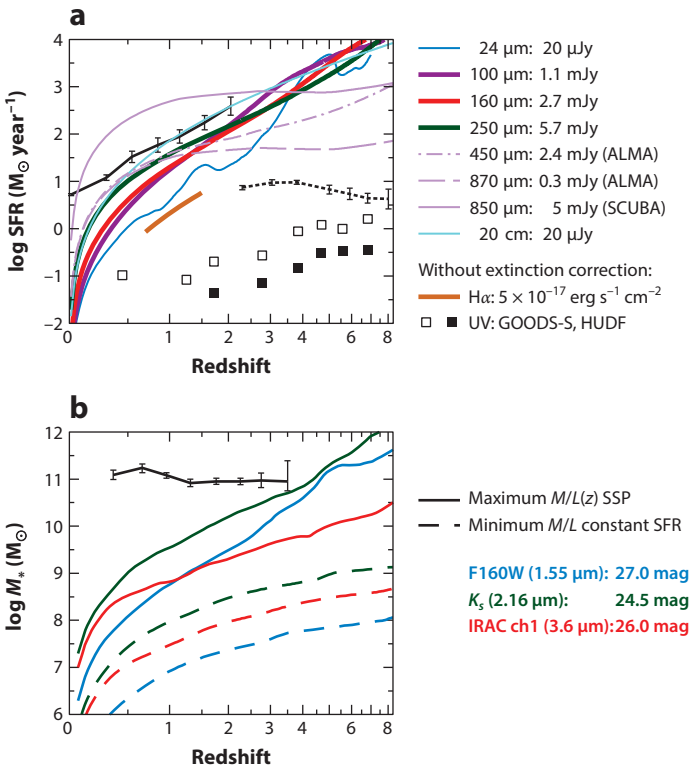

Hubble time. Therefore, changing the low-mass IMF mainly rescales the mass-to-light ratio *M/L* and, hence, affects both stellar masses and SFRs derived from photometry to a similar degree. Changes to the intermediate- and high-mass region of the IMF, however, can have significant effects on the luminosity, color evolution, and the galaxy properties derived from photometry. It is quite common to adopt the simple power-law IMF of Salpeter (1955), truncated over a finite mass range (generally, 0.1 to 100 $M_\odot$, as adopted in this review). However, most observations show that the actual IMF turns over from the Salpeter slope at masses $<1\,M_\odot$, resulting in smaller *M/L* ratios than those predicted by the Salpeter IMF. Some common versions of such an IMF are the broken power-law representation used by Kroupa (2001) and the log-normal turnover suggested by Chabrier (2003).

Dust extinction is another important effect that must often be assumed or inferred, rather than directly measured. The shape of the extinction law depends on the properties of the dust grains causing the extinction. For observations of a single star, photons may be absorbed by dust or scattered out of the observed sightline. However, galaxies are 3D structures with mixed and varying distributions of stars and dust. Photons may be scattered both into and out of the sightline, and the optical depth of dust along the line of sight to the observer will be different for every star in the galaxy. These effects are generally lumped together into the simplifying assumption of a net dust

Figure 1

(*a*) Sensitivity to star formation versus redshift for deep survey data at various wavelengths. The key at right indicates the wavelengths and the corresponding flux limits. Most of these limits were computed using data available in the GOODS fields or are simply chosen to be representative values for very deep surveys. For ALMA, we use projected sensitivities of the completed interferometer for modest 10-min integration times, noting that the small ALMA primary beam at 870 μm and 450 μm requires approximately 50 and 170 pointings, respectively, to map 1 square arcminute with uniform sensitivity. All conversions to star-formation rate (SFR) assume a Salpeter IMF from 0.1 to 100 $M_\odot$. The limits for mid-IR (*Spitzer*), far-IR (*Herschel*), submillimeter, and radio data use bolometric corrections from the observed wavelength based on spectral energy distribution templates by Magdis et al. (2012). Open square points show rest-frame 1,500-Å sensitivities assuming no extinction; in practice, dust attenuation can significantly increase these limits. The open squares are based on GOODS data from GALEX, ground-based *U*-band (Nonino et al. 2009), and HST ACS and WFC3 (CANDELS), whereas the filled square points show HST ACS and WFC3 limits for the HUDF (Bouwens et al. 2011b). The Hα curve shown here represents the typical limiting sensitivity of the 3D-HST IR grism spectroscopic survey (Brammer et al. 2012), again assuming no extinction, with conversion to SFR from Kennicutt (1998). The data points (shown as error bars) connected by a solid line show the SFR corresponding to the characteristic infrared luminosity L_*(IR) from Magnelli et al. (2013), and the points connected by a dotted line show the SFR corresponding to the characteristic FUV luminosity L_*(FUV) for Lyman break galaxies at $2 < z < 8$, uncorrected for extinction (Reddy & Steidel 2009; Bouwens et al. 2012b). (*b*) Sensitivity to stellar mass versus redshift, for flux limits at several wavelengths, as indicated at right. The solid curves assume a passively evolving simple stellar population with the age of the Universe, solar metallicity, a Salpeter IMF, and no extinction, computed using the models of Conroy et al. (2009). This approximates the maximum mass-to-light ratio potentially visible at any redshift and, hence, provides an upper bound to the mass completeness limit for a given survey. Less massive galaxies can easily be detected, however, if they have young stellar populations. The dashed curves show sensitivities for an unreddened galaxy with a constant SFR and age of 10^7 years, when *M/L* at these wavelengths reaches a minimum value. The IR sensitivity limits (given in AB magnitudes) are chosen to be representative of deep surveys such as GOODS and CANDELS [e.g., K_s data from Retzlaff et al. (2010) or Wang et al. (2010)], but are not specific to a particular data set. The data points (shown as error bars) connected by a solid line show the characteristic stellar mass M_* at redshifts $0.2 < z < 4$ (Ilbert et al. 2013). Abbreviations: 3D, three-dimensional; ACS, Advanced Camera for Surveys; ALMA, Atacama Large Millimeter Array; GALEX, *Galaxy Evolution Explorer*; GOODS, Great Observatories Origins Deep Survey; HST, *Hubble Space Telescope*; HUDF, Hubble Ultradeep Field; IMF, initial mass function; IR, infrared; SFR, star-formation rate; SSP, simple stellar population.

attenuation curve, and such relations have been derived for local galaxy samples both empirically (e.g., Calzetti et al. 2000) and using theoretical modeling (Charlot & Fall 2000). However, all galaxies are not equal, and no net attenuation law is equally appropriate for all galaxies. There can always be stars that are completely obscured behind optically thick dust such that little or none of their light emerges directly from the galaxy, except reradiated as dust emission. Although this may not be a significant factor for many galaxies, there are certainly some starburst galaxies in which huge and bolometrically dominant star-formation activity takes place in regions screened by hundreds of magnitudes of dust extinction. UV/optical measurements will never detect this light, but the star formation can be detected and measured at other wavelengths, e.g., with FIR or radio data.

To derive star formation rates or stellar masses for galaxies using stellar population synthesis models, astronomers typically assume relatively simple, parameterized SFHs. However, the SFHs of individual galaxies are unlikely to be smooth and simple; they may vary on both long and short timescales. The fact that young stars are more luminous than older stars leads to the problem of "outshining" (e.g., Papovich et al. 2001, Maraston et al. 2010)—the light from older stars can be lost in the glare of more recent star formation and contributes relatively little to the observed photometry from a galaxy, even if those stars contribute significantly to its mass. SED model fits to galaxies with recent star formation tend to be driven largely by the younger, brighter starlight and may not constrain the mass (or other properties) of older stars that may be present.

For the Universe as a whole, there is one "cosmic" IMF that represents the global average at a given time or redshift, regardless of whether the IMF varies from one galaxy to another. Similarly, there is a "cosmic" distribution of metallicities, a "cosmic" net attenuation of starlight by dust at a given wavelength, and the Universe as a whole obeys one "cosmic" SFH that, moreover, was probably relatively smooth over time—i.e., any stochasticity or "burstiness" averages out when considered for the Universe as a whole. In principle, these facts can simplify the determination of the cosmic SFH, particularly when it is derived from measurements of integrated light averaging over all galaxies. In practice, however, astronomers often derive SFRs and stellar masses for individual galaxies in their deep surveys and then sum them to derive comoving volume averages. In that case, some of the advantages of the "cosmic averaging" are reduced.

3.1. Star-Formation Rates

There are many ways in which to infer SFRs from observations of the integrated light from galaxies. Kennicutt (1998) and Kennicutt & Evans (2012) have presented extensive reviews of this topic, and here we recap only points that are especially relevant for measurements of the global SFH, particularly at high redshift. Virtually all observational tracers of star formation fundamentally measure the rate of massive star formation, because massive stars emit most of the energy from a young stellar population. However, different observational tracers are sensitive to different ranges of stellar masses; hence, they respond differently as a function of stellar population age. For example, Hα emission arises primarily from HII regions photoionized by O stars with lifetimes shorter than 20 Myr, whereas the UV continuum is produced by stars with a broader mass range and with longer lifetimes. The time dependence of different indicators can complicate efforts to derive accurate SFRs for individual galaxies, especially if their SFRs may be rapidly changing (e.g., during a starburst event), but they should average out when summing over a whole population of galaxies.

3.1.1. UV light. Newly formed stellar populations emit radiation over a broad spectrum. For a normal IMF, low-mass stars dominate the mass integrated over the whole stellar population, but at young ages, the luminosity is dominated by UV emission from massive stars. These stars have

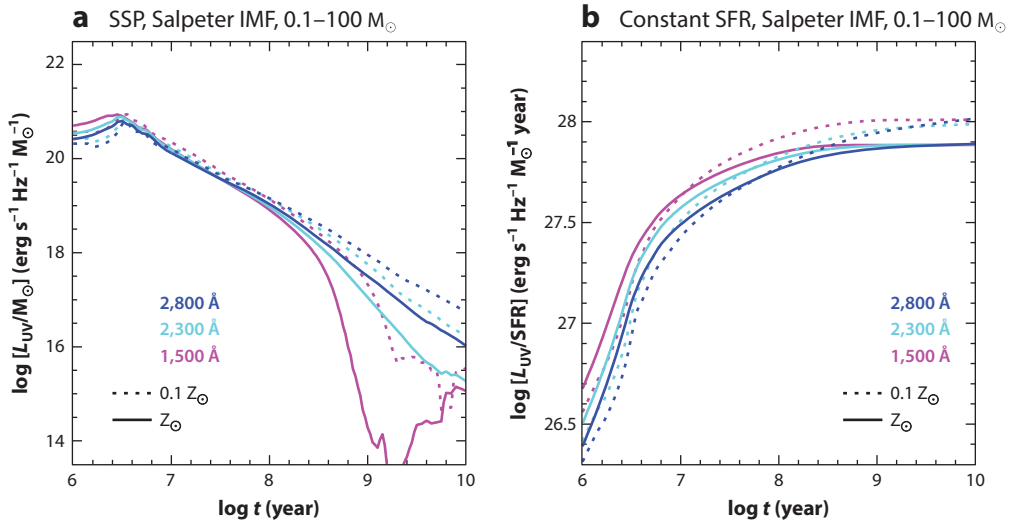

Figure 2

(*a*) Time dependence of the UV luminosity of an SSP with initial mass 1 $M_\odot$, formed with a Salpeter IMF in the range 0.1–100 $M_\odot$, measured at three wavelengths, 1,500 Å, 2,300 Å, and 2,800 Å, and computed with the stellar population synthesis models of Conroy et al. (2009): (*solid lines*) solar metallicity ($Z = 0.02$), (*dashed lines*) 1/10 solar metallicity ($Z_* = 0.002$). (*b*) Time dependence of the UV luminosity per unit SFR for a model with a constant SFR, shown for the same UV wavelengths and metallicities as in the left panel. Abbreviations: IMF, initial mass function; SFR, star-formation rate; SSP, simple stellar population.

short lifetimes, so the UV emission fades quickly. For a Salpeter IMF, the 1,500-Å luminosity from an evolving simple stellar population (SSP) (i.e., an ensemble of stars formed instantaneously and evolving together) with solar metallicity fades by a factor of 100 after 10^8 years and by factors of 10^3 to 10^6 after 10^9 years, depending on metallicity (**Figure 2**). Bolometrically, at least half of the luminous energy that an SSP produces over a 10-Gyr cosmic lifetime emerges in the first 100 Myr, mostly in the UV, making this a natural wavelength from which to infer SFRs.

For a galaxy forming stars at a constant rate, the 1,500-Å luminosity stabilizes once O stars start to evolve off the main sequence. For solar metallicity, by an age of $10^{7.5}$ years, the 1,500-Å luminosity has reached 75% of its asymptotic value, although convergence is somewhat slower at lower metallicity (**Figure 2**). For these reasons, the UV luminosity at wavelengths of ∼1,500 Å (wavelengths from 1,400 Å to 1,700 Å have been used in the literature for both local and high-redshift studies) is regarded as a good tracer of the formation rate of massive stars, provided that the timescale for significant fluctuations in the SFR is longer than a few 10^7 years. For shorter bursts or dips in the SFR, changes in the UV continuum flux may lag those in the SFR and smooth over such variations.

Although the 1,500-Å rest frame is readily accessible with ground-based optical observations of galaxies at redshifts $z \gtrsim 1.4$, measurements at lower redshifts require space-based UV data (e.g., from GALEX or HST) or are limited to longer UV wavelengths. Mid-UV reference wavelengths that have been used in the literature include 2,300 Å (the approximate central wavelength of the GALEX near-UV passband) and 2,800 Å (used, e.g., by Lilly et al. 1996). The mid-UV emission from a galaxy can have a larger contribution from longer-lived, lower-mass stars, particularly at later ages, and the time evolution of the luminosity is more gradual. This is particularly true after ∼250 Myr, when the 1,500-Å luminosity of an SSP drops off sharply, whereas the 2,800-Å luminosity continues to fade at an approximately exponential rate (**Figure 2**). For a constant

SFR, the UV spectral slope reddens moderately with time, as the 1,500-Å luminosity reaches a steady-state level earlier, whereas longer-lived (B and A) stars continue to build up and contribute to the 2,800-Å luminosity. This complicates the conversion from luminosity to SFR as well as any correction for dust extinction based on the UV spectral slope. Still, for young ages, both shorter and longer UV wavelengths usefully trace the SFR and have been used extensively in the literature. Moreover, longer UV wavelengths are subject to somewhat lesser dust attenuation. Wavelengths shorter than that of Lyα (1,216 Å) are rarely used to estimate SFRs, particularly at high redshift where absorption from neutral hydrogen in the IGM is strong.

The UV luminosity output by a stellar population also depends on its metallicity, which affects stellar temperatures and line blanketing. Generally speaking, less-metal-rich stars produce more UV light. The amplitude of this effect is not insignificant and depends on the details of the SFH. From a Salpeter IMF and constant SFR, the range of FUV luminosity per unit SFR for stars spanning a factor of 100 in metallicity (from $Z = 0.0003$ to 0.03) is less than 0.24 dex, or 70%. These variations are larger at higher metallicities and older ages; therefore, we may expect significant evolution in the $L_{\rm FUV}$ to the SFR conversion factor as the global metallicity of galaxies evolves.

We express the conversion factor between the intrinsic FUV-specific luminosity L_ν(FUV) (before extinction or corrected for extinction) and the ongoing SFR as

$$\mathrm{SFR} = \mathcal{K}_{\rm FUV} \times L_\nu(\mathrm{FUV}), \tag{10}$$

where L_ν(FUV) is expressed in units of erg s^{-1} Hz^{-1} and SFR in units of M$_\odot$ year^{-1}. The precise value of the conversion factor $\mathcal{K}_{\rm FUV}$ is sensitive to the recent SFH and metal-enrichment history as well as to the choice of IMF. It is relatively insensitive to the exact FUV wavelength, as the UV spectrum of a galaxy with a constant SFR is quite flat in f_ν units, at least for ages much longer than 10^7 years. Generally in this review, we use FUV to refer to 1,500-Å emission or are explicit when we refer to other UV wavelengths. For a Salpeter IMF in the mass range $0.1-100\,\mathrm{M}_\odot$ and constant SFR, the flexible stellar population synthesis (FSPS) models of Conroy et al. (2009) yield $\mathcal{K}_{\rm FUV} = (1.55, 1.3, 1.1, 1.0) \times 10^{-28}$ for $\log Z_*/Z_\odot = (+0.2, 0, -0.5, -1.0)$ at age $\gtrsim$300 Myr. The GALAXEV models of Bruzual & Charlot (2003) yield values of $\mathcal{K}_{\rm FUV}$ that are ~5% smaller.

Figure 3 illustrates the combined effects of the evolution of the global SFR and metal density on the global mean UV-to-SFR conversion factor as a function of redshift on the basis of the FSPS models. Concentrating on the FUV behavior at 1,500 Å for constant $\psi(z)$, the conversion factor is nearly constant, though slightly elevated at the highest redshifts as the cosmic age gets young, particularly for lower-metallicity models. A SFH that increases with time from $z = 12$ to 1.7, so that the UV-emitting population is on average younger over that redshift range, leads to a more gradually declining trend in $\mathcal{K}_{\rm FUV}(z)$ with time. The dashed line incorporates one scenario for a global change in the metallicity of the star-forming population, evolving as $Z_* = Z_\odot 10^{-0.15z}$ (Kewley & Kobulnicky 2007). This particular evolution is only moderately well constrained at lower redshifts and should be taken as illustrative only, but we may certainly expect metallicities to be lower on average at higher redshift. The effects of metallicity dominate over those of age in this scenario, but the two counterbalance each other to a certain degree, so that $\mathcal{K}_{\rm FUV}(z)$ changes by less than 20%. At 2,800 Å, the redshift dependence of $\mathcal{K}_{\rm FUV}(z)$ is stronger, particularly at $z < 2$ as the global SFRD declines with time, although this may be partially canceled by the effects of metallicity evolution. This is an example of why shorter FUV wavelengths should be preferred for deriving galaxy SFRs.

In this review, we adopt a constant FUV conversion factor $\mathcal{K}_{\rm FUV} = 1.15 \times 10^{-28}\,\mathrm{M}_\odot$ year^{-1} erg^{-1} s Hz (we typically leave out the units) as a compromise value based on the evolutionary scenario from **Figure 3**. The widely used value from Kennicutt (1998) (and based on the calibration by Madau et al. 1998b), $\mathcal{K}_{\rm FUV} = 1.4 \times 10^{-28}$, is 20% larger than our calibration. Other recent

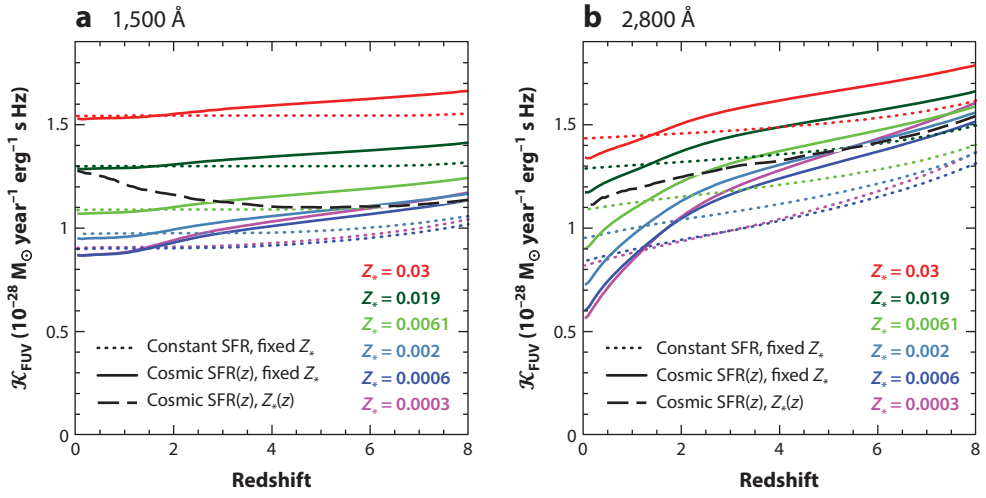

Figure 3

Age and metallicity dependence of the SFR to UV luminosity ratio ($= \mathcal{K}$) (Equation 10) for a stellar population with a Salpeter IMF in the range 0.1–100 $M_\odot$, using the spectral population synthesis models of Conroy et al. (2009): (*dotted lines*) $\mathcal{K}_{FUV}(z)$ assuming constant SFR (starting at $z = 12$) and fixed stellar metallicity; (*solid lines*) same assuming the functional form for cosmic SFR density given in Equation 15 (again starting at $z = 12$) and fixed stellar metallicity; (*dashed lines*) same assuming the functional form for cosmic SFR density given in Equation 15 (again starting at $z = 12$) and stellar metallicity evolving as $Z_* = Z_\odot 10^{-0.15z}$ (Kewley & Kobulnicky 2007). This relation is shown at (*a*) 1,500 Å and (*b*) 2,800 Å, respectively. Abbreviations: IMF, initial mass function; SFR, star-formation rate.

analyses based on the GALAXEV libraries have also found lower mean conversion factors, for both low- and high-redshift galaxy populations (e.g., Salim et al. 2007, Haardt & Madau 2012). The FUV conversion tabulated in Kennicutt & Evans (2012) (from Murphy et al. 2011), if rescaled from the Kroupa to Salpeter IMF, is very close to the $z = 0$ solar metallicity value of $\mathcal{K}_{FUV}(z)$ in **Figure 3**, but our somewhat smaller value should be more representative for the peak era of cosmic star formation at high redshift. Some authors express FUV luminosity as $L_{FUV} = \nu L_\nu$ in solar units. In that case, $\mathcal{K}_{FUV} = 2.2 \times 10^{-10}\, M_\odot$ year^{-1} $L_\odot^{-1}$ at 1,500 Å, and the conversion factor will depend on the wavelength.

Figure 4 shows the ratio of $\mathcal{K}_{FUV}$ for the Chabrier or Kroupa IMFs to that for the Salpeter IMF as a function of age for a constant SFR calculated using FSPS. This ratio is nearly constant, varying by only 5% with age and 3% over a factor of 100 in metallicity. Where necessary to convert SFRs from the literature from Chabrier or Kroupa IMFs to the Salpeter IMF, we divide by constant factors of 0.63 (Chabrier) or 0.67 (Kroupa). Similarly, **Figure 4** examines mass-to-light ratios for an SSP as a function of age in various bandpasses, comparing values for the Chabrier or Kroupa IMFs to the Salpeter IMF. Again, these ratios are fairly constant with age and have very little dependence on the bandpass. In other words, the color evolution for an SSP with Chabrier or Kroupa IMFs is very similar to that for the Salpeter IMF, showing a roughly constant offset in *M/L*. [The similar time dependence of *M/L* for the "bottom-light" Chabrier or Kroupa IMFs to that for the Salpeter IMF is something of a coincidence (or a conspiracy). The rate of luminosity evolution for an SSP depends on the logarithmic IMF slope at masses greater than 1 $M_\odot$ and is faster for the flatter $x = 1.3$ (Kroupa or Chabrier) than for the Salpeter value $x = 1.35$. However, the evolution of the recycled mass fraction is also faster for the Kroupa and Chabrier IMFs because their low-mass turnovers give them smaller mass fractions of long-lived stars. These two effects roughly cancel for $x = 1.3$, resulting in a time dependence for *M/L* that

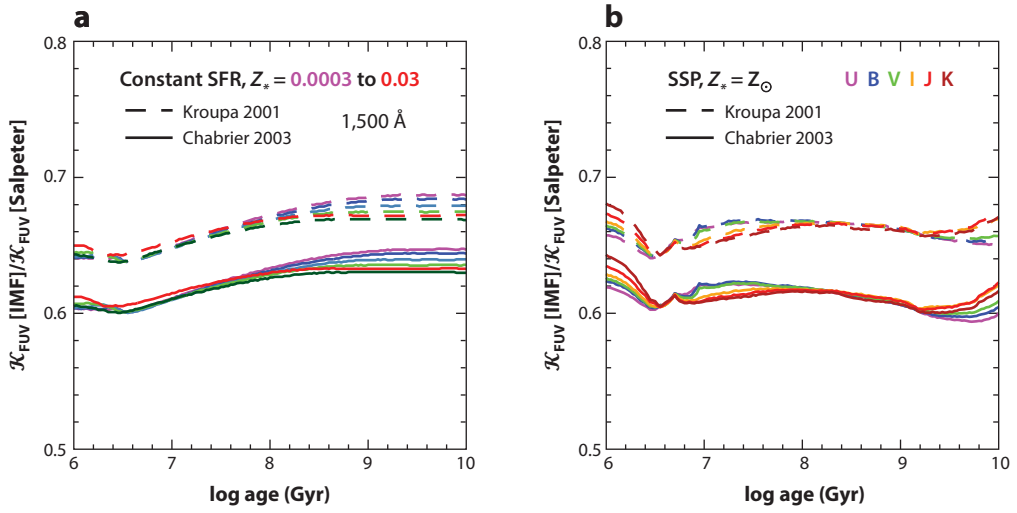

Figure 4

(*a*) The ratio of SFR/L_{FUV} conversion factors $\mathcal{K}_{FUV}$ (Equation 10) for Chabrier or Kroupa IMFs to that for a Salpeter IMF (0.1 to 100 $M_\odot$), for a constant SFR and for various metallicities computed with the FSPS models of Conroy et al. (2009). The difference in this conversion factor varies only slightly with age or metallicity over the ranges shown here. (*b*) Mass-to-light ratio for a simple stellar population as a function of age, for various bandpasses from the near UV through near IR, comparing values for Chabrier and Kroupa IMFs to Salpeter. This factor also has only a small dependence on age, bandpass, or metallicity (the last not shown here). Abbreviations: FSPS, flexible star population synthesis; IMF, initial mass function; SFR, star-formation rate.

is nearly the same as that for the Salpeter IMF. For an SSP with a "bottom-light" IMF with a Salpeter slope $x = 1.35$, the ratio of M/L compared with that for a Salpeter IMF would decrease by ∼16% over ∼5 Gyr, and a constant IMF rescaling factor for derived stellar masses would be inappropriate.] The dependence on metallicity (not shown) is very weak. To rescale stellar masses from Chabrier or Kroupa to Salpeter IMF, we divide by constant factors 0.61 and 0.66, respectively.

The greatest drawback for UV measurements of star formation is the obscuring effect of dust. Extinction is strong in the UV, so even modest amounts of dust can dramatically suppress the emerging UV flux. Dust re-emits the absorbed energy in the IR, which we discuss in the next section. A reliable measurement of SFRs from UV light must either correct for the effects of dust absorption or measure the absorbed energy directly through IR emission. We will return to the relation between UV dust attenuation and IR emission in Section 3.1.3 below.

3.1.2. Infrared emission. The energy that dust absorbs from the UV is reradiated at MIR and FIR wavelengths, making IR observations another important tool for measuring SFRs. The effect of dust extinction at FIR wavelengths is generally regarded as negligible, although in the MIR extinction can still be relevant for the most deeply buried star formation and active galactic nucleus (AGN). The total IR luminosity (L_{IR}, usually defined as being integrated over the wavelength range 8–1,000 μm) is a measurement of the energy that was absorbed by dust mainly at UV wavelengths. Because most UV emission comes from star formation, the IR luminosity is often interpreted as being directly proportional to the absorbed fraction of the energy from star formation. However, active nuclei can also produce strong UV emission, often in dusty environments, and may contribute to IR emission by heating dust in the torus and clouds

surrounding the AGN. Older stellar populations can also heat dust that is present in the ISM of a galaxy, contributing to the FIR emission. This is important particularly for "mature" galaxies with low current SFRs in the nearby Universe: For a galaxy such as our Milky Way, perhaps half of the FIR emission comes from dust heated by older stars, not from young star-forming regions (Lonsdale Persson & Helou 1987). However, for very actively star-forming galaxies without AGN, it is generally assumed that most of the IR emission arises from new star formation. Ideally, a galaxy's total IR luminosity would be measured by fitting a dust emission model to observations at several wavelengths, hopefully spanning the peak of dust emission. In practice, however, such multiwavelength data are often unavailable, and astronomers frequently use an SED template that is often derived from observations of local galaxies to extrapolate from a single observed flux density at some MIR or FIR wavelength, not necessarily close to the dust emission peak, to a total $L_{\rm IR}$. Thus, variations in the dust emission properties from galaxy to galaxy can lead to significant uncertainties in not only this bolometric correction but also the estimation of SFRs.

Arising from various components heated to different temperatures, the spectrum of dust emission is fairly complex. Most of the dust mass in a galaxy is usually in the form of relatively cold dust (15–60 K) that contributes strongly to the emission at FIR and submillimeter wavelengths (30–1,000 μm). Dust at several different temperatures may be present, including both colder grains in the ambient ISM and warmer grains in star-forming regions. Emission from still hotter, small-grain dust in star-forming regions, usually transiently heated by single photons and not in thermal equilibrium, can dominate the MIR continuum ($\lambda < 30$ μm) and may serve as a useful SFR indicator (e.g., Calzetti et al. 2007). The MIR spectral region (3–20 μm) is both spectrally and physically complex: It has strong emission bands from polycyclic aromatic hydrocarbons and absorption bands primarily from silicates. The strength of emission from polycyclic aromatic hydrocarbons can depend strongly on ISM metallicity and radiation field intensity (e.g., Engelbracht et al. 2005, 2008; Smith et al. 2007). Strong silicate absorption features are seen when the column density of dust and gas is particularly large toward obscured AGN and perhaps even nuclear starburst regions. AGN may contribute strong continuum emission from warm dust and can dominate over star formation at MIR wavelengths. By contrast, in the FIR, their role is less prominent.

The *Infrared Space Observatory* (ISO) and the *Spitzer Space Telescope* were the first telescopes with MIR sensitivities sufficient to detect galaxies at cosmological redshifts. In particular, *Spitzer* observations at 24 μm with the MIPS instrument are very sensitive and capable of detecting "normal" star-forming galaxies out to $z \approx 2$ in modest integration times. *Spitzer* is also very efficient for mapping large sky areas. It has a 24-μm beam size that is small enough (5.7 arcsec) to reliably identify faint galaxy counterparts to the IR emission. However, only a fraction of the total IR luminosity emerges in the MIR. As noted above, it is a complicated spectral region that leads to large and potentially quite uncertain bolometric corrections from the observed MIR flux to the total IR luminosity. At $z \approx 2$, where 24-μm observations sample rest-frame wavelengths around 8 μm, where the strongest polycyclic aromatic hydrocarbon bands are found, spectral templates based on local galaxies span more than an order of magnitude in the ratio $L_{\rm IR}/L_{8\ \mu{\rm m}}$ (e.g., Chary & Elbaz 2001, Dale & Helou 2002, Dale et al. 2005). More information about the type of galaxy being observed is needed to choose with confidence an appropriate template to convert the observed MIR luminosity to $L_{\rm IR}$ or an SFR.

The FIR thermal emission is a simpler and more direct measurement of star-formation energy. Partly owing to their large beam sizes that resulted in significant confusion and blending of sources and in difficulty localizing galaxy counterparts, ISO and *Spitzer* offer only relatively limited FIR sensitivity for deep observations. The *Herschel Space Observatory* dramatically improved such observations: Its 3.5-m mirror diameter provided a point spread function FWHM (full width half maximum) small enough to minimize confusion and to identify source counterparts in observations

from 70 to 250 μm. However, at the longest wavelengths of the *Herschel* SPIRE instrument, 350 and 500 μm, confusion becomes severe. *Herschel* observations can directly detect galaxies near the peak of their FIR dust emission: Dust SEDs typically peak at 60–100 μm in the rest frame, within the range of *Herschel* observations out to $z < 4$. Temperature variations in galaxies lead to variations in the bolometric corrections for observations at a single wavelength, but these differences are much smaller than for MIR data, generally less then factors of 2.

Despite *Herschel*'s FIR sensitivity, deep *Spitzer* 24-μm observations, in general, still detect more high-z sources down to lower limiting IR luminosities or SFRs. At $z \approx 2$, the deepest *Herschel* observations only barely reach to roughly $L^*_{\rm IR}$ [the characteristic luminosity of the "knee" of the infrared luminosity function (IRLF)], leaving a large fraction of the total cosmic SFRD undetected, at least for individual sources, although stacking can be used to probe to fainter levels. Deep *Spitzer* 24-μm observations detect galaxies with SFRs several times lower, and many fields were surveyed to faint limiting fluxes at 24 μm during *Spitzer*'s cryogenic lifetime. Therefore, there is still value in trying to understand and calibrate ways to measure star formation from deep MIR data, despite the large and potentially uncertain bolometric corrections.

In practice, observations of IR-luminous galaxies detected at high redshift with both *Spitzer* and *Herschel* have demonstrated that the IR SEDs for many galaxies are well behaved and that variations can be understood at least in part. Several pre-*Herschel* studies (Daddi et al. 2007; Papovich et al. 2007; Magnelli et al. 2009, 2011) compared 24-μm observations of distant galaxies with those of other SFR tracers, including *Spitzer* FIR measurements (either individual detections or stacked averages) and radio emission. On average, the MIR to FIR flux ratios for galaxies at $z \lesssim 1.3$ match those predicted by local IR SED templates such as those of Chary & Elbaz (2001), implying that 24-μm-derived SFRs should be reliable. However, at higher redshift, $1.3 < z < 2.5$, the 24-μm fluxes were brighter than expected relative to the FIR or radio data, i.e., SFRs derived from 24-μm data using local SED templates may be systematically overestimated at $z \approx 2$. This result was upheld by early *Herschel* studies (Elbaz et al. 2010, Nordon et al. 2010). In a joint analysis of the IR SED properties of both nearby and high-redshift IR-luminous galaxies, Elbaz et al. (2011) provided an explanatory framework for these observations in terms of the distinction between a majority population of galaxies obeying a "main-sequence" correlation between their SFRs and stellar masses and a minority "starburst" population with substantially higher SFRs per unit mass (or sSFR). Locally, starburst galaxies have more compact, high surface density star-forming regions, whereas normal disk galaxies on the star-forming main sequence have star formation distributed on larger scales with lower surface density. Starbursts also have warmer average dust temperatures and a significantly larger ratio between their FIR and 8-μm rest-frame luminosities than those of the main-sequence disk galaxies. Locally, most luminous and ultraluminous infrared galaxies (LIRGs and ULIRGs, with $L_{\rm IR} > 10^{11}\ L_\odot$ and $>10^{12}\ L_\odot$, respectively) are merger-driven starbursts, but at $z \approx 2$ where the SFRs and sSFRs of galaxies are globally much larger, the majority of LIRGs and ULIRGs are "normal" main-sequence galaxies. Their IR SEDs are more similar to those of ordinary, local star-forming spiral galaxies and have smaller bolometric corrections from observed 24-μm data (rest frame $\lambda \approx 8$ μm) than those predicted by SED templates designed to match local LIRGs and ULIRGs. Elbaz et al. (2011) constructed a "universal" main-sequence SED from the ensemble of high-z *Spitzer* and *Herschel* photometry for galaxies in the Great Observatories Origins Deep Survey (GOODS) fields at $0.3 < z < 2.5$. This SED leads to consistent total IR luminosities for the large majority of galaxies over that redshift range. Although no single template can be used to accurately derive $L_{\rm IR}$ or SFR from MIR observations for all galaxies, we now have a better understanding of how this can be done on average, which may be sufficient for deriving the global redshift evolution of the IR luminosity density or its corresponding SFRD. Rodighiero et al. (2011) (see also Sargent et al. 2012) showed that starbursts (whose IR SEDs

deviate significantly from those of the main-sequence population) account for only 10% of the global SFRD at $z \approx 2$. With the data now available from *Herschel* and *Spitzer*, a broad understanding of the evolving IRLF and IR luminosity density, at least at $0 < z < 2.5$, seems within reach.

MIR and FIR observations require space-based telescopes, but at submillimeter and millimeter wavelengths, observations can once again be made from the ground within certain atmospheric transmission windows. The advent of submillimeter bolometer array cameras such as SCUBA on the JCMT revolutionized the field and led to the first detections of a large population of ULIRGs at high redshift (e.g., Smail et al. 1997, Hughes et al. 1998, Barger et al. 1998). Until recently, only the most luminous high-z objects could be readily detected, but the new ALMA interferometer will improve detection sensitivities by more than an order of magnitude, albeit over small fields of view. As noted above, submillimeter observations measure emission beyond the peak of dust emission, where flux is declining steeply with wavelength in the Rayleigh-Jeans part of the SED. This leads to a negative *K* correction so strong that it cancels out the effects of distance: A galaxy with a given IR luminosity will have roughly constant submillimeter flux if it is observed at any redshift $1 < z < 10$. By contrast, the bolometric corrections from the observed submillimeter wavelengths to the total IR luminosities are large and depend strongly on dust temperature. This can lead to significant uncertainties interpreting submillimeter fluxes from high-redshift sources and a bias toward detecting galaxies with the coldest dust emission.

By analogy with Equation 10, we express the conversion from IR luminosity ($L_{\rm IR}$) to ongoing SFR as

$$\mathrm{SFR_{IR}} = \mathcal{K}_{\rm IR} \times L_{\rm IR}, \tag{11}$$

where $L_{\rm IR}$ is the IR luminosity integrated over the wavelength range from 8 to 1,000 μm. Here, it is assumed that the IR emission is entirely due to recent star formation, but in practice, AGN and older stars can contribute to dust heating. Furthermore, if the net dust opacity to young star-forming regions in a galaxy is not large and if a significant amount of UV radiation emerges, then the SFR derived from the IR luminosity will represent only a fraction of the total. Hence, we write $\mathrm{SFR_{IR}}$ in Equation 11 to indicate that this is only the dust-obscured component of the SFR. For this reason, some authors advocate summing the SFRs derived from the observed IR and UV luminosity densities, the latter uncorrected for extinction. Once again, we calibrate the conversion factor $\mathcal{K}_{\rm IR}$ using the FSPS models of Conroy et al. (2009), which also incorporate dust attenuation and re-emission. We assume simple foreground-screen dust attenuation from Calzetti et al. (2000), although the details of the dust absorption model matter relatively little. The luminosity integrated from 8 to 1000 μm depends only mildly on the detailed dust emission parameters (essentially, the dust temperature distribution) for a broad range of reasonable values. Because the dust luminosity is primarily reprocessed UV emission from young star formation, the conversion factor $\mathcal{K}_{\rm IR}$ also depends on the details of the SFH and on metallicity. In practice, we may expect that galaxies with substantial extinction and bolometrically dominant dust emission are unlikely to have low metallicities; here, we assume solar metallicity for our calibration. We modify Equation 11 to account for both the FUV and FIR components of star formation:

$$\mathrm{SFR_{tot}} = \mathcal{K}_{\rm FUV} L_{\rm FUV} + \mathcal{K}_{\rm IR} L_{\rm IR}, \tag{12}$$

where $L_{\rm FUV}$ is the observed FUV luminosity at 1,500 Å with no correction for extinction. We use FSPS models with a Salpeter IMF, solar metallicity, and constant SFR to compute $L_{\rm FUV}$ and $L_{\rm IR}$ as a function of age for various levels of dust attenuation; we then solve for $\mathcal{K}_{\rm IR}$. **Figure 5** shows the result of this calculation: SFR is expressed in units of $\mathrm{M_\odot\ year^{-1}}$, and both the FUV and IR luminosities are expressed in solar units (with $L_{\rm FUV} = \nu L_\nu$) to display both on the same

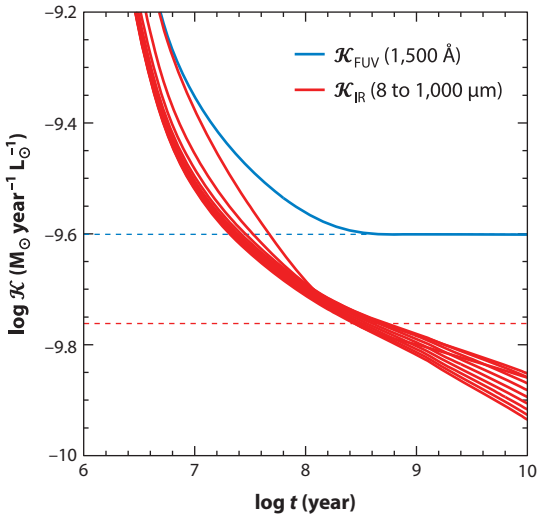

Figure 5

The SFR to luminosity ratio $\mathcal{K}$ for dusty galaxies, in solar luminosity units, calibrated with the FSPS models of Conroy et al. (2009), assuming a constant SFR, a Salpeter IMF, and solar metallicity. The blue curve shows the FUV conversion factor $\mathcal{K}_{FUV}$ (see Section 3.1.1), and the blue dotted line indicates its asymptotic value. The red curves show the FIR conversion factor $\mathcal{K}_{IR}$ computed as per Equation 12, for 1,500-Å extinction ranging from 0.055 to 5.5 magnitudes. The dotted red line indicates the value of $\mathcal{K}_{IR}$ from Kennicutt (1998), which we also adopt here. Abbreviations: FSPS, flexible star population synthesis; FIR, far-infrared; FUV, far-UV; IMF, initial mass function; SFR, star-formation rate.

scale. As shown in Section 3.1.1, the FUV emission reaches a steady state after ∼300 Myr, and for this calculation, we use the asymptotic value $\mathcal{K}_{FUV} = 2.5 \times 10^{-10}\,M_\odot$ year^{-1} $L_\odot^{-1}$ (equivalently, $\mathcal{K}_{FUV} = 1.3 \times 10^{-28}\,M_\odot$ year^{-1} erg^{-1} s Hz). Instead, L_{IR} increases slowly (hence, K_{IR} decreases) as the optical rest-frame luminosity of longer-lived stars continues to build, some fraction of which is then absorbed by dust and re-emitted. This model with constant SFR and constant dust attenuation results in a modest effect of ∼0.1 dex in log $\mathcal{K}_{IR}$ per dex in log t. However, in practice, older stars will likely have lower dust extinction than younger stars, thus further reducing this trend. At ages of a few 10^8 years, K_{IR} depends very little on the total extinction. Kennicutt (1998) proposed a calibration factor $\mathcal{K}_{IR} = 1.73 \times 10^{-10}\,M_\odot$ year^{-1} $L_\odot^{-1}$, which is fully consistent with the models shown in **Figure 5** for an age of 300 Myr. We adopt that value for this review. For luminosities measured in cgs units, we can write $\mathcal{K}_{IR} = 4.5 \times 10^{-44}\,M_\odot$ year^{-1} erg^{-1} s.

3.1.3. UV extinction and IR emission. As noted above, dust can substantially attenuate UV emission, not only compromising its utility for measuring SFRs, but also producing IR emission, which is a valuable tracer of star-formation activity. Considerable effort has been invested in understanding the physics and phenomenology of extinction in galaxies (for a review, see Calzetti 2001). In principle, the best way to account for the effect of dust attenuation is to directly measure the energy emitted at both UV and IR wavelengths, i.e., both the luminosity that escapes the galaxy directly and that which is absorbed and reradiated by dust. This provides a "bolometric" approach to measuring SFRs. In practice, however, data sensitive enough to measure FIR luminosities of high-redshift galaxies are often unavailable. *Herschel* greatly advanced these sorts of observations, but its sensitivity, although impressive, was sufficient to detect only galaxies with high SFRs > $100\,M_\odot$ year^{-1}, at $z > 2$.

For star-forming galaxies with moderate extinction at $z > 1$, optical photometry measuring rest-frame UV light is obtained much more easily than are suitably deep FIR, submillimeter, or radio data. Current observations of UV light are also typically much more sensitive to star formation than are those at other wavelengths (**Figure 1**). As a result, trying to infer SFRs from rest-frame UV observations alone is tempting, but this requires reliable estimates of dust extinction corrections. For example, Lyman break galaxies (LBGs) are a UV-selected population of star-forming high-redshift galaxies. Their selection would favor relatively low extinction, but even LBGs are quite dusty: Reddy et al. (2012) used *Herschel* observations to determine that, on average, 80% of the FUV emission from typical ($\sim L^*_{\rm FUV}$) LBGs at $z \approx 2$ is absorbed by dust and reradiated in the FIR. Many more massive galaxies with high SFRs have greater extinction. So-called dust-obscured galaxies (Dey et al. 2008) have MIR to UV flux density ratios >1,000 (typically corresponding to $L_{\rm IR}/L_{\rm FUV} > 100$) (Penner et al. 2012) and are quite common, contributing 5–10% of the SFRD at $z \approx 2$ (Pope et al. 2008); many of these are nearly or entirely invisible in deep optical images.

Nevertheless, the widespread availability of rest-frame UV data for high-redshift galaxies encourages their use for measuring the cosmic SFH. Presently, at $z \gg 2$, there is little alternative: Even the deepest *Spitzer*, *Herschel*, radio, or submillimeter surveys can detect only the rarest and most ultraluminous galaxies at such redshifts. By contrast, deep optical and NIR surveys have now identified samples of thousands of UV-selected star-forming galaxies out to $z \approx 7$ and beyond.

Attempts to measure and correct for dust extinction in high-z galaxies have generally used the UV spectral slope (designated β) as a measure of UV reddening and have adopted empirical correlations between UV reddening and UV extinction. Calzetti et al. (1994, 2000) used ultraviolet and optical spectroscopy to derive an empirical, average dust attenuation curve for a sample of local UV-bright star-forming galaxies. Meurer et al. (1999) (later updated by Overzier et al. 2011) used UV and FIR data for a similar local sample to empirically calibrate the relation between UV reddening (β) and UV extinction (IRX $\equiv L_{\rm IR}/L_{\rm FUV}$, which can be directly related to $A_{\rm FUV}$). The reasonably tight IRX-β relation obeyed by the local UV-bright galaxies is broadly consistent with the Calzetti attenuation law, hence reinforcing its popularity. However, other local studies showed clearly that some galaxies deviate from these relations. Goldader et al. (2002) found that nearby ULIRGs deviate strongly from the Meurer IRX-β relation; these ULIRGs have very large values of IRX but often with relatively blue UV spectral index β. This was interpreted to mean that the observed UV light from local ULIRGs is relatively unreddened star formation in the host galaxy that is unrelated to the bolometrically dominant star formation, which is entirely obscured from view at UV-optical wavelengths and detected only in the FIR. Instead, observations of ordinary spiral galaxies (Kong et al. 2004, Buat et al. 2005) measured redder values of β for a given IRX. This is generally taken as evidence that light from older and less massive stars contributes significantly to the near-UV emission, leading to redder UV colors for reasons unrelated to extinction. In general, different relative distributions of stars and dust can lead to different net attenuation properties. Extinction can easily be patchy: Winds from star-forming regions can blow away dust on certain timescales, whereas other regions that are younger or more deeply embedded in the galaxy's ISM remain more heavily obscured. Dust heating also depends on geometry, leading to different distributions of dust temperatures and different emission spectra at IR and submillimeter wavelengths.

At high redshift, there are only relatively limited tests of the relation between UV reddening and extinction. Reddy & Steidel (2004) and Reddy et al. (2006, 2010, 2012) have compared various SFR tracers (including radio, *Spitzer* 24-μm, and *Herschel* 100–160-μm emission) to show that Calzetti/Meurer UV extinction laws are broadly appropriate for the majority of L_* LBGs at $z \approx 2$. However, they found evidence for systematic deviations for galaxies with the largest SFRs ($>100\,{\rm M}_\odot\ {\rm year}^{-1}$), which, similar to local ULIRGs, show "grayer" effective attenuation (i.e., less

UV reddening for their net UV extinction). They also found evidence for systematic deviations for the youngest galaxies, which show stronger reddening for their net FUV extinction, perhaps because of the metallicity or geometric effects that steepen the wavelength dependence of the UV reddening function compared with results from the Calzetti law. Assuming Calzetti attenuation, Daddi et al. (2007) and Magdis et al. (2010) also found broad consistency between UV-based and IR- or radio-based SFR measurements for samples at $z \approx 2$–3 (although, see Carilli et al. 2008). However, studies that have selected galaxies primarily on the basis of their IR emission have tended to find significant deviations from Meurer/Calzetti attenuation. In general, these deviations indicate that UV-based SFRs using Meurer/Calzetti UV slope corrections significantly underestimate total SFRs (e.g., Chapman et al. 2005, Papovich et al. 2007). Such studies have also found that differently selected populations may obey systematically different net dust attenuation relations depending on the properties of the galaxies (Buat et al. 2012, Penner et al. 2012).

Therefore, we must remain cautious about SFRs derived from UV data alone, even when estimates of UV reddening are available. Current evidence suggests that these may work well on average for UV-bright LBGs with relatively low reddening but may fail for other galaxies including the most IR-luminous objects that dominate the most rapidly star-forming galaxy population. Star formation that is obscured by too much dust, e.g., in compact starburst regions, will be unrecorded by UV observations and can be measured directly only with deep IR, submillimeter, or radio measurements.

3.1.4. Other indicators: nebular line, radio, and X-ray emission. Star formation also produces nebular line emission from excited and ionized gas in HII regions. Recombination lines of hydrogen such as Hα and Lyα are often used to measure SFRs, because they have a close relation to photoionization rates that are mainly due to intense UV radiation from OB stars. Hence, they trace massive star formation quite directly, although the presence of AGN can also contribute to these lines. Other lines from heavier elements such as [OII] 3,727 Å or [OIII] 5,007 Å have been used, but they tend to have more complex dependence on ISM conditions such as metallicity or excitation. Emission lines are also subject to absorption by dust in the star-forming regions. This is particularly true for Lyα, which is a resonance line, scattered by encounters with neutral hydrogen atoms. Such encounters can greatly increase the path length of travel for Lyα and hence increase the likelihood that it may encounter a dust grain and be absorbed. Overall, Hα is regarded as the most reliable among the easily accessible nebular SFR tracers (e.g., Moustakas et al. 2006). Weaker but less extinguished hydrogen lines in the NIR, such as Paschen α, can be very useful for measuring SFRs in dusty galaxies, but they are generally accessible only at very low redshift, although the JWST will open the possibility for measuring these for significant numbers of galaxies at cosmological distances.

Radio emission is also correlated with star formation, as SN-accelerated electrons emit non-thermal radiation at centimeter wavelengths; thermal (free-free) emission from electrons in HII regions can also contribute, particularly at higher frequencies (>5 GHz). The physics is somewhat complicated and not entirely understood, but a remarkably tight correlation is observed between radio emission and FIR emission in local galaxies spanning many orders of magnitude in luminosity (e.g., Condon 1992, Yun et al. 2001). Radio emission is free from dust extinction and thus offers a relatively unbiased tracer of star formation. However, it is difficult to obtain radio observations deep enough to detect ordinary star-forming galaxies at high redshift, although recent upgrades to the Karl G. Jansky VLA have significantly improved its sensitivity. AGN can also contribute to radio emission, occasionally dominating for radio-loud AGN (which are a minority population). Radio emission should also be suppressed at earlier cosmic epochs, as electrons should lose energy by inverse Compton scattering off microwave background photons whose energy density increases

at high redshift. Recent studies have found little evidence for redshift evolution in the FIR to radio correlation (Appleton et al. 2004; Ivison et al. 2010a,b; Sargent et al. 2010a,b; Mao et al. 2011).

Even X-rays have been used to trace SFRs. X-rays are typically regarded as a quintessential signature of AGN activity in galaxies, but they are also produced by young stellar populations, notably by X-ray binaries. In the absence of an AGN, X-ray emission may be measured from individual star-forming galaxies out to $z \approx 1$ in the deepest *Chandra* fields, and stacking measurements have been used to reach fainter fluxes in studies of UV-selected galaxies, with detections at $1 < z < 4$ and upper limits at higher redshifts (Reddy & Steidel 2004; Laird et al. 2005, 2006; Lehmer et al. 2005; Basu-Zych et al. 2013). However, the proportionality between X-ray luminosity and SFR may vary with stellar population age and other parameters that could affect the mix of low- and high-mass X-ray binaries present in a galaxy; various calibrations that differ significantly have been published (e.g., Ranalli et al. 2003, Persic et al. 2004). Overall, because most of the cosmic X-ray background arises from AGN (for a review, see Brandt & Hasinger 2005), the value of using X-rays to measure the cosmic SFH seems limited (we do not discuss this method further).

3.2. "Weighing" Stellar Mass

Whereas hot young stars emit most of their energy at UV wavelengths, the cooler low-mass stars that dominate the stellar mass of a galaxy emit most of their light at red optical and NIR wavelengths. If we examine the SED of an evolving SSP from ages older than 10^9 years, the bulk of the luminosity (in λf_λ energy units) is emitted in a broad plateau between 0.4 and 2.5 μm, peaking at ∼1 μm for ages >2 Gyr. (In f_ν flux density or AB magnitude units, the SED peak is at approximately 1.6 μm, where there is a minimum in the H^- opacity of cool stellar atmospheres.) The effects of dust extinction are also greatly reduced at NIR wavelengths: For Calzetti attenuation, the extinction (in magnitudes) A in the K-band is 10 times smaller than that in the V-band and 25 times smaller than that at 1,600 Å.

The luminosity, and hence the mass-to-light ratio, of a stellar population evolves very steeply with time at UV and blue wavelengths: Young stars evolve quickly off the main sequence but more slowly at red and NIR wavelengths. Therefore, observations in the NIR rest frame more closely trace the integrated stellar mass of a galaxy, but we cannot neglect the effects of evolution: The flux at 1 μm still changes by more than an order of magnitude as a stellar population ages from 0.1 to 10 Gyr (see, e.g., figure 9 from Bruzual & Charlot 2003). Therefore, we need to do more than simply measure the NIR luminosity to infer a stellar mass.

In effect, astronomers use the colors or SED of a galaxy to infer the expected mass-to-light ratio at some wavelength (preferably in the red or NIR) and then multiply the observed luminosity by M/L to estimate the stellar mass (M_*). The most common method is to fit spectral templates generated by stellar population synthesis models to broadband photometry in whatever bands are available that span rest-frame UV to NIR wavelengths, where stellar photospheric emission dominates the galaxy light. Generally speaking, researchers generate a large suite of models that span a wide range of stellar population parameters, including the past SFH, age, metallicity, and dust attenuation. The IMF is typically fixed, because there is almost no photometric signature that can usefully constrain it. The suite of models is redshifted to match a galaxy of interest. The models are then convolved by the filter bandpasses to generate synthetic broadband fluxes that are fit to the photometry, allowing the luminosity normalization to vary and minimizing χ^2 or some other likelihood parameter. The unnormalized models have a specified unit mass; therefore, normalization of the best-fitting model provides the best estimate of the galaxy's stellar mass, given the range of input parameters that were allowed.

In principle, this method can be used to constrain other stellar population parameters such as the galaxy's age, SFR, or the degree of extinction that is present. In practice, the fitting results for various parameters are often quite degenerate. For example, age, extinction, and metallicity all affect the integrated colors of a galaxy. As a result, the derived values of these parameters tend to be highly covariant: A galaxy may be red because it is old, dusty, or very metal rich. With very good photometry, particularly spanning a large range of wavelength and with many bandpasses that can more accurately sample the detailed spectral shape (e.g., measuring relatively sharp age-sensitive features such as the Balmer or 4,000-Å breaks), these constraints can be improved, but it is hard to avoid significant degeneracies. Careful practitioners may consider joint probability distributions for models that fit with acceptable likelihood. The stellar mass tends to be the best-constrained parameter, largely because the degeneracies in other parameters all tend to affect the net M/L of the model in similar ways. Redder colors from age, dust, or metallicity all tend to affect M/L to a similar (but not identical) degree. Whereas parameters such as age or reddening may be individually uncertain, the net M/L of acceptable models does not vary so much. Thus, the total mass is well constrained. Many papers have discussed stellar population modeling uncertainties in estimating galaxy masses; these are thoroughly reviewed by Conroy (2013).

Other than the choice of the IMF, the largest uncertainty that affects the derived stellar mass is usually the necessarily imperfect knowledge of the galaxy's past SFH. Fundamentally, more recently formed stars can easily outshine older stars and dominate the observed light, even at red wavelengths. The observed photometry may be dominated by the younger starlight, even though the actual galaxy mass may be dominated by older stars that are lost in the glare of the younger stars ("outshining," e.g., Papovich et al. 2001, Maraston et al. 2010) and thus have little impact on the choice of the best-fitting models. Therefore, the model fitting often underestimates the age of the galaxy or the potential contribution of older stars to the mass, and it may also underestimate the mass. If the actual SFH were well known (which is almost never the case in practice), this might not be a problem. For example, the models used to fit the photometry are often assumed to have smoothly varying SFRs, but the actual SFHs of real galaxies can be complex and nonmonotonic, fluctuating with time and perhaps punctuated by short-duration bursts. Even if very large suites of models with complex SFHs are considered, outshining tends to ensure that recently formed stars drive the model fitting, whereas the mass in older stars is poorly constrained. This effect generally leads to underestimation of galaxy stellar masses (Pforr et al. 2012). Realistically constraining the distribution of allowable past SFHs for real galaxies, especially at high redshift, remains a basic limitation when deriving stellar masses.

In practice, these SFH degeneracies are largest for galaxies with recent star formation. For galaxies that have not formed stars in a long while (say >1 Gyr) or for which the current SFR is small compared with the stellar mass (often quantified by the sSFR), the outshining is small and, thus, so is the resulting systematic uncertainty on M/L. Therefore, stellar masses for present-day elliptical galaxies, which are old with little or no ongoing star formation, or for ordinary spiral galaxies such as the Milky Way tend to be reasonably well-constrained, whereas those for very actively star-forming galaxies are less certain. As an example, Papovich et al. (2001) fit models to HST WFPC2 and NICMOS photometry for faint LBGs at $z \approx 2.5$ in the Hubble Deep Field North (HDF-N). When using models with smoothly varying SFHs, they found stellar mass uncertainties to be $\sigma(\log M_*) < 0.5$ dex, with typical uncertainties of 0.25 dex, i.e., less than a factor of 2. However, if they considered "maximal M/L" models, which allowed for as much older stellar mass as possible within the χ^2 fitting constraints formed at $z = \infty$, the masses could in principle be as much as 3 to 8 times larger. In practice, such extreme models seem unlikely. Moreover, the early work of Papovich et al. (2001) used photometry only out to the K-band or rest-frame wavelengths ~6,000 Å at $z = 2.5$. Today, deep *Spitzer* IRAC photometry routinely

measures fluxes for high-z galaxies at redder rest-frame wavelengths and can significantly improve stellar mass constraints. Nevertheless, even with the best data from *Spitzer* (or the JWST in the future), the effects of outshining fundamentally limit our certainty about stellar mass estimates for individual objects. These effects can be reduced only if reasonable prior assumptions can more tightly constrain the range of allowable SFHs.

Interestingly, at very high redshifts some of these SFH uncertainties are reduced, simply because the Universe is much younger. At $z > 6$, the Universe is less than 1 Gyr old, and the oldest stars in the galaxies must be younger than that; this sets a cap on M/L for a hypothetical unseen old population and thus on its possible contribution to the total stellar mass. Curtis-Lake et al. (2013) provided a recent and detailed discussion of stellar population modeling uncertainties for galaxies at $z \sim 6$.

Additionally, the practitioners who create stellar population models have not reached complete consensus: Questions regarding evolutionary tracks, the contributions of certain stellar subpopulations, and the behavior of stellar populations at low and high metallicities remain topics of debate or are poorly calibrated by observations. One widely recognized example of such uncertainties was highlighted by Maraston (2005), whose models featured significantly greater contributions of emission from thermally pulsating asymptotic giant branch (TP-AGB) stars to the red and NIR rest-frame light at SSP ages between a few hundred million years and ∼2 Gyr. The enhanced red luminosity led to lower M/L at these wavelengths and redder colors, with potentially quite significant effects (factors of 2 or more) in derived stellar masses for galaxies dominated by stars in this age range. Although such populations may not dominate in most present-day galaxies, at $z \approx 2–4$ when the Universe was only a few billion years old their role must be accurately modeled to ensure proper estimates of stellar masses. Maraston et al. (2006) found that this could reduce derived stellar masses by ∼60% on average for K-band-selected star-forming galaxies at $z \approx 2$ compared with results computed using the popular models of Bruzual & Charlot (2003). Although Bruzual et al. (2013) released new models in 2007 that featured enhanced TP-AGB emission, they have argued in recent conference presentations for weaker TP-AGB emission more similar to that in the older models. Given the lack of a completely satisfactory way to compute this contribution on theoretical principles, a lot hangs on the sparseness of data available to empirically calibrate the emission and evolution of TP-AGB stars.

4. TRACING THE GALAXY EMISSION HISTORY WITH LARGE SURVEYS

Over the past 18 years, a sea of published measurements of the cosmic SFRD or SMD at many different redshifts have used different data sets and methods. Much of the observational work has been carried out in deep survey fields that have accumulated outstanding multiwavelength data for this purpose and cover different angular scales to different depths (**Figure 6**). We do not attempt a comprehensive review of this literature. Instead, we highlight key data sets and analyses from roughly the first decade of cosmic SFR measurements (1996–2006) and then focus on the most important or extensive recent measurements that we use in our analysis in Section 5. Hopkins (2004) and Hopkins & Beacom (2006) provided an extensive compilation of SFRD measurements up to 2006, whereas Wilkins et al. (2008a) summarized SMD derivations through 2007. Other authors have also compiled these data more recently (e.g., Behroozi et al. 2013).

The number of papers that present measurements of the cosmic SFR history vastly exceeds the number of different data sets that have been used for this purpose because certain well-trodden surveys such as the HDF-N, the Hubble Ultradeep Field (HUDF), GOODS, and COSMOS have been used repeatedly by many groups or by the same groups who continue to refine their analyses

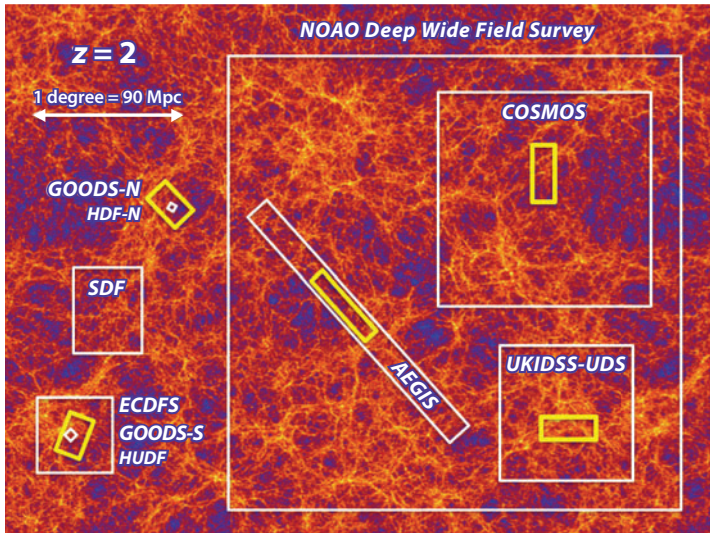

Figure 6

Relative sizes of the regions on the sky observed in several important surveys of the distant Universe. The two Great Observatories Origins Deep Survey (GOODS) fields, the Subaru Deep Field (SDF) and the Extended Chandra Deep Field South (ECDFS) are shown on the left. Very-deep surveys such as the Hubble Deep Field North (HDF-N) and the Hubble Ultradeep Field (HUDF) [Advanced Camera for Surveys (ACS) area shown], which are embedded within the GOODS fields, can detect fainter galaxies, but cover only very tiny regions on the sky. Other surveys such as the Cosmic Evolution Survey (COSMOS), the UK Infrared Deep Sky Survey (UKIDSS), the Ultradeep Survey (UDS), the All-Wavelength Extended Groth Strip International Survey (AEGIS), and the National Optical Astronomy Observatory (NOAO) Deep Wide Field Survey cover wider regions of the sky, usually to shallower depths, i.e., with less sensitivity to very faint galaxies. However, they encompass larger and perhaps more statistically representative volumes of the Universe. The yellow boxes indicate the five fields from the Cosmic Assembly Near-Infrared Deep Extragalactic Legacy Survey (CANDELS), each of which is embedded within another famous survey area. The image in the background shows a cosmological *N*-body simulation performed within the MultiDark project (see **http://www.multidark.org/MultiDark/**), viewed at $z = 2$, more than 10 Gyr ago. The colors represent the matter density distribution in a slice 43-Mpc thick, or $\Delta(z) = 0.03$ at that redshift, and all lengths are given in comoving units for $h = 0.7$. Small surveys may sample under- or overdense regions, whereas larger surveys can average over density variations, but may not be sensitive to the ordinary, relatively faint galaxies that are most numerous in the Universe. Averaging over redshift intervals that are greater than that shown in the background figure will smooth over density variations, but for any redshift binsize cosmic variance will be smaller for wider surveys or when a survey is divided into fields sampling multiple, independent sightlines.

or add new observational information. One should thus be cautious compiling results from many different studies: Although the analyses are independent, the data used and the actual galaxies measured may not be different. For example, the SFHs of GOODS-South and COSMOS are particularly well studied, but true cosmic variance due to clustering in those fields will not cancel out from one analysis to another.

4.1. UV Surveys

The largest number of analyses of the cosmic SFRD have used rest-frame UV continuum measurements, largely because the method is quite sensitive (see **Figure 1**) and can be applied over a very broad range of redshifts. Rest-frame FUV (1,500 Å) SFRs at $1.4 < z < 6$ can be measured using optical photometry that is (relatively) easily obtained with ground-based or HST imaging.

The heavy use of photometric redshifts in recent years has led to much work based on imaging data alone, with little or no spectroscopy. However, in popular deep survey fields such as GOODS or COSMOS, the photo-z values are typically well calibrated thanks to the widespread availability of thousands of spectroscopic measurements. At $z < 1$, rest-frame UV measurements ideally require space-based telescopes such as GALEX or HST to reach rest-frame wavelengths near 1,500 Å, but several studies have used blue or *U*-band imaging to sample mid-UV wavelengths (e.g., 2,800 Å) at $z < 1$ instead.

The modern era of SFRD measurements arguably began with the analysis of Lilly et al. (1996), who were the first to combine a large and deep (for its time) spectroscopic redshift survey with multiwavelength photometry and to derive LFs and luminosity densities at several different rest-frame wavelengths, including the rest-frame UV. The Canada-France Redshift Survey (CFRS) was carried out using the 4-m *Canada-France-Hawaii Telescope* and mainly surveyed the Universe out to $z < 1$. The available *BVIK*-band photometry permitted direct measurement of 2,800-Å rest-frame luminosities at $z > 0.5$ and down to $z \approx 0.3$ with modest spectral extrapolation. Lilly et al. (1996) found that the 2,800-Å luminosity density declined by approximately one order of magnitude from $z = 1$ to the present, which they interpreted as a steep decline in the SFRD.

Madau et al. (1996) used the then-new HDF observations to extend this analysis to much higher redshift. They employed color-selected LBG samples at $\langle z \rangle = 2.75$ and 4. The deep HST WFPC2 photometry allowed luminosities to be measured at 1,500 Å in the rest frame, reaching fainter than contemporaneous ground-based LBG data at $z \approx 3$ from Steidel et al. (1996) and thus integrating further down the LF. Madau et al. (1996) quoted only lower limits for the SFRD, without extrapolation to fainter luminosities (relatively small, given the depth of the HDF imaging) and without correction for dust absorption (significant, but at the time little known). Later analyses (e.g., Sawicki et al. 1997, Madau et al. 1998b, Steidel et al. 1999) fit Schechter LFs to the photometric samples to extrapolate to total UV luminosity densities. Connolly et al. (1997) and Pascarelle et al. (1998) combined the optical HST imaging of the HDF with ground-based NIR data to improve photometric redshift analyses in the redshift "desert" at $1 < z < 2$, between the regime of Lilly et al. (1996) and that of Madau et al. (1996). Taken together, the HDF measurements at $z > 1$ and the CFRS measurements at $z < 1$ suggested a general "rise and fall" picture of a UV luminosity density and, by inference, the cosmic SFH that peaked somewhere between $z \approx 1$ and 2.

Various surveys subsequently extended this finding using other data sets or different analyses. Several groups reanalyzed the HDF (and later the HDF-South) data in various ways or made use of deeper spectroscopic surveys with the *Keck* telescope. Cowie et al. (1999) and Wilson et al. (2002) combined *Keck* spectroscopy in several fields with deep *U*-band imaging to measure shorter rest-frame UV wavelengths (2,000–2,500 Å) at $z < 1$ than were probed in the CFRS analysis of Lilly et al. (1996) and derived a shallower rate of decline in the SFRD. Wolf et al. (2005) used 17-filter intermediate and broadband imaging to obtain high-quality photometric redshifts at $z < 1.25$ in the Extended Chandra Deep Field South and analyzed the 2,800-Å luminosity density evolution.

Ideally, UV rest-frame observations at $z < 1$ should be done from space telescopes to sample shorter UV wavelengths than those used in the ground-based studies by Lilly, Wilson, Wolf, and others. In early work, Treyer et al. (1998) and Sullivan et al. (2000) used the FOCA balloon-borne UV telescope to measure 2,000-Å luminosity densities at $z \approx 0.15$. GALEX has since provided vastly more FUV data, including both wide-area and deeper surveys. Wyder et al. (2005) combined GALEX all-sky imaging survey data with distances from the 2dF Galaxy Redshift Survey (2dFGRS) over 56 deg^2 to measure local ($z \approx 0.055$) LFs at 1,500 Å and 2,300 Å. Budavári et al. (2005) analyzed a similar total sky area using somewhat deeper GALEX data and SDSS-derived photometric redshifts to compute LFs and densities at $z < 0.25$. Salim et al. (2007) and

Robotham & Driver (2011) have since analyzed much larger GALEX data sets with SDSS data to cover as much as 830 deg^2. Robotham & Driver (2011) presented a straightforward derivation of the UV luminosity function (UVLF) and luminosity density, whereas Salim et al. (2007) used GALEX photometry as one ingredient to derive SFRs and the total SFRD.

Arnouts et al. (2005) combined much deeper GALEX observations with spectroscopy from the VIMOS VLT Deep Survey (VVDS) and derived 1,500-Å rest-frame LFs at $0.2 < z < 1.2$. Schiminovich et al. (2005) integrated these LFs to determine the 1,500-Å luminosity density, measuring evolution consistent with $\rho_{\rm FUV} \propto (1+z)^{2.5}$. This remains the most direct and frequently cited GALEX study of FUV luminosity densities at $z < 1$, which is somewhat surprising, as there are many more deep GALEX observations in fields with extensive spectroscopy (COSMOS, AEGIS, GOODS, etc.). Yet, to our knowledge, there have been no other published LFs. The Arnouts/Schiminovich analysis is admirable, but it used only ~1,000 galaxies with spectroscopic redshifts over the whole range $\Delta z = 1$ in a single field covering 0.5 deg^2. Hence, it may be subject to cosmic variance issues. This area is ripe for further exploitation of existing archival data.

HST is the only other modern space telescope with UV capabilities, particularly with the UVIS channel of the WFC3 camera. Until recently, only one 50-arcmin^2 field in GOODS-South had been surveyed to interesting depths to study distant galaxies (Hathi et al. 2010, Oesch et al. 2010). At $z < 1.4$, where these data measure FUV rest-frame emission, the survey volume and counting statistics are poor. These data have also been used for Lyman break color selection at $z \approx 1.5$–2. The analyses generally support relatively steep UVLFs with $\alpha < -1.5$ with large uncertainties. Expanded WFC3 UVIS observations in the HUDF and GOODS-North field have been recently completed and should improve the existing measurements. A recent WFC3 UVIS survey of gravitationally lensed galaxies behind the massive cluster Abell 1689 (Alavi et al. 2013) has been used for Lyman break color selection to unprecedentedly faint FUV luminosities at $z \approx 2$ to $M_{AB} \approx -13$, or ~1,000 times fainter than L_* at that redshift. Alavi et al. (2013) found no turnover to the LF down to those limits and measured a faint-end slope $\alpha = -1.56 \pm 0.13$.

Cucciati et al. (2012) analyzed a larger, deeper and more complete spectroscopic sample in the same VVDS survey field studied by Arnouts et al. (2005) and Schiminovich et al. (2005). They fit SED models to multiband photometry from the *U*- to the *K*-bands to extrapolate flux density measurements to FUV rest-frame wavelengths at $z < 1.4$. They demonstrated consistency with the GALEX luminosity densities from Schiminovich et al. (2005) but did not make direct use of the GALEX data. Although the largest and deepest spectroscopic sample used to derive UVLFs at $0 < z < 2$, it is based on only one sightline and requires SED extrapolation to rest frame 1,500 Å at lower redshifts. Tresse et al. (2007) presented a similar, earlier analysis using shallower spectroscopy in two VVDS fields.

Over many years, Steidel and collaborators have carried out an extensive campaign of *Keck* spectroscopy for Lyman break–selected galaxies, especially at $z \approx 2$ and 3 (Steidel et al. 2003, 2004). Their survey covers many widely spread sightlines and provides excellent control over cosmic variance. Among several LF analyses from these data, the most recent and definitive are those of Reddy et al. (2008) and Reddy & Steidel (2009). These still rely on deep photometric color-selected samples to probe the faint end of the LF, but with a degree of spectroscopic confirmation and calibration for brighter galaxies that is unmatched by any other survey. The use of UV rest-frame selection means that any LBG-based study will miss heavily dust-obscured star formation at these redshifts, but as a measure of the evolving UV luminosity density, the LBG surveys have provided the most robust method to date.

At higher redshifts, $4 < z < 7$, deep HST observations (discussed below) have dominated surveys for LBGs in recent years, but several ground-based imaging programs have made significant

contributions, particularly surveying wider areas at (relatively) shallower depths to constrain the bright end of the LF. The *Subaru* telescope and its SuPrime Cam imager have been particularly important in this respect, although deep IR imaging from UKIRT and the VLT has also been used. Notable examples (not an exhaustive list) include Ouchi et al. (2004), Yoshida et al. (2006), Iwata et al. (2007), and McLure et al. (2009) at $z = 4$ to 6 and Ouchi et al. (2009), Castellano et al. (2010a,b), Bowler et al. (2012), and Tilvi et al. (2013) at $z \approx 7$.

The installation of the Advanced Camera for Surveys (ACS) enabled substantially more efficient optical HST imaging that covers fields much wider than the original HDF. ACS also offered significant gains in sensitivity at the reddest wavelengths, making Lyman break selection practical out to $z \approx 6$. Two major ACS surveys led to new derivations of the cosmic SFRD. GOODS (Giavalisco et al. 2004b) observed two independent fields with combined area >60 times larger than the HDF through four filters. This provided a sample of several thousand Lyman break candidates at $z \approx 4$ and of order 1,000 at $z \approx 5$, reaching significantly fainter than L_* and permitting robust characterization of the luminosity density. LBG selection at $z \approx 6$ was less secure from GOODS ACS data alone, as it was based on a single color ($i - z$) and could sample only relatively bright galaxies. The HUDF (Beckwith et al. 2006) observed a single ACS pointing ($\sim$11 arcmin^2) located within the GOODS-South region with very long exposure times and reaching fainter than the original HDF and with better sensitivity at higher redshifts. Both GOODS and the HUDF have been repeatedly revisited with new observations from HST over the years to add deeper optical imaging as well as NIR data, first from NICMOS (Thompson et al. 2006, Conselice et al. 2011) and later with WFC3 in the HUDF09 and HUDF12 programs (Bouwens et al. 2011b, Ellis et al. 2013) and the Cosmic Assembly Near-Infrared Deep Extragalactic Legacy Survey (CANDELS) of several premier deep survey fields including GOODS (Grogin et al. 2011, Koekemoer et al. 2011). These IR observations make Lyman break selection at $z \approx 6$ far more robust and extend the method out to $z \approx 8$, with a handful of unconfirmed candidates identified out to $z \approx 12$.

Early analyses of the GOODS data (Giavalisco et al. 2004a) found evidence for relatively mild evolution of the UV luminosity density from $2 < z < 5$ and clear evidence that there were fewer high-luminosity galaxies at $z \approx 6$ (Stanway et al. 2003, Dickinson et al. 2004). Subsequent studies have repeatedly mined the combined GOODS+HUDF observations, using deeper data and more rigorous analyses. At least 20 papers about high-redshift LFs using WFC3 data in the HUDF and GOODS/CANDELS have been published since 2010, augmenting at least a dozen others pre-WFC3. We cannot attempt to review them all here, but they have convincingly demonstrated that the UVLF evolves significantly at $z > 4$. The current consensus is that this is primarily luminosity evolution, at least at $4 < z < 7$, with L_* brightening over time (e.g., Bouwens et al. 2007, 2012b; Grazian et al. 2011). As a result, the number density of bright LBGs increases rapidly with time, more quickly than does the integrated luminosity density. Analyses using the CANDELS and HUDF09+12 NIR imaging point to continued evolution out to $z = 8$ and perhaps beyond (Oesch et al. 2012, Yan et al. 2012, Lorenzoni et al. 2013, Schenker et al. 2013), although it would be prudent to recall that only a handful of galaxies at $z \approx 7$ have reasonably secure spectroscopic confirmation and none at $z > 7.5$. There is broad agreement that UV spectral slopes for LBGs are bluer at $z > 4$ than at lower redshifts (Bouwens et al. 2012a, Finkelstein et al. 2012a, Dunlop et al. 2013), which has implications for their dust extinction and total SFRD. Most of these studies have examined the faint-end slope of the LF, measuring very steep values, in some cases approaching or exceeding the divergent value $\alpha = -2$ (Bouwens et al. 2012b, McLure et al. 2013). Several studies have also extended SFRD analyses to $9 < z < 12$, using data from the HUDF (Bouwens et al. 2011a, Ellis et al. 2013) or from lensing cluster studies (Coe et al. 2013). Although still in flux as better data accumulate, these measurements have considerable significance for the earliest phases of galaxy evolution and for the reionization of the IGM (e.g.,

Robertson et al. 2013), but relatively little impact on the global star-formation budget of the Universe. According to current estimates, only ~1% of the cosmic SMD present today was formed at $z > 6$.

4.2. Infrared Surveys

IRAS enabled the first measurements of the local far-infrared luminosity function (FIRLF) (Lawrence et al. 1986, Soifer et al. 1987, Saunders et al. 1990, Sanders et al. 2003). These were typically measured either at 60-μm observed wavelength or using FIR luminosities integrated over a broader wavelength range. They were also generally extrapolated from the measured IRAS fluxes using fitting formulas. Although various representations of FIR luminosity have been adopted, here we consider $L_{\rm IR}$ as the luminosity integrated over the range 8–1,000 μm, which encompasses most of the bolometric luminosity of dust emission from nearly all sources of interest. The longest wavelength IRAS band was at 100 μm, but AKARI extended all-sky FIR measurements out to 160 μm to provide more reliable measurements of the bolometric luminosity and reduced bias against galaxies with cold dust temperatures. Goto et al. (2011a,b) reanalyzed the local IRLF incorporating AKARI data. Despite differences in detail, the results are largely consistent with previous IRAS measurements in the luminosity range of overlap. LFs have also been measured for IRAS samples selected at 12 and 25 μm (Rush et al. 1993, Shupe et al. 1998). LFs at longer IR wavelengths were measured for (rather small) local samples with ISO [90 μm (Serjeant et al. 2004); 170 μm (Takeuchi et al. 2006)], *Herschel* (250–500 μm) (Dey et al. 2010, Vaccari et al. 2010), and with ground-based (sub)millimeter observations generally for IRAS-selected samples [1.2 mm (Franceschini et al. 1998); 850 μm (Dunne et al. 2000)]. New, large-area measurements using the largest *Herschel* surveys (e.g., H-ATLAS, covering 550 deg^2 with observations from 100 to 500 μm) have not yet appeared in the literature.

Nearly all studies found that the bright end of the IRLF cuts off less sharply than does the exponential used in the Schechter function. This has typically been modeled either as a double power law (e.g., Lawrence et al. 1986, Sanders et al. 2003) or as a combined log-normal and power law (e.g., Saunders et al. 1990). Locally, the bright end of the IRLF is dominated by galaxies with warmer dust temperatures, which tend to be starburst galaxies and dusty AGN (Saunders et al. 1990). Several studies have measured a steep faint-end slope α ($dN/dL \propto L^{\alpha}$), e.g., $\alpha = -1.6$ (Sanders et al. 2003), $\alpha = -1.8$ (Goto et al. 2011a), and $\alpha = -1.99$ (Goto et al. 2011b). However, other studies have found flatter distributions, e.g., $\alpha = -1.2$ to -1.0 (Saunders et al. 1990, Takeuchi et al. 2003, Vaccari et al. 2010). In practice, the faint end has not been well sampled locally except in a few of the IRAS surveys. Future analysis of the widest *Herschel* surveys may help resolve this.

In local, relatively quiescent spiral galaxies such as the Milky Way, more than half of the FIR luminosity is believed to arise, not from dust in active star-forming regions, but from dust in the general ISM that is heated by ambient starlight from intermediate- and older-age stellar populations (Lonsdale Persson & Helou 1987, Sodriski et al. 1997). The luminosity of the Milky Way is typical ($L_{\rm IR} \approx 10^{10}\,{\rm L}_{\odot}$) (Sodriski et al. 1997) compared with the knee of the local IRLF at $L^{*}_{\rm IR} = 10^{10.5}\,{\rm L}_{\odot}$ (Sanders et al. 2003). This implies that a significant fraction of the local IR luminosity density is not the direct result of young star formation. Thus, it may not be a good measure of the global SFR today. At higher redshift when the specific SFR of typical galaxies was much larger and the net dust extinction to star-forming regions was, on average, larger (see Section 5.1), we may expect the IRLF and its integral to more reliably trace the total SFRD. However, Salim et al. (2009) suggested that, even at higher redshift ($z \approx 0.7$), intermediate-age stars may significantly contribute to MIR dust emission observed by *Spitzer* at 24 μm.

The deepest surveys with ISO at 15 μm detected a few hundred galaxies, mainly at $z \leq 1$, in the HDF and a few other deep survey regions where spectroscopic and photometric redshifts

were available (Rowan-Robinson et al. 1997, Aussel et al. 1999, Flores et al. 1999). Analyses of these generally agreed that the emission from dusty star formation increased steeply with redshift, although statistics were generally too poor to construct redshift-dependent LFs. Chary & Elbaz (2001) used measurements from ISO and SCUBA as well as constraints from the FIR background as measured by the COBE satellite to constrain a model for the evolution of the cosmic SFH. Their model exhibited a sharp decline in the SFRD by a factor of 10 or more from $z \approx 0.8$ to the present, with a plateau of nearly constant star formation at $0.8 < z < 2$. At higher redshifts, the SFRD was more poorly constrained. Submillimeter sources placed a rough lower bound, whereas the cosmic infrared background (CIRB) set an upper limit. Acceptable solutions ranged from flat evolution to an increase by a factor of ~10 from $z = 4.5$ to 2.

Spitzer greatly enhanced the sensitivity and mapping efficiency for deep IR observations, particularly at 24 μm where the beam size (FWHM ≈ 5.7 arcsec) was small enough to enable relatively straightforward association with optical counterparts. *Spitzer* also observed in an era when very large spectroscopic redshift surveys were available or under way and when photometric redshift techniques were well established. Le Floc'h et al. (2005) produced an early, seminal analysis of 24-μm sources at $0.3 < z < 1.2$ in the Extended Chandra Deep Field South. Integrating over derived IRLFs, they inferred an evolution of the IR luminosity density proportional to $(1+z)^{3.9\pm0.4}$, significantly steeper than the evolving UV luminosity density, $\rho_{\rm FUV} \propto (1+z)^{2.5}$ (Schiminovich et al. 2005). With strong luminosity evolution, the fraction of the IR luminosity density produced by LIGs and ULIGs evolved even more steeply: Le Floc'h et al. (2005) found that galaxies with $L_{\rm IR} > 10^{11}\,{\rm L}_\odot$ produced 70% ± 15% of the IR luminosity density at $z \approx 1$, compared with ~5–15% today, depending on the adopted local LF. Several analyses of LFs, mainly at $z < 1$, using shallower *Spitzer* data covering significantly wider areas have also been published: These include Babbedge et al. (2006) and Rujopakarn et al. (2010) at 24 μm and Patel et al. (2013) at 70 μm and 160 μm. The work by Rujopakarn et al. (2010) is particularly notable for its combination of (relatively) wide area (9 deg^2), extensive spectroscopic redshifts (4,047 galaxies with $z \leq 0.65$), and 24-μm sensitivity (0.27 mJy, sufficient to reach $\sim L_*$ out to $z = 0.65$), making it arguably the best bridge study to date between local (IRAS and AKARI) measurements and deep-field studies at $z \geq 1$.

Several studies extended *Spitzer* 24-μm-based LF measurements to higher redshifts, $z \approx 2$ to 2.5 (Pérez-González et al. 2005, Caputi et al. 2007, Rodighiero et al. 2010). Such studies primarily use deeper 24-μm data and fainter spectroscopic and photometric redshifts available in the two GOODS fields. [Pérez-González et al. (2005) used shallower 24-μm data, whereas Caputi et al. (2007) and Rodighiero et al. (2010) employed deeper data from the GOODS team. Rodighiero et al. (2010) also incorporated relatively shallow *Spitzer* 24-μm data covering 0.85 deg^2 in one of the VVDS redshift survey fields.] Depending on the analysis, these studies all found flatter IR luminosity density evolution at higher redshifts with modestly lower or higher $\rho(L_{\rm IR})$ at $z = 2$ than at $z = 1$. All three studies also found that the characteristic IR luminosity $L^*_{\rm IR}$ brightened further at $z > 1$, such that ULIRGs emitted either close to 50% of the total energy density at $z \approx 2$ (Caputi et al. 2007, Rodighiero et al. 2010) or the majority of it (Pérez-González et al. 2005).

Depending on the data, methodology, and assumptions that are used, IRLFs estimated at high redshift have differed at both the faint and bright ends. At the faint end, the available data rarely constrain the slope of the LF at high redshift. Indeed, as noted above, there are significant differences in the faint-end slopes that have been measured at $z \approx 0$. Data with a limiting 24-μm flux density of 80 μJy (as found for most of the earlier *Spitzer* studies described above) reach only a factor of a few fainter than typical estimates of $L^*_{\rm IR}$ at $z \approx 1$, and they barely reach $L^*_{\rm IR}$ at $z \approx 2$. Thus, most analyses are forced to assume a faint-end slope based on measurements at lower redshifts, making them subject to large (typically >100%) and uncertain extrapolations to total IR luminosity densities.

Moreover, depending on the SED templates that are adopted, there are significant differences in the (large) extrapolations from observed MIR rest-frame measurements (e.g., 8-μm rest frame at $z = 2$) to the bolometric IR luminosity and SFR. Indeed, we expect such variations among real galaxies. Compared with several other studies, Pérez-González et al. (2005) found many more galaxies with $L_{IR} > 10^{12}\ L_{\odot}$ at $z \approx 2$, in part owing to different assumptions about these bolometric corrections. Also, different procedures to account for AGN emission (which can be particularly strong in the MIR) as well as heavy reliance on photometric redshifts may contribute to systematic issues in the IRLF, particularly at the bright end.

As we noted above (Section 3.1.2), several studies (Papovich et al. 2007, Daddi et al. 2007) stacked data at longer FIR wavelengths (e.g., 70 μm) or in radio and submillimeter data and found that standard SED templates such as those of Chary & Elbaz (2001) tend to overestimate typical bolometric corrections from observed 24-μm data for galaxies at $z \approx 2$. This suggested that true FIR measurements were needed to reliably determine luminosities and SFRs at high redshift. Huynh et al. (2007) made early measurements of the IRLF at $z < 1$ using the deepest available *Spitzer* 70-μm data in GOODS-North. The sample of detected sources was very small, but it was generally consistent with the earlier 24-μm work by Le Floc'h et al. (2005).

Magnelli et al. (2009, 2011) used comparably deep 70-μm data over a much wider area from the Far-Infrared Deep Extragalactic Legacy Survey to extend this work. In addition to counting detected sources (mostly at $z < 1.3$, given the depth of the 70-μm data), Magnelli et al. (2009, 2011) stacked 70-μm data in bins of 24-μm flux and redshift to measure empirically the average conversion between observed MIR and FIR luminosities. Compared with previous studies, they also used significantly deeper 24-μm catalogs extending down to 30 μJy in the GOODS fields. At $z < 1.3$, Magnelli et al. (2009) found that the average FIR over MIR flux ratios closely matched predictions from the template library of Chary & Elbaz (2001). They also measured LFs that were similar to previous measurements, but that extended to fainter luminosities significantly below the bend in the IRLF at $z \approx 1$ and with better statistics. At $z > 1.3$, however, Magnelli et al. (2011) confirmed previous suggestions that the average 70-μm to 24-μm flux ratios deviated systematically from the predictions of standard local SED templates. They extrapolated from the averaged 70-μm fluxes to the bolometric IRLF and found only a mild increase in L_* and the luminosity contribution of ULIRGs from $z \approx 1$ to 2. At lower redshifts, the faint-end slope was consistent with $\alpha = -1.6$ as measured for local IRAS galaxies by Sanders et al. (2003). By $z = 2$, the data reach only slightly fainter than the IRLF knee, and the slope is not constrained. However, extrapolating with a fixed slope $\alpha = -1.6$, Magnelli et al. (2011) found that the faint IRLF at $z = 2$ would be quite similar to that predicted by Reddy et al. (2008) on the basis of UV-selected galaxies and the dust absorption predicted from their UV spectral slopes.

The *Herschel Space Observatory* significantly improved sensitivity and reduced the beam size for FIR (70–500 μm) observations, and several large programs were dedicated to surveys of the most important multiwavelength-deep fields. Even the deepest *Herschel* surveys do not detect as many sources per square arcminute as are found in the deepest *Spitzer* 24-μm observations, but direct access to FIR wavelengths is invaluable for reliably estimating bolometric luminosities and SFRs at high redshift. Several analyses presented preliminary LFs out to $z = 2$ to 3 using data sets obtained early in the *Herschel* mission (Eales et al. 2010, Gruppioni et al. 2010, Lapi et al. 2011).

More extensive analyses of larger *Herschel* data sets have recently appeared in the literature. Gruppioni et al. (2013) used sources selected in *Herschel* PACS observations at 70, 100, and 160 μm in the two GOODS fields as well as shallower but wider observations of the Extended Chandra Deep Field South and COSMOS. They fit customized IR SED templates to photometry from both the PACS and SPIRE (250–500 μm) instruments and computed IR luminosities based on

spectroscopic and photometric redshifts. They derived LFs out to $z < 4.2$. However, at the highest redshifts ($3 < z < 4.2$), the data are sensitive only to the rarest hyperluminous sources. Limiting their analysis to $z < 2.3$, Magnelli et al. (2013) restricted their study to the deepest 70–160-μm data available in the GOODS fields and extracted FIR fluxes to still-fainter limits at positions of 24-μm-detected sources. Note that, as is often the case, the fields analyzed and the data used in these studies overlap considerably; even if the methods of analysis are different, they cannot be considered to be fully independent. That said, in their range of overlap, the two analyses are generally consistent: They find somewhat stronger luminosity evolution at $z > 1$ than in the *Spitzer* analysis of Magnelli et al. (2011) and, hence, demonstrate a larger contribution of ULIRGs to the total IR luminosity density at $z \approx 2$ [but not as large as in some earlier *Spitzer* studies, e.g., by Pérez-González et al. (2005)]. Magnelli et al. (2011) concluded that this difference (compared with their own very similar *Spitzer* analysis) is mainly due to better determination of the total IR luminosities of galaxies using the improved *Herschel* FIR measurements. Gruppioni et al. (2013) found that the characteristic luminosity $L^*_{\rm IR}$ continued to brighten at $z > 2$, albeit at a slower rate. Neither survey reliably measured the faint-end slope of the IRLF at high redshift, and both fixed it to values derived locally. Each study adopted distinct values: Magnelli et al. (2011) used $\alpha = -1.6$, whereas Gruppioni et al. (2013) used $\alpha = -1.2$. Given these different slopes, it is striking and perhaps surprising that these two analyses derive similar values for the total IR luminosity density at redshifts $0 < z < 2$. Broadly speaking, both studies find evolution by a factor of ∼6 between $z = 1.1$ and today and comparatively flat evolution at higher redshift to $\langle z \rangle = 2.05$ (Magnelli et al. 2011) and $\langle z \rangle = 2.75$ (Gruppioni et al. 2013), albeit with an increasing range of values allowed within the measurement uncertainties.

Figure 7 shows recent determinations of the IRLFs and UVLFs at $0 < z < 4$. The UVLFs in the figure show the observed luminosities uncorrected for extinction and are presented in units of solar luminosities for more direct comparison with the IRLFs. This figure illustrates several points that indicate low extinction for galaxies with lower SFRs and a significant contribution from low-luminosity galaxies to the global SFRD at high redshift.

1. Compared with the UVLFs, the IRLFs cut off less steeply at high luminosities.
2. The IRLFs extend to much higher luminosities than the UVLFs at the same redshifts, as the most actively star-forming galaxies tend to be strongly obscured by dust.
3. There is strong luminosity evolution, particularly for the IRLFs, but also in the UV, with more modest density evolution.
4. The UVLFs shown in **Figure 7** (from Cucciati et al. 2012) exhibit a trend toward steeper faint-end slopes at higher redshifts, especially for $z > 2$. Although this point lacks universal agreement, most studies do measure quite steep UVLFs at $z > 2$ and a trend toward bluer UV colors at faint luminosities.

Before *Spitzer* and *Herschel*, ground-based submillimeter bolometer arrays, especially SCUBA at JCMT, provided an essential glimpse at dusty star formation at very high redshifts. As is frequently noted, the negative *K* correction at submillimeter wavelengths approximately cancels luminosity distance dimming at $z > 1$. The flux limits of most submillimeter surveys constrain individual source detections to ultra- and hyperluminous galaxies, so that only the tip of the IRLF is sampled. In practice, the greatest limitation for deriving LFs or SFRD is identifying galaxy counterparts to submillimeter sources and measuring their redshifts. This limitation is due mainly to the large beam size of single-dish submillimeter observations, but it is also due to the fact that the optical counterparts are often very faint and sometimes invisible. Another consequence of the negative *K* correction is that substantial redshift uncertainties translate to only relatively small uncertainties in the bolometric luminosity. Hence, using radio-identified counterparts and

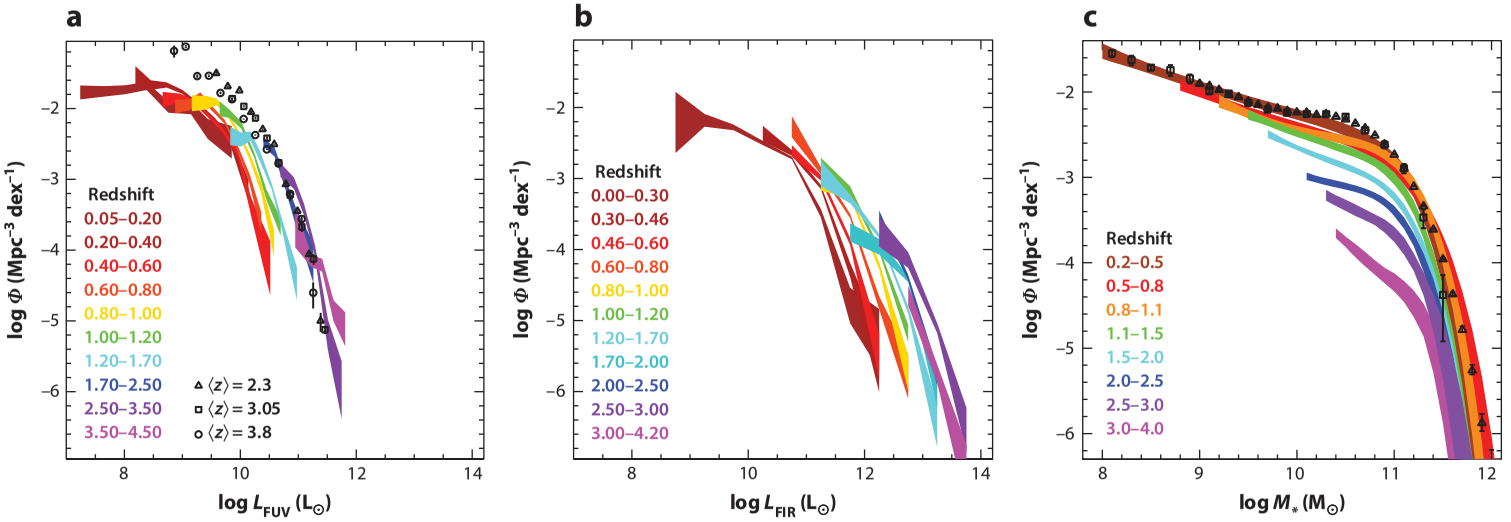

Figure 7

(*a*) Redshift evolution of the FUV luminosity function at $0 < z < 4$. The colored bands indicate the 68% confidence intervals on the space densities over the observed luminosities (uncorrected for dust attenuation), in different redshift ranges as indicated by the legend, from Cucciati et al. (2012). Data points, coded by shape, also as indicated in the legend, show the FUV luminosity functions for Lyman break galaxies at mean redshifts 2.3 and 3.05 from Reddy & Steidel (2009) and 3.8 from Bouwens et al. (2007). These luminosity functions use color selection techniques to extend the measurements to much fainter luminosities than those measured in the purely spectroscopic samples from Cucciati et al. (2012). The FUV luminosity functions at $2.3 < z < 3.8$ are observed to be quite similar. (*b*) Redshift evolution of the FIR luminosity function at $0 < z < 4$ from Gruppioni et al. (2013). The bands indicate the 68% confidence intervals at each redshift, as indicated by the color coding. (*c*) Galaxy stellar mass function at $0 < z < 4$ for a large, deep ($K_s < 24$) sample of 220,000 galaxies, from Ilbert et al. (2013). Once again, the bands correspond to the 68% confidence intervals at each redshift, including estimated uncertainties in the derived stellar masses. The open triangles and squares correspond to the local estimates by Moustakas et al. (2013) and Baldry et al. (2012), respectively. Abbreviations: FIR, far-infrared; FUV, far-UV. Panel *c* adapted from Ilbert et al. (2013).

very rough radio-millimetric redshift estimates, Barger et al. (2000) were able to make plausible estimates of the SFRD from submillimeter sources in broad redshift bins. Barger et al. (2012) recently updated their findings using a complete submillimeter galaxy (SMG) sample with accurate interferometric positions from the submillimeter array (SMA) and with more extensive redshift information, made possible in part thanks to recent advances in millimetric CO spectroscopy. Chapman et al. (2005) measured optical spectroscopic redshifts for a sample of radio-identified SMGs and derived the first SMG LFs at $\langle z \rangle = 0.9$ and $\langle z \rangle = 2.5$. These estimates were recently updated by Wardlow et al. (2011) using (mainly) photometric redshifts for another well-defined SMG sample. These analyses demonstrated a significant contribution of dusty SMGs to the cosmic SFRD at high redshift, mainly limited to $z \lesssim 4$. However, recent discoveries of substantial numbers of SMGs out to $z = 6.3$ (e.g., Riechers et al. 2013) suggest that the dusty ultraluminous population may be important even in the first few billion years of the cosmic SFH.

Although direct FIR detection of individual sources at $z \gg 2$ is limited to the most extremely luminous objects (**Figure 1**), the CIRB provides additional constraints on dusty star formation at the highest redshifts (Pei et al. 1999, Gispert et al. 2000). FIR source counts and the CIRB were reviewed by Lagache et al. (2005) and recent results from *Herschel* are reviewed by Lutz (2014) in this volume, so we only briefly discuss this topic here. Sources directly detected by *Herschel* in the deepest observations resolve ∼75% of the CIRB at 100 and 160 μm (Berta et al. 2011, Magnelli et al. 2013), albeit with significant uncertainties at 100 μm. Stacking *Herschel* data at the position of sources detected by Spitzer at 24 μm detects an even larger fraction that, with modest extrapolation, can account for the entire CIRB at these wavelengths. At 250 to 500 μm, where confusion is more severe in *Herschel* SPIRE data, the directly resolved fractions are smaller (from 15% to 5% at 250 to 500 μm), whereas stacking detects 73% to 55%. Again, an extrapolation is consistent with resolving the entire background (Béthermin et al. 2012). Because the deepest *Herschel* observations were carried out in fields such as GOODS and COSMOS with exceptional ancillary data, it is possible to stack in bins of photometric redshift to constrain the redshift distribution of the CIRB emission. At higher redshifts, the peak of dust emission from galaxies shifts to longer FIR and submillimeter wavelengths, and the fractional contribution of more-distant galaxies increases with the wavelength of the bandpass analyzed. Combining data from *Spitzer* through *Herschel* to ground-based submillimeter observations, Béthermin et al. (2012) estimated that 4.7 ± 2.0 nW m^{-2} sr^{-1}, or 17^{+11}_{-9}% of the integrated CIRB, is produced by galaxies at $z > 2$. Although the fraction is small, it still allows for a significant amount of dusty star formation to take place at $z > 2$, beyond what is seen in directly detected sources. However, the 24-μm sources used for these stacking analyses are also subject to strong *k*-correction dimming at $z > 2$. Thus, a larger fraction of the high-redshift CIRB may have been missed.

4.3. Emission Line Surveys

Among the nebular emission lines that have been most frequently used to quantify SFRs at high redshift, Hα is arguably the most useful (see Section 3.1.4). Lines from other elements, most commonly [OII] 3,727 Å, have also been used to measure the cosmic SFR (e.g., Hogg et al. 1998), but their more complex dependence on metallicity and ISM conditions as well as their larger extinction make them problematic. Narrow-band Lyα surveys are popular at high redshift, but Lyα is so strongly subject to resonant scattering and extinction that it must always be regarded as setting only a lower limit on the true SFR.

Hα is accessible with optical observations only at $z < 0.5$, and NIR observations are needed to follow it out to higher redshifts ($z \lesssim 2.5$). Recent technological developments in IR instrumentation have significantly increased the potential for such measurements. A new generation of

wide-field imagers using mosaics of IR arrays is now operating on 4-m- and 8-m-class telescopes (e.g., UKIRT WFCAM, CFHT WIRCAM, NOAO NEWFIRM, VISTA VIRCAM, VLT HAWK-I), thereby significantly increasing the comoving volumes accessible for deep narrow-band imaging. NIR multiobject spectrographs are now becoming mature and efficient (e.g., *Subaru* MOIRCS and FMOS, *Keck* MOSFIRE, VLT KMOS, LBT LUCI). Slitless grism spectroscopy with WFC3 on the HST can measure faint Hα lines out to $z < 1.5$ for all objects within its field of view. Each method has advantages and disadvantages. Narrow-band imaging surveys are tuned to specific, narrow redshift ranges and are strongly subject to density variations due to line-of-sight clustering effects. Flux calibration for objects whose redshifts place emission lines in the wings of the narrow bandpasses can also be problematic. Only statistical corrections can be made for the flux contribution from [NII] or for stellar absorption. Multislit spectroscopy is subject to slit losses that complicate measurements of integrated line fluxes, and atmospheric absorption and emission significantly limit the accessible redshifts and can introduce complicated selection effects. (The new VLT KMOS spectrograph uses multiple deployable integral field units, thus eliminating slit-loss concerns, and may prove to be a valuable tool for Hα surveys.) HST WFC3 slitless spectroscopy avoids concerns about the atmosphere and slit losses, but deep observations covering adequately large solid angles are time intensive. As of this writing, results on Hα LFs from the largest ongoing programs [WISPS (Atek et al. 2010) and 3D-HST (Brammer et al. 2012)] have not appeared in the literature to supersede earlier HST NICMOS results (Yan et al. 1999, Hopkins et al. 2000, Shim et al. 2009). With all methods, reliable extinction corrections depend on the measurement of the Balmer decrement (the ratio of Hα to Hβ line fluxes). This is rarely available for narrow-band surveys, but it is sometimes available for spectroscopic samples. However, in such cases, the sample selection is often limited by the weaker Hβ line. Hence, statistical corrections are often adopted. AGN and LINERs can also contribute significantly to the samples of emission line galaxies and can be reliably taken into account only using high-quality spectroscopic data to measure line-excitation diagnostics. Most careful studies of the local galaxy population using spectroscopy from SDSS or GAMA (see below) have done this, but it is rarely possible at higher redshifts. Thus, most studies have resorted to statistical corrections or none at all.

Much literature discusses LF and SFRD measurements from Hα, [OII] and [OIII], and we note only selected works here. Gunawardhana et al. (2013) included a thorough and up-to-date compilation of these measurements at low and high redshifts. Using objective prism photographic data, Gallego et al. (1995) presented an important early study of the local Hα LF. Subsequently, the SDSS provided a vast number of spectroscopic redshifts and line-flux measurements, although the small aperture size of the spectroscopic fibers requires careful and inevitably uncertain corrections to the total emission line flux for each galaxy. SDSS spectroscopy covers both Hα and Hβ and can provide a measurement of extinction via the Balmer decrement, although care is needed to account for stellar absorption, flux limits, and selection effects. Brinchmann et al. (2004) conducted a widely cited study of local star formation from SDSS optical spectroscopy and photometry. They used a full analysis of the emission and absorption line spectroscopy. Thus, their study was not strictly based on Hα alone, although the Balmer lines carry significant weight in the SFR determinations. As noted above, Salim et al. (2007) carried out an independent SDSS analysis based mainly on photometry including GALEX UV measurements but with extensive cross comparison to the Hα data. By using photometry, the Salim analysis bypasses uncertainties inherent in the spectroscopic Hα aperture corrections. The local SFRDs (normalized to $z = 0.1$) from the studies by Brinchmann et al. (2004) and Salim et al. (2007) agree extremely well. Most recently, Gunawardhana et al. (2013) combined data from the SDSS with significantly deeper (but also much smaller) fiber spectroscopy from the GAMA survey to probe fainter down the LF and extend the analysis to higher redshifts ($z < 0.35$).

Optical spectroscopic surveys have measured Hα SFRDs typically out to $z < 0.4$ (e.g., Tresse & Maddox 1998, Sullivan et al. 2000, Westra et al. 2010, Gunawardhana et al. 2013). Until recently, NIR spectroscopy was measured only for small samples, object by object, typically at $0.5 < z < 1.1$ (Glazebrook et al. 1999, Tresse et al. 2002, Doherty et al. 2006). In general, nebular line extinction is not directly measured and can only be assumed. The same is true for corrections for stellar absorption. Larger-scale and deeper spectroscopic surveys from a new generation of multiobject IR spectrographs on 8–10-m telescopes should be forthcoming.

Several studies have exploited slitless grism spectroscopy of Hα at $0.7 < z < 1.9$ from the HST NICMOS instrument (Yan et al. 1999, Hopkins et al. 2000, Shim et al. 2009). These studies are of small but relatively unbiased samples that are observed with relatively uniform sensitivity over a broad redshift range and without concerns for flux losses due to a finite spectrograph slit size. Once again, direct measurements of extinction are generally unavailable, and the low-resolution slitless spectroscopy inextricably blends Hα with [NII], thus requiring purely statistical corrections. New, more sensitive grism surveys with HST WFC3 that cover larger solid angles are under way.

The largest number of high-redshift measurements has come from narrow-band imaging surveys using wide-field CCD cameras out to $z \approx 0.4$ and with IR arrays at higher redshifts. These are generally carried out using filters that fit into spectral windows relatively unaffected by atmospheric absorption or emission and that correspond to specific redshifts ($z = 0.24$, 0.40, 0.84, 1.47, and 2.23 are all common). Using a new generation of wide-field imagers, the current state-of-the-art Hα surveys include those of Ly et al. (2007, 2011), Hayes et al. (2010), and Sobral et al. (2013). The latter survey (HiZELS) combines data from *Subaru* Suprime-Cam ($z = 0.40$) and UKIRT WFCAM ($z = 0.84$, 1.47 and 2.23): It covers ∼2 deg^2 in two survey fields, with deeper but narrower (0.03 deg^2) observations at $z = 2.23$ from the VLT and its HAWK-I imager. Between 500 and 1750 Hα emitters are detected in each redshift window, thereby providing good statistics. These authors measured a steady increase in the characteristic luminosity $L_*(\mathrm{H}\alpha)$ with redshift and a faint-end slope $\alpha \approx 1.6$ that is constant with redshift and is also similar to that found in most of the UV continuum surveys.

4.4. Radio Surveys

Centimeter-wavelength radio continuum emission from star-forming galaxies arises from a combination of flat-spectrum free-free emission, which is prominent at high frequencies, and steep spectrum synchrotron emission, which dominates at lower frequencies. Although the free-free emission should be a direct tracer of star-formation rates, it has been impractical to observe this at high redshift. However, the improved high-frequency sensitivity of the Jansky VLA should open this capability in the future. The lower-frequency emission arises mainly as a consequence of SNe. As such, it is also related to the SFR. In practice, its calibration as an SFR measurement is primarily empirical, e.g., based on the tight correlation observed between radio and far-IR emission for IRAS-selected galaxies in the local Universe (e.g., Yun et al. 2001). This correlation together with insensitivity to dust extinction makes radio emission an attractive wavelength for studying star formation.

Problematically, AGN can also produce powerful radio emission. Locally, radio sources with $L_\nu(1.4\,\mathrm{GHz}) > 10^{23}$ W Hz^{-1} are predominantly AGN. This radio luminosity corresponds to an SFR $> 94\,\mathrm{M}_\odot$ year^{-1}, using the conversion factor from Murphy et al. (2011) scaled to a Salpeter IMF. Such galaxies are extremely rare locally, so very powerful radio sources are commonly excluded as likely AGN. However, at $z > 1$, galaxies with these SFRs (corresponding to ULIRGs in terms of their IR luminosities) are common, even "normal" (see Section 3.1.2). Thus, it is problematic to disregard them simply on the basis of their radio emission. Other considerations

are needed to distinguish AGN from star-forming radio sources, such as radio spectral index, radio morphology, or radio/IR flux ratios, but these are all more difficult to measure, especially for very faint sources.

The local radio LF has been used to estimate the current SFRD in many studies (for recent examples, see Machalski & Godlowski 2000, Condon et al. 2002, Sadler et al. 2002, Serjeant et al. 2002, Mauch & Sadler 2007). In these studies, the authors carefully employed various criteria to separate AGN from star-forming galaxies. Data were often compared with IRAS IR measurements and excluded objects with a radio excess relative to their IR luminosities.

At $z > 1$, even the deepest VLA surveys have been able to detect galaxies with SFRs only $\gtrsim 100\,M_\odot$ year^{-1} (**Figure 1**) and $\gtrsim 1{,}000\,M_\odot$ year^{-1} at $z > 3$, although the Jansky VLA is now pushing to fainter sensitivities. Haarsma et al. (2000) were among the first to combine very deep VLA observations with spectroscopic and photometric redshift information to derive radio LFs and the cosmic SFRD at high redshift, primarily at $0.3 < z < 0.8$. However, they also considered one very broad bin from $1 < z < 4.4$. Based on individually detected radio sources, this work was updated in later studies that took advantage of more extensive multiwavelength data to distinguish AGN from star-forming galaxies. Seymour et al. (2008) identified AGN based on radio spectral indexes, radio morphology, and radio to NIR and MIR flux ratios. Smolčić et al. (2009) used optical SED criteria to identify star-forming galaxies detected in VLA 1.4 GHz data for COSMOS at more modest redshifts $z < 1.3$. Seymour et al. (2008) assumed pure luminosity evolution for the LF, consistent with the measurements by Smolčić et al. (2009) (and earlier by Haarsma et al. 2000). All these studies found broad agreement between the radio SFRD evolution and optical and IR surveys, noting a steep decline from $z = 1$ to 0; Seymour et al. (2008) measured a peak SFRD at $z \approx 1.5$, albeit with large uncertainties.

Other studies have used radio stacking to probe to fainter luminosities below the detection limits for individual sources—particularly, stacking for NIR samples that approximate stellar mass selection. Here, the assumption is that, as in the local Universe, radio sources at fainter luminosities will primarily trace star formation with relatively little AGN contribution. Dunne et al. (2009) stacked VLA 1.4 GHz and GMRT 610 MHz data for *K*-band-selected sources in bins of redshift and *K*-band luminosity. They found a linear (but redshift-dependent) relation between radio and NIR luminosity. Using a measurement of the evolving *K*-band LF from the same data set, they then used this radio/NIR ratio to extrapolate the observations to the total radio luminosity density and SFRD. Karim et al. (2011) used a large 1.4-GHz survey of COSMOS and a *Spitzer* 3.6-μm-selected sample to carry out the most extensive study of this sort to date. Stacking in bins of stellar mass and photometric redshift and converting the mean radio fluxes to SFRs, they extensively analyzed the SFR-M_* correlation and used this and the evolving stellar mass function (SMF) (from Ilbert et al. 2010) to compute the integrated SFRD. Dunne et al. (2009) measured a steady increase in the SFRD from $z \approx 0$ to a peak at $z \approx 1.5$ that declined at higher redshift to $z \approx 4$. By contrast, Karim et al. (2011) found a monotonic decline in the SFRD from $z = 3$ to today.

4.5. Stellar Mass Density Surveys

As the technology of NIR detectors advanced, so did surveys that used NIR photometry to better sample galaxies by stellar mass at both low and high redshifts (e.g., Cowie et al. 1996, Gavazzi et al. 1996). However, it was not until the turn of the millennium that authors started to routinely use stellar population synthesis models to convert photometry and redshift information to stellar masses for large samples of galaxies, especially at high redshift. Before the era of large, modern redshift surveys such as the SDSS and the 2dFGRS, several authors made estimates of the local baryonic densities and SMDs (Persic & Salucci 1992; Fukugita et al. 1998; Salucci & Persic 1999).

This effort accelerated, however, as new spectroscopic surveys mapped the local Universe. Cole et al. (2001) used 2dFGRS redshifts and NIR photometry from 2MASS to measure the local *K*-band LF more accurately than had previously been possible. Then, using stellar population modeling, they inferred stellar masses from the galaxy colors and luminosities and derived the local galaxy stellar mass function (GSMF) and the local comoving SMD. Bell et al. (2003) did the same using SDSS and 2MASS. Many studies have subsequently derived the GSMF from incrementally improving SDSS data releases, using additional ancillary data and a variety of methods for stellar population modeling; mass-to-light ratios are sometimes derived from photometry and from the SDSS spectra (Panter et al. 2007, Baldry et al. 2008, Li & White 2009). Moustakas et al. (2013) incorporated photometry from the UV (GALEX) to the MIR (WISE) in their analysis of the SDSS GSMF. Baldry et al. (2012) analyzed a sample from GAMA, a wide-area spectroscopic survey extending significantly fainter than the SDSS, modeling *M/L* from optical SDSS photometry. As the samples have grown larger, more elaborate functional forms have been fit to the GSMF, including double and even triple Schechter functions, and there is some evidence that the GSMF slope at low masses ($<10^9\ M_\odot$) may be steeper than was previously believed (e.g., $\alpha = -1.47$) (Baldry et al. 2012). Other authors have modeled stellar populations for ensembles of galaxies rather than deriving individual galaxy stellar masses, e.g., by fitting the integrated local luminosity densities for the entire local volume from UV to NIR wavelengths (Baldry & Glazebrook 2003) or by modeling coadded SDSS spectra in bins of luminosity, velocity dispersion, and 4,000-Å break strength (Gallazzi et al. 2008).

At higher redshifts, Brinchmann & Ellis (2000) derived stellar masses for galaxies at $z < 1$ in fields with both HST and NIR imaging. As expected given the declining cosmic SFRD at those redshifts, they found relatively little evolution in the integrated mass density at $0.4 < z < 0.9$ but a marked evolution in the mass breakdown by morphological type. Cohen (2002) similarly found no significant evolution in the SMD at $0.25 < z < 1.05$. Because the cosmic SFRD declines steeply with time at $z < 1$, relatively little new stellar mass accumulates in the late stages of cosmic history. Moustakas et al. (2013) recently broke new ground with a low-resolution prism spectroscopic survey measuring ~40,000 redshifts for galaxies at $0.2 < z < 1$ in five fields with *Spitzer* IRAC photometry covering 5.5 deg^2. Even with such outstanding data, the evolution in the overall SMF at $0 < z < 1$ is nearly imperceptible, but the migration of galaxies from the star-forming to the quiescent population is confirmed with exquisite detail.

Sawicki & Yee (1998), Giallongo et al. (1998), Papovich et al. (2001), and Shapley et al. (2001) pioneered the use of stellar population models to derive stellar masses for LBGs at $z \approx 2$–3. Giallongo et al. (1998) computed comoving SMDs out to $z \approx 4$ for galaxies from a relatively bright, optically selected sample, and measured steep evolution, but did not attempt to correct for unobserved galaxies fainter than the limits of their data. Subsequently, Dickinson et al. (2003), Fontana et al. (2003), and Rudnick et al. (2003) used the deepest NIR imaging then available for the two HDFs, HST NICMOS (HDF-N) and VLT ISAAC (HDF-S), together with extensive photometric and spectroscopic redshifts to derive the comoving SMD in several redshift bins out to $z \approx 3$. Strong evolution was found over that longer redshift baseline; the SMD at $z \approx 3$ measured in the range 5% to 15% of its present-day value, although a somewhat broader range of values would be permitted if systematic assumptions about the galaxy SFHs or stellar metallicities were pushed well beyond the range of models used for standard analysis. The SMD reached half its present-day value somewhere between $z = 2$ and 1. Strong cosmic variance in these small fields was also evident: At $z > 2$, red galaxies with high mass-to-light ratios were nearly absent in the HDF-N but were found in moderate abundance in the HDF-S. By contrast, the corresponding SMDs differed substantially. This indicated the importance of surveying larger fields and more sightlines, but obtaining IR imaging to satisfactory depth over

these larger regions of sky has proven to be very challenging and has required another decade of effort.

The launch of *Spitzer* and the impressive performance of its IRAC camera for imaging at 3.6 to 8 μm made it possible to measure rest-frame NIR photometry for galaxies at high redshift, and major public survey imaging campaigns such as GOODS, S-COSMOS, and SWIRE produced widely accessible and heavily used imaging data sets spanning a wide range of area-depth parameter space, ideal for deriving SMFs and densities at high redshift. Indeed, NIR imaging has struggled to catch up with IRAC in terms of comparable area-depth coverage. Despite the vast swaths of telescope time that have been invested in obtaining NIR data on popular fields such as GOODS and COSMOS, imaging at 1 to 2.5 μm still tends to fall short of *Spitzer*'s sensitivity at 3.6 and 4.5 μm. At $z > 4.5$, the ground-based *K*-band samples rest-frame UV wavelengths, and IRAC offers the only viable way to measure optical rest-frame light to constrain stellar masses.

From 2006 onward, most (although not all) papers on SMFs and densities at high redshift have made use of IRAC data—often in the same survey fields that are repeatedly analyzed. Among many other papers, Fontana et al. (2006), Pérez-González et al. (2008), Kajisawa et al. (2009), and Marchesini et al. (2009) analyzed stellar masses in the GOODS fields (sometimes in combination with other data sets) for galaxies out to $z \approx 4$. Arnouts et al. (2007), Pozzetti et al. (2010), Ilbert et al. (2010), and Brammer et al. (2011) analyzed wider-area but shallower surveys (e.g., COSMOS, VVDS-SWIRE, NMBS), generally focusing on redshifts $z \leq 2$. Despite differences in their methodologies, the conclusions of these papers painted a remarkably consistent picture of the evolution of the SMF at $0 < z < 3$, with very little change in its shape, characteristic mass M_*, or faint-end slope, but with steady evolution in the characteristic density ϕ^*. There are indications that the faint-end slope of the mass function may steepen at higher redshifts (e.g., Kajisawa et al. 2009, Santini et al. 2012). The integrated SMDs measured in the different analyses generally agreed within factors of 2 at most redshifts, and a consistent picture of mass build-up emerged.

Some of the most recent additions to this literature have taken advantage of deeper, wider NIR imaging from the largest-format cameras on 4-m-class telescopes (Bielby et al. 2012, Ilbert et al. 2013, Muzzin et al. 2013) to map relatively wide survey areas such as COSMOS or the CFHT Legacy Survey fields to depths previously reserved for small, deep surveys such as GOODS. Together with ever-growing spectroscopic surveys and increasingly excellent photometric redshifts, these have yielded the most statistically robust measurements of the SMFs at $z < 2.5$. However, several of these surveys repeat analysis in COSMOS. Some even use essentially the same imaging data sets, so these analyses are not always robust against cosmic variance.

Spitzer IRAC has been essential for deriving stellar masses at $z > 4$, and very deep observations are necessary to detect typical galaxies at those redshifts. For this reason, nearly all analyses of SMDs at $z > 4$ have been carried out in GOODS and the HUDF [in a departure from the GOODS-dominated norm, McLure et al. (2009) stacked relatively shallow IRAC data for LBGs at $z = 5$ and 6 in the UKIDSS Ultra Deep Survey to measure average SEDs and mass-to-light ratios and, hence, to estimate the SMD], and nearly all have studied UV-selected LBGs, for which there are abundant samples. Early analyses of small samples of galaxies at $z = 5$ and 6, including estimates of the integrated SMD, were presented by Yan et al. (2006), Eyles et al. (2007), Stark et al. (2007), Verma et al. (2007), and Yabe et al. (2009). These were followed by larger and more systematic analyses of LBG samples at $4 \geq z \geq 7$ (Stark et al. 2009, González et al. 2011, Lee et al. 2012), all of which used similar procedures and found broadly similar results. In particular, the derived LBG SMFs have somewhat shallower low-mass slopes than do the UVLFs, because M/L_{UV} decreases at fainter UV luminosities, at least at $z = 4$ and 5 where this could be measured with some robustness from galaxies with individual IRAC detections (e.g., Lee et al. 2012). Using

HST WFC3-selected samples in the HUDF and GOODS/CANDELS fields, Labbé et al. (2013) recently extended this analysis to $z \approx 8$.

Exceptionally, some studies have used IRAC selection to avoid the potential bias of UV selection against older or dustier galaxies. Caputi et al. (2011) analyzed an IRAC 4.5-μm-selected sample in the UKIDSS Ultradeep Survey, thereby computing SMDs at $3 \leq z \leq 5$. The depth of their IRAC data limited direct detections to a stellar mass completeness limit $\gtrsim 10^{10.4}\,M_\odot$. Their extrapolated mass densities based on Schechter function fits fall somewhat below those from other LBG-based studies (e.g., González et al. 2011, Lee et al. 2012), but this is likely due to uncertainties in the large extrapolation required. Several other authors have analyzed partially or wholly IRAC-selected candidates for massive galaxies at $z \gtrsim 3.5$ (Wiklind et al. 2008, Mancini et al. 2009, Marchesini et al. 2010, Caputi et al. 2012). In some cases, they have estimated comoving SMDs, although generally without fitting SMFs and often without rigorous analysis of sample completeness.

Several studies have suggested that LBGs at $z \gtrsim 4$ have much stronger optical rest-frame nebular line emission (particularly Hα and [OIII]) than do similar UV-selected galaxies at lower redshifts (Chary et al. 2005, Raiter et al. 2010, Shim et al. 2011, Labbé et al. 2013, Stark et al. 2013). In most cases, this has been inferred on the basis of *Spitzer* IRAC colors that would be unusual for pure stellar populations but that can be explained if strong line emission boosts the IRAC fluxes. This line emission, if not taken into account, can significantly affect derived stellar population parameters and generally leads to overestimated stellar masses. For LBG samples at $z = 4$ to 8, Stark et al. (2013) and Labbé et al. (2013) estimated that average stellar masses derived from models without nebular lines should be reduced by factors from 10% to 70%, with the effect increasing at higher redshifts. Although the photometric evidence for this strong nebular emission is compelling, it will be vitally important for JWST spectroscopy to confirm and quantify its effects.

4.6. The State of the Art, and What's Wrong with It

Galaxy evolution surveys have amassed a remarkable wealth of new data in the past two decades. Newer, larger, and deeper surveys have supplanted earlier work and have provided more statistically robust measurements of the SFR and stellar mass densities at many different redshifts. Nevertheless, there are still shortcomings in even the best data or in our use of those data, which may significantly limit the accuracy or reliability of measurements of the cosmic SFH. Here we consider the strengths and weaknesses of the best measurements to date, from the local Universe out to the highest redshifts.

4.6.1. Local measurements. To be statistically meaningful, measurements of the current SFR or SMD require surveys covering a large fraction of the sky. Salim et al. (2007) and Robotham & Driver (2011) used most or all of the GALEX Medium Imaging Survey data, covering ~1,000 deg^2 overlapping the SDSS and 2dFGRS spectroscopic surveys, and there is little prospect for improving the UV data in the near future. Only refinements in the analysis can be expected, e.g., incorporating improved photometric data at optical or NIR wavelengths, or further joint analysis with spectroscopic stellar population measurements. As discussed below (Section 5.1) (**Figure 8**), there is significant disagreement in the literature about the net FUV extinction correction at $z \approx 0$. Wide-area spectroscopic emission line surveys (e.g., from SDSS or GAMA) (Brinchmann et al. 2004, Gunawardhana et al. 2013) are limited by uncertain aperture corrections to line fluxes, whereas narrow-band imaging surveys have yet to cover enough galaxies over a wide enough area and are usually limited by the absence of direct measurements of extinction from the Balmer decrement, the [NII] contribution to Hα measurements, or the contribution of AGN emission. There is still room for progress in combined narrow-band plus spectroscopic data for large local

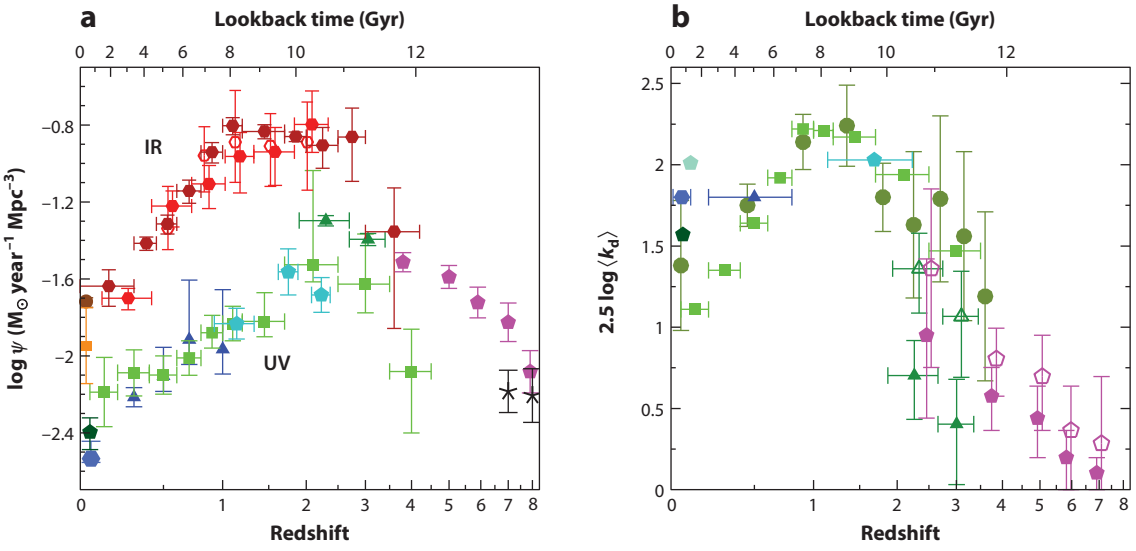

Figure 8

(*a*) SFR densities in the FUV (uncorrected for dust attenuation) and in the FIR. The data points with symbols are given in **Table 1**. All UV and IR luminosities have been converted to instantaneous SFR densities using the factors $\mathcal{K}_{\rm FUV} = 1.15 \times 10^{-28}$ and $\mathcal{K}_{\rm IR} = 4.5 \times 10^{-44}$ (cgs units) valid for a Salpeter IMF. (*b*) Mean dust attenuation in magnitudes as a function of redshift. Most of the data points shown are based on UV spectral slopes or stellar population model fitting. The symbol shapes and colors correspond to the data sets cited in **Table 1**, with the addition of Salim et al. (2007) (*cyan pentagon*). Two versions of the attenuation factors are shown for UV-selected galaxies at $2 < z < 7$ (Reddy & Steidel 2009, Bouwens et al. 2012a) (offset slightly in the redshift axis for clarity): one integrated over the observed population (*open symbols*), the other extrapolated down to $L_{\rm FUV} = 0$ (*filled symbols*). Data points from Burgarella et al. (2013) (*olive green dots*) are calculated by comparing the integrated FIR and FUV luminosity densities in redshift bins, rather than from the UV slopes or UV-optical spectral energy distributions. Abbreviations: FIR, far-infrared; FUV, far-UV; IMF, initial mass function; IR, infrared; SFR, star-formation rate.

samples. The local FIRLF has not been drastically revised since the final IRAS analyses (Sanders et al. 2003, Takeuchi et al. 2003); additional AKARI data did not drastically change earlier results (Goto et al. 2011a,b; Sedgwick et al. 2011). The biggest remaining uncertainties pertain to the faint-end slope, where measurements vary significantly from $\alpha = -1.2$ to -1.8 (or, somewhat implausibly, even -2.0) (e.g., Goto et al. 2011b). Analysis of the widest-area FIR surveys from *Herschel*, such as H-ATLAS (570 deg^2) (Eales et al. 2010), may help with this. The present uncertainties lead to a difference of a factor of at least 2 to 3 in the local FIR luminosity density. Nevertheless, as previously noted, in today's relatively "dead" epoch of cosmic star formation, a significant fraction of the FIR emission from ordinary spiral galaxies may arise from dust heated by intermediate-age and older stellar populations, not newly formed OB stars. Hence, it is not necessarily the best measure of the SFR. At higher redshifts, when the cosmic-specific SFR was much larger, new star formation should dominate dust heating, making the IR emission a more robust global tracer.

Local measurements of the SMD have relied mainly on purely optical data (e.g., SDSS photometry and spectroscopy) or on relatively shallow NIR data from 2MASS. There may still be concerns about missing light, surface brightness biases, etc., in the 2MASS data (e.g., Bell et al. 2003), and deeper very-wide-field NIR data would be helpful. All-sky MIR data from WISE may be valuable and have been used by Moustakas et al. (2013), but without extensive analysis specifically focused on this topic. Deeper NIR data covering a significant fraction of the sky, either from

new wide-field ground-based NIR telescopes with large apertures or from space-based surveys with EUCLID or WFIRST, would make a valuable new contribution. Otherwise, as for UV SFRs, the most likely improvements will come from refined stellar population analyses, rather than from new data.

4.6.2. $0 < z < 1$. During the decline and fall of cosmic star formation, from $z \approx 1$ to 0, the greatest weakness of current measurements is that they have generally covered small sky areas and small comoving volumes over few independent sightlines. Hence, they may be subject to significant cosmic variance uncertainties. Fields such as GOODS, which have been analyzed many times, are too small to offer precision measurements in fine redshift bins at $z < 1$. Even the 2 deg^2 COSMOS field subtends less than 100 Mpc at $z < 1$ and can be spanned by large-scale structure; as a single sightline, it is subject to density fluctuations. Although very good data for measuring the SFRD or SMD at $z < 1$ exist in many fields, relatively little information has been analyzed thoroughly, in part because intensive effort on spectroscopic (or even photometric) redshifts has been applied to only the few, most famous fields. Sometimes, even fields such as AEGIS, which has outstanding spectroscopy and deep GALEX, *Spitzer*, and *Herschel* data, have not been fully exploited for this purpose.

For example, very deep GALEX data exist for several of the most famous survey fields, but the one widely cited analysis of the UV luminosity density at $z < 1$ (Schiminovich et al. 2005) uses only ∼1,000 sources with redshifts in a single 0.5-deg^2 field. Expanded analysis of comparably deep GALEX data in COSMOS, AEGIS, and several other survey fields with existing, extensive spectroscopy is long overdue. There are no opportunities to collect more GALEX data, but deep *U*-band imaging measuring somewhat longer rest-frame UV wavelengths may be quite adequate for many purposes. Such data exist or could be obtained with wide-field imagers, but the best analysis to date (Cucciati et al. 2012), using ∼11,000 spectroscopic redshifts, is limited to a single 0.6-deg^2 sightline [indeed, the same field analyzed by Schiminovich et al. (2005) with GALEX]. Much more work can be done to improve this situation, with relatively limited new observational effort and often using data that already exist.

Similarly, most analyses of MIR and FIR data from *Spitzer* and *Herschel* data have used data from, at most, three independent sightlines (e.g., Magnelli et al. 2009, Rodighiero et al. 2010, Gruppioni et al. 2013), nearly always combining the two GOODS fields with one shallower but wider data set (e.g., COSMOS or the VVDS-SWIRE field). The widest-area analysis to date is that of Rujopakarn et al. (2010), which used 24-μm-selected sources at $z < 0.65$ from the 9-deg^2 Boötes survey. In practice, more data over more sightlines exist. Large consortium surveys such as the PEP and HerMES Herschel Guaranteed Time programs have mapped many fields, often with an elegant hierarchy of different areas and depths, but these have not yet been exploited and combined into a single, definitive analysis. Typically, this is because the ancillary imaging and spectroscopy needed to identify IR source counterparts and to determine their redshifts is available or adequate in only a few fields (hence, the repeated analyses of GOODS and COSMOS).

Many of these same comments apply to SMD estimates at $z < 1$. In this case, the state of the art has recently been improved by Moustakas et al. (2013), who analyzed five independent fields with a combined solid angle of 5.5 deg^2 with (relatively shallow) IRAC photometry and (low-resolution) spectroscopic redshifts. This is the best combination of area, depth, number of sightlines, and redshift quality for any study of the SMD at $z < 1$ and is also superior to any data used to date for SFRD studies at similar redshifts. Deeper ground-based NIR data were used by Bielby et al. (2012), who analyzed four fields covering 2.1 deg^2, and by several studies of the single 2-deg^2 COSMOS field (e.g., Ilbert et al. 2013). New wide-area surveys such as VISTA VIDEO (Jarvis 2012) (ground-based NIR, three fields, 12 deg^2) and SERVS (Mauduit et al. 2012) (*Spitzer* IRAC, five fields, 18 deg^2, overlapping VIDEO) will provide excellent new data to improve mass

function estimates, but only if adequate redshift information and supporting optical photometry are available.

4.6.3. $1 < z < 4$. At $z > 1$, deep surveys are needed to probe typical (L_* and fainter) luminosities and to directly detect the majority of cosmic star formations. In principle, many fields have suitable data. However, in practice, a few survey fields have been reanalyzed many times, in part because they have the best spectroscopic and photometric redshift measurements and in part because they have the richest multiwavelength data. As such, they are magnets for studies of all kinds. In the UV, the 1,500-Å rest frame is easily probed at $z > 1.5$ using ground-based or HST optical imaging. At $z \approx 2$ and 3, the surveys of LBGs by Steidel and collaborators (e.g., Reddy & Steidel 2009) cover many independent sightlines. They offer excellent control of cosmic variance and have outstanding spectroscopic calibration. UV selection is biased against dusty star formation, but for pure measurements of the UVLF, their surveys are arguably definitive. The best direct measurements of dust emission from *Spitzer* and *Herschel* are limited to fewer fields, and still fewer have the very deep data needed to probe galaxies near L_*. As described above, most analysis has revolved around GOODS and COSMOS, and even in GOODS, the *Herschel* data only barely reach L_* at $z = 2$. The faint-end slope of the IRLF is not directly constrained by individually detected sources at $z > 2$, leading to potentially large uncertainties in any extrapolation to the bolometric IR luminosity density. With no more sensitive FIR space missions on the horizon, there is little prospect for wide-area surveys to fainter flux limits. ALMA can reach fainter submillimeter continuum limits and detect dust continuum from ordinary galaxies at very high redshifts, but only for very small solid angles. Mosaics of hundreds or even thousands of pointings would be needed to survey a field the size of GOODS. Well-designed observations targeting intelligently selected galaxy samples, rather than panoramic mapping, may be required.

Stellar masses below the characteristic mass M_* can be probed using the best ground-based NIR data and using *Spitzer* IRAC even with modest integration times. Thus, more fields have been analyzed, although GOODS and COSMOS still tend to dominate the literature. The extended *Spitzer* warm mission generated a wealth of valuable data that has yet to be fully exploited. In practice, there is uncannily good agreement between most determinations of the SMF and density at $1 < z < 4$, and it is not clear that new surveys are needed, rather than more sophisticated analysis of the existing data. However, the CANDELS HST WFC3 survey reaches fainter multiband NIR fluxes in fields that already have the deepest IRAC data and, hence, provides an important opportunity for measuring photometric redshifts and stellar masses for galaxies fainter than the limits of most studies to date. This should provide a better constraint on the slope of the SMF at low masses.

4.6.4. $z > 4$. At $z \geq 4$, the large majority of UV-based SFR and SMD measurements have been derived from HST data, mainly in the GOODS fields and the HUDF plus its deep parallel fields (also located in and around GOODS-South). Although ground-based imaging can select galaxies at $z \geq 4$, in practice the HST surveys have gone deeper, especially at the very red optical wavelengths (I- and z-bands) and the NIR wavelengths needed to select galaxies at the highest redshifts; only with these data can LF measurements probe significantly fainter than L_*. GOODS also has the deepest *Spitzer* IRAC data, essential for deriving stellar masses at $z > 4$, where even the K-band samples rest-frame UV wavelengths. Although the comoving volumes in the GOODS fields are significant at these large redshifts (nearly 10^6 comoving Mpc^3 at $z = 4$ for the combined GOODS fields), one may still worry about clustering and cosmic variance, given only two sightlines. The CANDELS program (Grogin et al. 2011, Koekemoer et al. 2011) is obtaining multiband optical and NIR HST imaging over five fields, each similar in size, including the two GOODS fields. This program is supplemented by very deep IRAC imaging from SEDS (Ashby et al. 2013) and

S-CANDELS (G. Fazio, research in progress) and will help with cosmic variance control and improved statistics.

At $6 < z < 8$, the HUDF data become essential to get any handle on the faint-end slope of the LF, and one must worry about the very small field size. At $z > 8$, the HUDF (or lensing clusters) are needed to detect convincing candidates. Hence, nearly all the literature on the SFRD or stellar masses at these redshifts consists of serial and parallel analyses of the same HUDF data sets as well as recent work from CLASH (Zheng et al. 2012, Coe et al. 2013). Here, the new Hubble Frontier Fields should be important. This program, to be executed from 2013 to 2016, will obtain multiband optical and NIR HST imaging with near-HUDF depth along with ultradeep *Spitzer* IRAC data for six massive galaxy clusters. Its lensing potential will magnify the faintest high-redshift background galaxies. In addition, there will be six new "blank" parallel fields that will improve statistics for unlensed sources and provide cosmic variance control for analyses that now depend on the HUDF (and its satellites) alone.

At $z > 4$, galaxies detected in ground-based NIR data (and at $z > 3$ for HST observations in the reddest WFC3-IR filters) are observed at rest-frame UV wavelengths. Hence, even with CANDELS, the HUDF, and the Frontier Fields, HST selection will be biased against quiescent or dusty galaxies. Massive galaxies with huge SFRs that are detected at submillimeter wavelengths but invisible even out to the *K*-band have been detected. Redshifts $z > 4$ have been confirmed from CO measurements (e.g., Daddi et al. 2009), but it is unknown how much they might contribute to the SFR or SMD. IRAC selection should, in principle, provide a less biased census (e.g., Mancini et al. 2009; Huang et al. 2011; Caputi et al. 2011, 2012), but spectroscopic confirmation or even photometric redshift estimates for this population may prove to be very difficult before the launch of the JWST.

5. FROM OBSERVATIONS TO GENERAL PRINCIPLES

Equation 1 was first used by Lanzetta et al. (1995) to study the chemical evolution of the damped Lyα absorption systems, where one infers the comoving rate of star formation from the observed cosmological mass density of HI; Pei & Fall (1995) then generalized it to models with inflows and outflows. Madau et al. (1996, 1998b) and Lilly et al. (1996) developed a different method where data from galaxy surveys were used to infer the SFRD $\psi(t)$ directly. This new approach relies on coupling the equations of chemical evolution to the spectrophotometric properties of the cosmic volume under consideration. The specific luminosity density at time t of a "cosmic stellar population" characterized by an SFRD $\psi(t)$ and a metal-enrichment law $Z_*(t)$ is given by the convolution integral

$$\rho_\nu(t) = \int_0^t \psi(t-\tau)\mathcal{L}_\nu[\tau, Z_*(t-\tau)]\mathrm{d}\tau, \qquad (13)$$

where $\mathcal{L}_\nu[\tau, Z_*(t-\tau)]$ is the specific luminosity density radiated per unit initial stellar mass by a SSP of age τ and metallicity $Z_*(t-\tau)$. The theoretical calculation of $\mathcal{L}_\nu$ requires stellar evolutionary tracks, isochrones, and stellar atmosphere libraries. As an illustrative example of this technique, we provide in this section a current determination of the SFH of the Universe and discuss a number of possible implications.

5.1. Star-Formation Density

Rather than trying to be exhaustive, we base our modeling below on a limited number of contemporary (mostly post-2006) galaxy surveys (see **Table 1**). For the present purpose, we consider only surveys that have measured SFRs from rest-frame FUV (generally 1,500 Å) or MIR

Table 1 Determinations of the cosmic star-formation rate density from UV data (*top group*) and infrared data (*bottom group*) used in this review

Reference(s)	Redshift range	A_{FUV}[a] [mag]	log ψ[b] [$M_\odot$ year^{-1} Mpc^{-3}]	Symbols used in Figure 9
Wyder et al. (2005)	0.01–0.1	1.80	$-1.82^{+0.09}_{-0.02}$	Blue-gray hexagon
Schiminovich et al. (2005)	0.2–0.4	1.80	$-1.50^{+0.05}_{-0.05}$	Blue triangles
	0.4–0.6	1.80	$-1.39^{+0.15}_{-0.08}$	
	0.6–0.8	1.80	$-1.20^{+0.31}_{-0.13}$	
	0.8–1.2	1.80	$-1.25^{+0.31}_{-0.13}$	
Robotham & Driver (2011)	0.05	1.57	$-1.77^{+0.08}_{-0.09}$	Dark green pentagon
Cucciati et al. (2012)	0.05–0.2	1.11	$-1.75^{+0.18}_{-0.18}$	Green squares
	0.2–0.4	1.35	$-1.55^{+0.12}_{-0.12}$	
	0.4–0.6	1.64	$-1.44^{+0.10}_{-0.10}$	
	0.6–0.8	1.92	$-1.24^{+0.10}_{-0.10}$	
	0.8–1.0	2.22	$-0.99^{+0.09}_{-0.08}$	
	1.0–1.2	2.21	$-0.94^{+0.09}_{-0.09}$	
	1.2–1.7	2.17	$-0.95^{+0.15}_{-0.08}$	
	1.7–2.5	1.94	$-0.75^{+0.49}_{-0.09}$	
	2.5–3.5	1.47	$-1.04^{+0.26}_{-0.15}$	
	3.5–4.5	0.97	$-1.69^{+0.22}_{-0.32}$	
Dahlen et al. (2007)	0.92–1.33	2.03	$-1.02^{+0.08}_{-0.08}$	Turquoise pentagons
	1.62–1.88	2.03	$-0.75^{+0.12}_{-0.12}$	
	2.08–2.37	2.03	$-0.87^{+0.09}_{-0.09}$	
Reddy & Steidel (2009)	1.9–2.7	1.36	$-0.75^{+0.09}_{-0.11}$	Dark green triangles
	2.7–3.4	1.07	$-0.97^{+0.11}_{-0.15}$	
Bouwens et al. (2012a,b)	3.8	0.58	$-1.29^{+0.05}_{-0.05}$	Magenta pentagons
	4.9	0.44	$-1.42^{+0.06}_{-0.06}$	
	5.9	0.20	$-1.65^{+0.08}_{-0.08}$	
	7.0	0.10	$-1.79^{+0.10}_{-0.10}$	
	7.9	0.0	$-2.09^{+0.11}_{-0.11}$	
Schenker et al. (2013)	7.0	0.10	$-2.00^{+0.10}_{-0.11}$	Black crosses
Sanders et al. (2003)	0.03	NA	$-1.72^{+0.02}_{-0.03}$	Brown circle
Takeuchi et al. (2003)	0.03	NA	$-1.95^{+0.20}_{-0.20}$	Dark orange square
Magnelli et al. (2011)	0.40–0.70	NA	$-1.34^{+0.22}_{-0.11}$	Red open hexagons
	0.70–1.00	NA	$-0.96^{+0.15}_{-0.19}$	
	1.00–1.30	NA	$-0.89^{+0.27}_{-0.21}$	
	1.30–1.80	NA	$-0.91^{+0.17}_{-0.21}$	
	1.80–2.30	NA	$-0.89^{+0.21}_{-0.25}$	
Magnelli et al. (2013)	0.40–0.70	NA	$-1.22^{+0.08}_{-0.11}$	Red filled hexagons
	0.70–1.00	NA	$-1.10^{+0.10}_{-0.13}$	
	1.00–1.30	NA	$-0.96^{+0.13}_{-0.20}$	
	1.30–1.80	NA	$-0.94^{+0.13}_{-0.18}$	
	1.80–2.30	NA	$-0.80^{+0.18}_{-0.15}$	

(*Continued*)

Table 1 (*Continued*)

Reference(s)	Redshift range	A_{FUV}[a] [mag]	log ψ[b] [$M_\odot$ year^{-1} Mpc^{-3}]	Symbols used in Figure 9
Gruppioni et al. (2013)	0.00–0.30	NA	$-1.64^{+0.09}_{-0.11}$	Dark red filled hexagons
	0.30–0.45	NA	$-1.42^{+0.03}_{-0.04}$	
	0.45–0.60	NA	$-1.32^{+0.05}_{-0.05}$	
	0.60–0.80	NA	$-1.14^{+0.06}_{-0.06}$	
	0.80–1.00	NA	$-0.94^{+0.05}_{-0.06}$	
	1.00–1.20	NA	$-0.81^{+0.04}_{-0.05}$	
	1.20–1.70	NA	$-0.84^{+0.04}_{-0.04}$	
	1.70–2.00	NA	$-0.86^{+0.02}_{-0.03}$	
	2.00–2.50	NA	$-0.91^{+0.09}_{-0.12}$	
	2.50–3.00	NA	$-0.86^{+0.15}_{-0.23}$	
	3.00–4.20	NA	$-1.36^{+0.23}_{-0.50}$	

[a]In our notation, $A_{FUV} \equiv -2.5\log_{10}\langle k_d \rangle$.
[b]All our star-formation rate densities are based on the integration of the best-fit luminosity function parameters down to the same relative limiting luminosity, in units of the characteristic luminosity L_*, of $L_{min} = 0.03L_*$. A Salpeter initial mass function has been assumed.
Abbreviation: NA, not applicable.

and FIR measurements. Other surveys of nebular line or radio emission are also important, but they provide more limited or indirect information as discussed in previous sections (Sections 4.3 and 4.4). For the IR measurements, we emphasize surveys that make use of FIR data from *Spitzer* or *Herschel*, rather than relying on MIR (e.g., *Spitzer* 24-μm) measurements alone, owing to the complexity and lingering uncertainty over the best conversions from MIR luminosity to SFR, particularly at high redshift or high luminosity. In a few cases, we include older measurements when they are the best available, particularly for local luminosity densities from IRAS or GALEX, or GALEX-based measurements at higher redshifts that have not been updated since 2005.

For rest-frame FUV data, we use local GALEX measurements by Wyder et al. (2005) and Robotham & Driver (2011) and also include the 1,500-Å GALEX measurements at $z < 1$ from Schiminovich et al. (2005). We use the FUV luminosity densities of Cucciati et al. (2012) at $0.1 < z < 4$, noting that for $z < 1$ these are extrapolations from photometry at longer UV rest-frame wavelengths. At $1 \lesssim z \lesssim 3$ we also use FUV luminosity densities from Dahlen et al. (2007) and Reddy & Steidel (2009). At redshifts $4 \leq z \leq 8$, there are a plethora of HST-based studies, with some groups of authors repeatedly reanalyzing samples in GOODS and the HUDF as new and improved data have accumulated. We restrict our choices to a few of the most recent analyses, taking best-fit Schechter parameters (ϕ^*, L_*, α) from Bouwens et al. (2012b) and Schenker et al. (2013). For the present analysis, we stop at $z = 8$ and do not consider estimates at higher redshifts.

For local IR estimates of the SFRD, we use IRAS LFs from Sanders et al. (2003) and Takeuchi et al. (2003). At $0.4 < z < 2.3$, we include data from Magnelli et al. (2009, 2011), who used stacked *Spitzer* 70-μm measurements for 24-μm-selected sources. We also use the *Herschel* FIRLFs of Gruppioni et al. (2013) and Magnelli et al. (2013). Although both groups analyze data from the GOODS fields, Gruppioni et al. (2013) incorporate wider/shallower data from COSMOS. By contrast, Magnelli et al. (2013) include the deepest 100- and 160-μm data from GOODS-*Herschel*, extracting sources down to the faintest limits using 24-μm prior positions.

All the surveys used here provide best-fit LF parameters—generally Schechter functions for the UV data, but other functions for the IR measurements, such as double power laws or the

function by Saunders et al. (1990). These allow us to integrate the LF down to the same relative limiting luminosity in units of the characteristic luminosity L_*. We adopt an integration limit $L_{\rm min} = 0.03L_*$ when computing the luminosity density $\rho_{\rm FUV}$ or $\rho_{\rm IR}$. For the case of a Schechter function, this integral is

$$\rho_{\rm FUV}(z) = \int_{0.03L_*}^{\infty} L\phi(L, z){\rm d}L = \Gamma(2 + \alpha, 0.03)\phi^* L_*. \quad (14)$$

Here α denotes the faint-end slope of the Schechter parameterization, and Γ is the incomplete gamma function. The integrated luminosity density has a strong dependence on $L_{\rm min}$ at high redshift, where the faint-end slope is measured to be very steep, i.e., $\alpha = -2.01 \pm 0.21$ at $z \sim 7$ and $\alpha = -1.91 \pm 0.32$ at $z \sim 8$ (Bouwens et al. 2011b). Slopes of $\alpha \lesssim -2$ lead to formally divergent luminosity densities. Our choice of a limiting luminosity that is 3.8 magnitudes fainter than L_*, although it samples a significant portion of the faint-end of the FUV LF, requires only a mild extrapolation (1.3 mag) from the deepest HST WFC3/IR observations (∼2.5 mag beyond L_* at $z \sim 5$–8) of the HUDF (Bouwens et al. 2011b). For the IR data, we use analytic or numerical integrations depending on the LF form adopted by each reference, but the same faint-end slope considerations apply. (Note, however, that some authors use logarithmic slopes for IRLFs, which differ from the linear form used in the standard Schechter formula by $\Delta\alpha = +1$.)

Multiplying the integrated FUV and IR comoving luminosity densities by the conversion factors $\mathcal{K}_{\rm FUV}$ (Section 3.1.1) and $\mathcal{K}_{\rm IR}$ (Section 3.1.2), we obtain measurements of the "observed" UV and IR SFRDs (shown in **Figure 8**). Here, the FUV measurements are uncorrected for dust attenuation. This illustrates the now well-known result that most of the energy from star-forming galaxies at $0 < z < 2$ is absorbed and reradiated by dust; only a minority fraction emerges directly from galaxies as UV light. The gap between the UV and IR measurements increases with redshift out to at least $z \approx 1$ and then may narrow from $z = 1$ to 2. Robust measurements of the FIR luminosity density are not yet available at $z > 2.5$.

Clearly, a robust determination of dust attenuation is essential to transform FUV luminosity densities into total SFRDs. **Figure 8** shows measurements of the effective dust extinction, $\langle k_d \rangle$, as a function of redshift. This is the multiplicative factor needed to correct the observed FUV luminosity density to the intrinsic value before extinction or, equivalently, $\langle k_d \rangle = \rho_{\rm IR}/\rho_{\rm FUV} + 1$ (e.g., Meurer et al. 1999). For most of the data shown in **Figure 8**, the attenuation has been estimated from the UV spectral slopes of star-forming galaxies using the attenuation-reddening relations from Meurer et al. (1999) or Calzetti et al. (2000) or occasionally from stellar population model fitting to the full UV-optical SEDs of galaxies integrated over the observed population (e.g., Salim et al. 2007, Cucciati et al. 2012). Robotham & Driver (2011) used the empirical attenuation correction of Driver et al. (2008). We note that the estimates of UV attenuation in the local Universe span a broad range, suggesting that more work needs to be done to firmly pin down this quantity (and perhaps implying that we should be cautious about the estimates at higher redshift). Several studies of UV-selected galaxies at $z \geq 2$ (Reddy & Steidel 2009, Bouwens et al. 2012a, Finkelstein et al. 2012b) have noted strong trends for less luminous galaxies as having bluer UV spectral slopes and, hence, lower inferred dust attenuation. Because the faint-end slope of the far-UV luminosity function (FUVLF) is so steep at high redshift, a large fraction of the reddened FUV luminosity density is emitted by galaxies much fainter than L_*; this extinction-luminosity trend also implies that the net extinction for the entire population will be a function of the faint integration limit for the sample. In **Figure 8**, the points from Reddy & Steidel (2009) (at $z = 2.3$ and 3.05) and from Bouwens et al. (2012a) (at $2.5 \leq z \leq 7$) are shown for two faint-end integration limits: These are roughly down to the observed faint limit of the data, $M_{\rm FUV} < -17.5$ to -17.7 for the different redshift subsamples and extrapolated to $L_{\rm FUV} = 0$. The net attenuation for the

brighter limit, which more closely represents the sample of galaxies actually observed in the study, is significantly larger than for the extrapolation—nearly two times larger for the Reddy & Steidel (2009) samples and by a lesser factor for the more distant objects from Bouwens et al. (2012a). In our analysis of the SFRDs, we have adopted the mean extinction factors inferred by each survey to correct the corresponding FUV luminosity densities.

Adopting a different approach, Burgarella et al. (2013) measured total UV attenuation from the ratio of FIR to observed (uncorrected) FUV luminosity densities (**Figure 8**) as a function of redshift, using FUVLFs from Cucciati et al. (2012) and *Herschel* FIRLFs from Gruppioni et al. (2013). At $z < 2$, these estimates agree reasonably well with the measurements inferred from the UV slope or from SED fitting. At $z > 2$, the FIR/FUV estimates have large uncertainties owing to the similarly large uncertainties required to extrapolate the observed FIRLFs to a total luminosity density. The values are larger than those for the UV-selected surveys, particularly when compared with the UV values extrapolated to very faint luminosities. Although galaxies with lower SFRs may have reduced extinction, purely UV-selected samples at high redshift may also be biased against dusty star-forming galaxies. As we noted above, a robust census for star-forming galaxies at $z \gg 2$ selected on the basis of dust emission alone does not exist, owing to the sensitivity limits of past and present FIR and submillimeter observatories. Accordingly, the total amount of star formation that is missed from UV surveys at such high redshifts remains uncertain.

Figure 9 shows the cosmic SFH from UV and IR data following the above prescriptions as well as the best-fitting function

$$\psi(z) = 0.015 \frac{(1+z)^{2.7}}{1+[(1+z)/2.9]^{5.6}}\ \mathrm{M_\odot\ year^{-1}\ Mpc^{-3}}. \qquad (15)$$

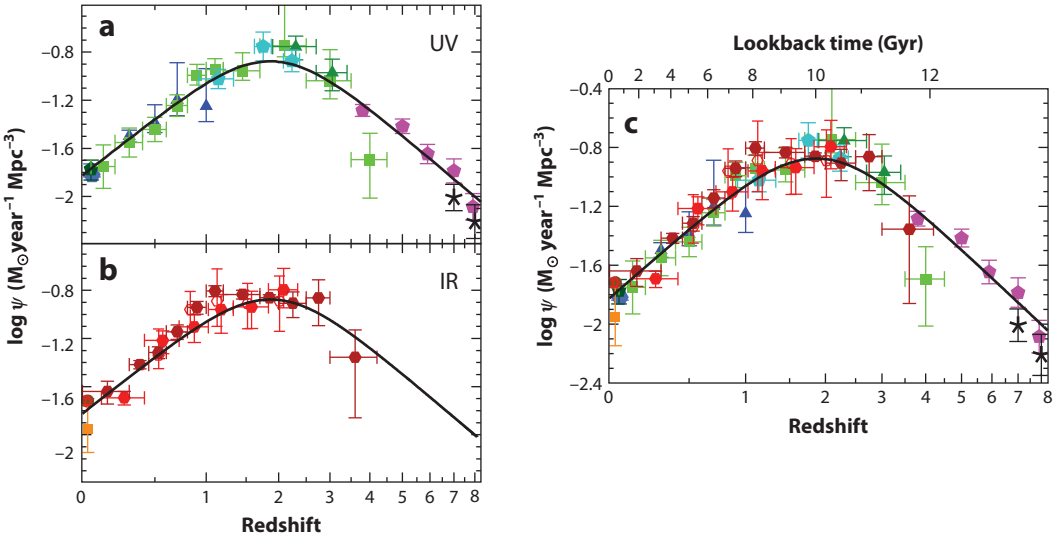

Figure 9

The history of cosmic star formation from (*a*) FUV, (*b*) IR, and (*c*) FUV+IR rest-frame measurements. The data points with symbols are given in **Table 1**. All UV luminosities have been converted to instantaneous SFR densities using the factor $\mathcal{K}_{\mathrm{FUV}} = 1.15 \times 10^{-28}$ (see Equation 10), valid for a Salpeter IMF. FIR luminosities (8–1,000 μm) have been converted to instantaneous SFRs using the factor $\mathcal{K}_{\mathrm{IR}} = 4.5 \times 10^{-44}$ (see Equation 11), also valid for a Salpeter IMF. The solid curve in the three panels plots the best-fit SFR density in Equation 15. Abbreviations: FIR, far-infrared; FUV, far-UV; IMF, initial mass function; IR, infrared; SFR, star-formation rate.

These state-of-the-art surveys provide a remarkably consistent picture of the cosmic SFH: a rising phase, scaling as $\psi(z) \propto (1+z)^{-2.9}$ at $3 \lesssim z \lesssim 8$, slowing and peaking at some point probably between $z = 2$ and 1.5, when the Universe was ~3.5 Gyr old, followed by a gradual decline to the present day, roughly as $\psi(z) \propto (1+z)^{2.7}$. The comoving SFRD at redshift 7 was approximately the same as that measured locally. The increase in $\psi(z)$ from $z \approx 8$ to 3 appears to have been steady, with no sharp drop at the highest redshifts, although there is now active debate in the literature about whether that trend continues or breaks at redshifts 9 and beyond (Coe et al. 2013, Ellis et al. 2013, Oesch et al. 2013). Although we have adopted a fitting function that is a double power law in $(1+z)$, we note that the SFRD data at $z < 1$ can also be fit quite well by an exponential decline with cosmic time and an e-folding timescale of 3.9 Gyr. Compared with the recent empirical fit to the SFRD by Behroozi et al. (2013), the function in Equation 15 reaches its peak at a slightly higher redshift, with a lower maximum value of ψ and with slightly shallower rates of change at both lower and higher redshift, and produces 20% fewer stars by $z = 0$.

We also note that each published measurement has its own approach to computing uncertainties on the SFRD and takes different random and systematic factors into account, and we have made no attempt to rationalize these here. Moreover, the published studies integrate their measurements down to different luminosity limits. We have instead adopted a fixed threshold of $0.03L_*$ to integrate the published LFs, and given the covariance on the measurements and uncertainties of LF parameters, there is no simple way for us to correct the published uncertainties to be appropriate for our adopted integration limit. Therefore, we have simply retained the fractional errors on the SFRD measurements published by each author without modification to provide an indication of the relative inaccuracy derived by each study. These should not be taken too literally, especially when there is significant difference in the faint-end slopes of LFs reported in different studies, which can lead to large differences in the integrated luminosity density. Uncertainties in the faint-end slope and the resulting extrapolations are not always fully taken into account in published error analyses, especially when LFs are fit at high redshift by fixing the slope to some value measured only at lower redshift.

5.2. Core-Collapse Supernova Rate

Because core-collapse supernovae (CC SNe) (i.e., Type II and Ibc SNe) originate from massive, short-lived stars, the rates of these events should reflect ongoing star formation and offer an independent determination of the cosmic star formation and metal production rates at different cosmological epochs (e.g., Madau et al. 1998a, Dahlen et al. 2004). Although poor statistics and dust obscuration are major liming factors for using CC SNe as a tracer of the SFH of the Universe, most derived rates are consistent with each other and increase with lookback time between $z = 0$ and $z \sim 1$ (see **Figure 10**). The comoving volumetric SN rate is determined by multiplying Equation 15 by the efficiency of forming CC SNe

$$R_{\rm CC}(z) = \psi(z) \times \frac{\int_{m_{\rm min}}^{m_{\rm max}} \phi(m) {\rm d}m}{\int_{m_l}^{m_u} m\phi(m) {\rm d}m} \equiv \psi(z) \times k_{\rm CC}, \qquad (16)$$

where the number of stars that explode as SNe per unit mass is $k_{\rm CC} = 0.0068\ {\rm M}_\odot^{-1}$ for a Salpeter IMF, $m_{\rm min} = 8\,{\rm M}_\odot$ and $m_{\rm max} = 40\,{\rm M}_\odot$. The predicted cosmic SN rate is shown in **Figure 10** and appears to be in good agreement with the data. The IMF dependence in Equation 16 is largely canceled out by the IMF dependence of the derived SFRD $\psi(z)$, as the stellar mass range probed by SFR indicators is comparable to the mass range of stars exploding as CC SNe. Recent comparisons between SFRs and CC SN rates have suggested a discrepancy between the two rates:

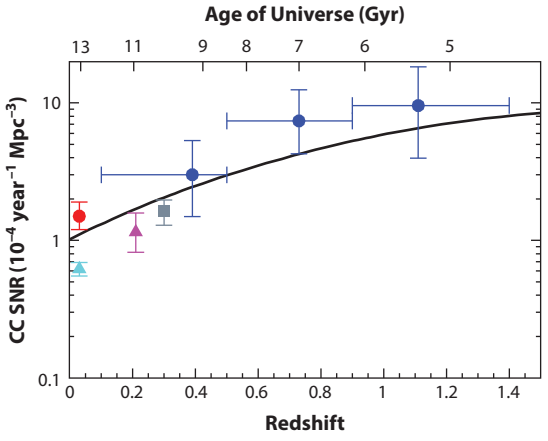

Figure 10

The cosmic core-collapse supernova rate (CC SNR). The data points are taken from Li et al. (2011) (*cyan triangle*), Mattila et al. (2012) (*red dot*), Botticella et al. (2008) (*magenta triangle*), Bazin et al. (2009) (*gray square*), and Dahlen et al. (2012) (*blue dots*). The solid line shows the rates predicted from our fit to the cosmic star-formation history. The local overdensity in star formation may boost the local rate within 10–15 Mpc of Mattila et al. (2012).

The numbers of CC SNe detected are too low by a factor of approximately 2 (Horiuchi et al. 2011). Our revised cosmic SFH does not appear to show such systematic discrepancy (see also Dahlen et al. 2012).

Observations show that at least some long-duration gamma-ray bursts (GRBs) happen simultaneously with CC SNe, but neither all SNe nor even all SNe of Type Ibc produce GRBs (for a review, see Woosley & Bloom 2006). In principle, the rate of GRBs of this class could provide a complementary estimate of the SFRD (e.g., Porciani & Madau 2001), but it is only a small fraction (<1% after correction for beaming) of the CC SN rate (Gal-Yam et al. 2006), suggesting that GRBs are an uncommon chapter in the evolution of massive stars requiring special conditions that are difficult to model. Recent studies of the GRB-SFR connection have claimed that GRBs do not trace the SFR in an unbiased way and are more frequent per unit stellar mass formed at early times (Kistler et al. 2009, Robertson & Ellis 2012, Trenti et al. 2012).

5.3. Stellar Mass Density

Figure 11 shows a compilation (see also **Table 2**) of recent (mostly post 2006) measurements of the SMD as a function of redshift (for a compilation of older data, see Wilkins et al. 2008a). We show local SDSS-based SMDs from Gallazzi et al. (2008), Li & White (2009), and Moustakas et al. (2013). Moustakas et al. (2013) also measured SMFs at $0.2 < z < 1$. However, at $z > 0.5$, their mass completeness limit is larger than $10^{9.5}$ $M_\odot$, so we have used their points only below that redshift. At higher redshifts (as in Moustakas et al. 2013), nearly all the modern estimates incorporate *Spitzer* IRAC photometry; we include only one recent analysis (Bielby et al. 2012) that does not but that otherwise uses excellent deep, wide-field NIR data in four independent sightlines. We also include measurements at $0.1 < z \lesssim 4$ from Arnouts et al. (2007), Pérez-González et al. (2008), Kajisawa et al. (2009), Marchesini et al. (2009), Pozzetti et al. (2010), Reddy & Steidel (2009), Ilbert et al. (2013), and Muzzin et al. (2013). We show measurements for the IRAC-selected sample of Caputi et al. (2011) at $3 \leq z \leq 5$ and for UV-selected LBG samples at $4 < z < 8$ by Yabe et al. (2009), González et al. (2011), Lee et al. (2012), and Labbé et al. (2013).

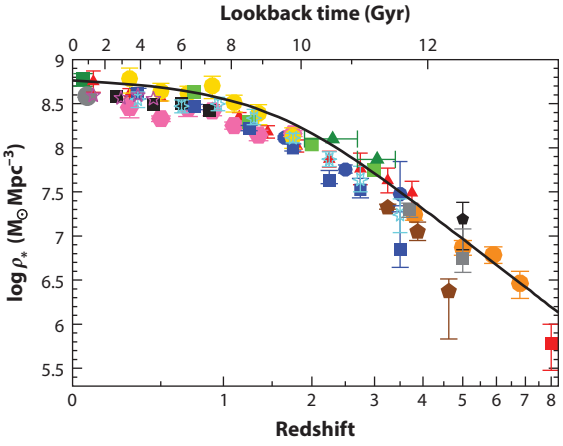

Figure 11

The evolution of the stellar mass density. The data points with symbols are given in **Table 2**. The solid line shows the global stellar mass density obtained by integrating the best-fit instantaneous star-formation rate density $\psi(z)$ (Equations 2 and 15) with a return fraction $R = 0.27$.

When needed, we have scaled from a Chabrier IMF to a Salpeter IMF by multiplying the stellar masses by a factor of 1.64 (**Figure 4**). At high redshift, authors often extrapolate their SMFs beyond the observed range by fitting a Schechter function. Stellar mass completeness at any given redshift is rarely as well defined as luminosity completeness, given the broad range of M/L values that galaxies can exhibit. Unlike the LFs used for the SFRD calculations where we have tried to impose a consistent faint luminosity limit (relative to L_*) for integration, in most cases we have simply accepted whatever low-mass limits or integral values that the various authors reported. Many authors found that the characteristic mass M_* appears to change little for $0 < z < 3$ (e.g., Fontana et al. 2006, Ilbert et al. 2013) and is roughly 10^{11} $M_\odot$ (Salpeter). Therefore, a low-mass integration limit similar to that which we used for the LFs ($L_{\rm min} = 0.03\,L_*$) would correspond to $M_{\rm min} \approx 10^{9.5}\,M_\odot$ in that redshift range. A common but by no means universal low-mass integration limit used in the literature is $10^8\,M_\odot$. Generally, SMFs have flatter low-mass slopes than do UVLFs (and sometimes IRLFs), so the lower-mass limit makes less difference to the SMDs than it does to the SFRDs.

Our model predicts an SMD that is somewhat high (~0.2 dex on average, or 60%) compared with many, but not all, of the data at $0 < z \lesssim 3$. At $0.2 < z < 2$, our model matches the SMD measurements for the *Spitzer* IRAC-selected sample of Arnouts et al. (2007), but several other modern measurements in this redshift range from COSMOS (Pozzetti et al. 2010, Ilbert et al. 2013, Muzzin et al. 2013) fall below our curve. Carried down to $z = 0$, our model is somewhat high compared with several, but not all (Gallazzi et al. 2008), local estimates of the SMD (e.g., Cole et al. 2001, Baldry et al. 2008, Li & White 2009).

Several previous analyses (Hopkins & Beacom 2006, but see the erratum; Hopkins & Beacom 2008; Wilkins et al. 2008a) have found that the instantaneous SFH overpredicts the SMD by larger factors, up to 0.6 dex at redshift 3. We find little evidence for such significant discrepancies, although there does appear to be a net offset over a broad redshift range. Although smaller, a ~60% effect should not be disregarded. One can imagine several possible causes for this discrepancy; we consider several of them here.

SFRs may be overestimated, particularly at high redshift during the peak era of galaxy growth. For UV-based measurements, a likely culprit may be the luminosity-weighted dust corrections,

Table 2 Determinations of the cosmic stellar mass density used in this review

Reference	Redshift range	$\log \rho_*$ [a] [$M_\odot$ Mpc^{-3}]	Symbols used in Figure 11
Li & White (2009)	0.07	$8.59^{+0.01}_{-0.01}$	Gray dot
Gallazzi et al. (2008)	0.005–0.22	$8.78^{+0.07}_{-0.08}$	Dark green square
Moustakas et al. (2013)	0.0–0.2	$8.59^{+0.05}_{-0.05}$	Magenta stars
	0.2–0.3	$8.56^{+0.09}_{-0.09}$	
	0.3–0.4	$8.59^{+0.06}_{-0.06}$	
	0.4–0.5	$8.55^{+0.08}_{-0.08}$	
Bielby et al. (2012)[b]	0.2–0.4	$8.46^{+0.09}_{-0.12}$	Pink filled hexagons
	0.4–0.6	$8.33^{+0.03}_{-0.03}$	
	0.6–0.8	$8.45^{+0.08}_{-0.1}$	
	0.8–1.0	$8.42^{+0.05}_{-0.06}$	
	1.0–1.2	$8.25^{+0.04}_{-0.04}$	
	1.2–1.5	$8.14^{+0.06}_{-0.06}$	
	1.5–2.0	$8.16^{+0.32}_{-0.03}$	
Pérez-González et al. (2008)	0.0–0.2	$8.75^{+0.12}_{-0.12}$	Red triangles
	0.2–0.4	$8.61^{+0.06}_{-0.06}$	
	0.4–0.6	$8.57^{+0.04}_{-0.04}$	
	0.6–0.8	$8.52^{+0.05}_{-0.05}$	
	0.8–1.0	$8.44^{+0.05}_{-0.05}$	
	1.0–1.3	$8.35^{+0.05}_{-0.05}$	
	1.3–1.6	$8.18^{+0.07}_{-0.07}$	
	1.6–2.0	$8.02^{+0.07}_{-0.07}$	
	2.0–2.5	$7.87^{+0.09}_{-0.09}$	
	2.5–3.0	$7.76^{+0.18}_{-0.18}$	
	3.0–3.5	$7.63^{+0.14}_{-0.14}$	
	3.5–4.0	$7.49^{+0.13}_{-0.13}$	
Ilbert et al. (2013)	0.2–0.5	$8.55^{+0.08}_{-0.09}$	Cyan stars
	0.5–0.8	$8.47^{+0.07}_{-0.08}$	
	0.8–1.1	$8.50^{+0.08}_{-0.08}$	
	1.1–1.5	$8.34^{+0.10}_{-0.07}$	
	1.5–2.0	$8.11^{+0.05}_{-0.06}$	
	2.0–2.5	$7.87^{+0.08}_{-0.08}$	
	2.5–3.0	$7.64^{+0.15}_{-0.14}$	
	3.0–4.0	$7.24^{+0.18}_{-0.20}$	
Muzzin et al. (2013)	0.2–0.5	$8.61^{+0.06}_{-0.06}$	Blue squares
	0.5–1.0	$8.46^{+0.03}_{-0.03}$	
	1.0–1.5	$8.22^{+0.03}_{-0.03}$	
	1.5–2.0	$7.99^{+0.05}_{-0.03}$	
	2.0–2.5	$7.63^{+0.11}_{-0.04}$	
	2.5–3.0	$7.52^{+0.13}_{-0.09}$	
	3.0–4.0	$6.84^{+0.43}_{-0.20}$	

(*Continued*)

Table 2 (*Continued*)

Reference	Redshift range	$\log \rho_*$[a] [$M_\odot$ Mpc^{-3}]	Symbols used in Figure 11
Arnouts et al. (2007)	0.3	$8.78^{+0.12}_{-0.16}$	Yellow dots
	0.5	$8.64^{+0.09}_{-0.11}$	
	0.7	$8.62^{+0.08}_{-0.10}$	
	0.9	$8.70^{+0.11}_{-0.15}$	
	1.1	$8.51^{+0.08}_{-0.11}$	
	1.35	$8.39^{+0.10}_{-0.13}$	
	1.75	$8.13^{+0.10}_{-0.13}$	
Pozzetti et al. (2010)	0.1–0.35	8.58	Black squares
	0.35–0.55	8.49	
	0.55–0.75	8.50	
	0.75–1.00	8.42	
Kajisawa et al. (2009)	0.5–1.0	8.63	Green squares
	1.0–1.5	8.30	
	1.5–2.5	8.04	
	2.5–3.5	7.74	
Marchesini et al. (2009)	1.3–2.0	$8.11^{+0.02}_{-0.02}$	Blue dots
	2.0–3.0	$7.75^{+0.05}_{-0.04}$	
	3.0–4.0	$7.47^{+0.37}_{-0.13}$	
Reddy et al. (2012)	1.9–2.7	$8.10^{+0.03}_{-0.03}$	Dark green triangles
	2.7–3.4	$7.87^{+0.03}_{-0.03}$	
Caputi et al. (2011)	3.0–3.5	$7.32^{+0.04}_{-0.02}$	Brown pentagons
	3.5–4.25	$7.05^{+0.11}_{-0.10}$	
	4.25–5.0	$6.37^{+0.14}_{-0.54}$	
González et al. (2011)[c]	3.8	$7.24^{+0.06}_{-0.06}$	Orange dots
	5.0	$6.87^{+0.08}_{-0.09}$	
	5.9	$6.79^{+0.09}_{-0.09}$	
	6.8	$6.46^{+0.14}_{-0.17}$	
Lee et al. (2012)[c]	3.7	$7.30^{+0.07}_{-0.09}$	Gray squares
	5.0	$6.75^{+0.33}_{-0.16}$	
Yabe et al. (2009)	5.0	$7.19^{+0.19}_{-0.35}$	Small black pentagon
Labbé et al. (2013)	8.0	$5.78^{+0.22}_{-0.30}$	Red square

[a]All the stellar mass densities have been derived assuming a Salpeter initial mass function.
[b]Stellar mass densities were computed by averaging over the four fields studied by Bielby et al. (2012).
[c]Following Stark et al. (2013), the mass densities of González et al. (2011) and Lee et al. (2012) at $z \simeq 4$, 5, 6, and 7 have been reduced by the factor 1.1, 1.3, 1.6, and 2.4, respectively, to account for contamination by nebular emission lines.

which could be too large, although it is often asserted that UV data are likely to underestimate SFRs in very dusty, luminous galaxies. IR-based SFRs may be overestimated and indeed were overestimated for some high-redshift galaxies in earlier *Spitzer* studies, although this seems less likely now in the era of deep *Herschel* FIR measurements. It seems more plausible that the SFRs inferred for individual galaxies may be correct on average but that the LF extrapolations could be too large. Many authors adopt fairly steep ($\alpha \geq -1.6$) faint-end slopes to both the UVLFs and IRLFs for distant galaxies. For the UVLFs, the best modern data constrain these slopes quite well,

but in the IR current measurements are not deep enough to do so. However, although these extrapolations may be uncertain, the good agreement between the current best estimates of the UV- and IR-based SFRDs at $0 < z < 2.5$ (**Figure 9**) does not clearly point to a problem in either one.

Instead, stellar masses or their integrated SMD may be systematically underestimated. This is not implausible, particularly for star-forming galaxies, where the problem of recent star formation "outshining" older high-*M/L* stars is well known (see Section 5.1). By analyzing mock catalogs of galaxies drawn from simulations with realistic (and complex) SFHs, Pforr et al. (2012) found that the simplifying assumptions that are typically made when modeling stellar masses for real surveys generally lead to systematically underestimated stellar masses at all redshifts. That said, other systematic effects can work in the opposite direction and lead to mass overestimates, e.g., the effects of TP-AGB stars on the red and NIR light if these are not correctly modeled (Maraston 2005). A steeper low-mass slope to the GSMF could also increase the total SMD. This has been suggested even at $z = 0$, where mass functions have been measured with seemingly great precision and dynamic range (e.g., Baldry et al. 2008). At high redshift, most studies to date have found relatively flat low-mass SMF slopes, but galaxy samples may be incomplete (and photometric redshift estimates poor) for very faint, red, high-*M/L* galaxies if they exist in significant numbers. Some recent SMF determinations using very deep HST WFC3 observations have found steeper SMF slopes at $z > 1.5$ (e.g., Santini et al. 2012), and new measurements from extremely deep NIR surveys such as CANDELS are eagerly anticipated. That said, it seems unlikely that the SMF slope at low redshift has been underestimated enough to account for a difference of 0.2 dex in the SMD.

Recent evidence has suggested that strong nebular line emission can significantly affect broadband photometry for galaxies at high redshift, particularly $z > 3.8$, where Hα (and, at $z > 5.3$, [OIII]) enter the *Spitzer* IRAC bands (Shim et al. 2011). Therefore, following Stark et al. (2013), we have divided the SMD of González et al. (2011) at $z \simeq 4$, 5, 6, and 7 in **Figure 11** by the factor 1.1, 1.3, 1.6, and 2.4, respectively, to account for this effect. Although considerable uncertainties in these corrections remain, such downward revision to the inferred early SMD improves consistency with expectations from the time-integrated SFRD.

Alternatively, some authors have considered how changing the IMF may help reconcile SMD(z) with the time-integrated SFRD(z) (e.g., Wilkins et al. 2008b). Generally, a more top-heavy or bottom-light IMF will lead to larger luminosities per unit SFR, hence smaller SFR/*L* conversion factors *K* (Section 3.1). Mass-to-light ratios for older stellar populations will also tend to be smaller, but not necessarily by the same factor. Although we have used a Salpeter IMF for reference in this review, an IMF with a low-mass turnover (e.g., Chabrier or Kroupa) will yield a larger mass return fraction *R* and proportionately lower final stellar masses for a given integrated past SFH by the factor $(1 - R_1)/(1 - R_2) = 0.81$, where R_1 and $R_2 = 0.41$ and 0.27 for the Chabrier and Salpeter IMFs, respectively (Section 2). The apparent offset between the SMD data and our integrated model $\psi(z)$ can be reduced further to only ~0.1 dex without invoking a particularly unusual IMF. Given the remaining potential for systemic uncertainties in the measurements of SFRDs and SMDs, it seems premature to tinker further with the IMF, although if discrepancies remain after further improvements in the measurements and modeling then this topic may be worth revisiting.

5.4. Fossil Cosmology

In concordance with estimates from the cosmic SFH, the measurements of the SMD discussed above imply that galaxies formed the bulk ($\gtrsim$75%) of their stellar mass at $z < 2$. Stars formed in galaxies before 11.5 Gyr are predicted to contribute only 8% of the total stellar mass today. An important consistency check for all these determinations could come from studies of the past

SFH of the Universe from its present contents. This "fossil cosmology" approach has benefited from large spectroscopic surveys in the local Universe such as the 2dFGRS (Colless et al. 2001) and the SDSS (York et al. 2000), which provide detailed spectral information for hundreds of thousands of galaxies. Using a sample of 1.7×10^5 galaxies drawn from the SDSS DR2 and comparing the spectrum of each galaxy to a library of templates by Bruzual & Charlot (2003) (the comparison was based on five spectral absorption features, namely D4,000, Hβ, and Hδ_A + Hγ_A as age-sensitive indexes and [Mg_2Fe] and [MgFe]$'$ as metal-sensitive indexes), Gallazzi et al. (2008) have constructed a distribution of stellar mass as a function of age (for a similar analysis on the SDSS DR3 sample, see also Panter et al. 2007). In **Figure 12**, we compare this distribution with the one predicted by our best-fit cosmic SFH. The latter implies a mass-weighted mean stellar age,

$$\langle t_{\rm age} \rangle = t_0 - \int_0^{t_0} t\psi(t){\rm d}t \left[\int_0^{t_0} \psi(t){\rm d}t \right]^{-1}, \quad (17)$$

equal to $\langle t_{\rm age} \rangle = 8.3$ Gyr. Both distributions have a peak at 8–10 Gyr and decline rapidly at younger ages, with the peak age corresponding to the formation redshift, $z \sim 2$, where the cosmic star-formation density reaches a maximum. The SDSS distribution, however, appears to be skewed toward younger ages. This is partly caused by a bias toward younger populations in the SDSS "archaeological" approach, where individual galaxies are assigned only an average (weighted by mass or light) age that is closer to the last significant episode of star formation. Such bias appears to be reflected in **Figure 12** where the mass assembly history predicted by our model SFH is compared with that inferred by translating the characteristic age of the stellar populations measured by Gallazzi et al. (2008) into a characteristic redshift of formation. The agreement is generally good, although the SDSS distribution would predict later star formation and more rapid SMD growth at $z < 2$ and correspondingly less stellar mass formed at $z > 2$. The present-day total SMD derived by Gallazzi et al. (2008) is $(6.0 \pm 1.0) \times 10^8$ $M_\odot$ Mpc^{-3} (scaled up from a Chabrier to a Salpeter IMF), in excellent agreement with $\rho_* = 5.8 \times 10^8$ $M_\odot$ Mpc^{-3} predicted by our model SFH. This stellar density corresponds to a stellar baryon fraction of only 9% (5% for a Chabrier IMF).

5.5. The Global Specific Star-Formation Rate

In recent years, there has been considerable interest in the sSFR (sSFR $\equiv$ SFR/M_*) of galaxies with different masses at different times in the history of the Universe. The sSFR describes the fractional growth rate of stellar mass in a galaxy or, equivalently, the ratio of current to past star formation. The inverse of the sSFR is the characteristic stellar mass doubling time (Guzman et al. 1997). At $0 < z < 2$ and quite possibly at higher redshifts, most star-forming galaxies follow a reasonably tight relation between SFR and M_*, whose normalization (e.g., the mean sSFR at some fiducial mass) decreases steadily with cosmic time (decreasing redshift) at least from $z = 2$ to the present (Brinchmann et al. 2004, Daddi et al. 2007, Elbaz et al. 2007, Noeske et al. 2007). A minority population of starburst galaxies exhibits elevated sSFRs, whereas quiescent or passive galaxies lie below the SFR-M_* correlation. For the "main sequence" of star-forming galaxies, most studies find that the average sSFR is a mildly declining function of stellar mass (e.g., Karim et al. 2011). This implies that more massive galaxies completed the bulk of their star formation earlier than that did lower-mass galaxies (Brinchmann & Ellis 2000, Juneau et al. 2005), a "downsizing" picture first introduced by Cowie et al. (1996). Dwarf galaxies continue to undergo major episodes of activity. The tightness of this SFR-M_* correlation has important implications for how star formation is regulated within galaxies and perhaps for the cosmic SFH. Starburst galaxies, whose SFRs are significantly elevated above the main-sequence correlation, contribute only a small fraction of the global SFRD at $z \leq 2$ (Rodighiero et al. 2011, Sargent et al. 2012).

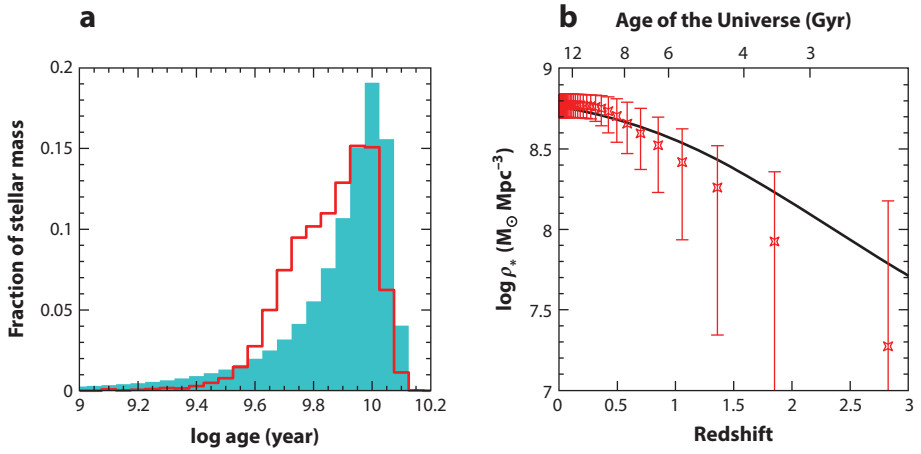

Figure 12

"Stellar archaeology" with the SDSS. (*a*) Normalized distribution of stellar mass in the local Universe as a function of age. The red histogram shows estimates from the SDSS (Gallazzi et al. 2008). The measured (mass-weighted) ages have been corrected by adding the lookback time corresponding to the redshift at which the galaxy is observed. The turquoise shaded histogram shows the distribution generated by integrating the instantaneous star-formation rate density in Equation 2. (*b*) Evolution of the stellar mass density with redshift. The points, shown with systematic error bars, are derived from the analysis of SDSS data by Gallazzi et al. (2008), assuming a Salpeter IMF in the range $0.1-100\,M_\odot$. The solid line shows the mass assembly history predicted by integrating our best-fit star-formation history. Abbreviations: IMF, initial mass function; SDSS, Sloan Digital Sky Survey.

Instead, the evolution of the cosmic SFR is primarily due to the steadily evolving properties of main-sequence disk galaxies.

Figure 13 compares the sSFR (in Gyr^{-1}) for star-forming galaxies with estimated stellar masses in the range $10^{9.4}-10^{10}\,M_\odot$ from a recent compilation by González et al. (2014) with the predictions from our best-fit SFH. At $z < 2$, the globally averaged sSFR ($\equiv \psi/\rho_*$) declines more steeply than does that for the star-forming population, as star formation is "quenched" for an increasingly large fraction of the galaxy population. These passive galaxies are represented in the global sSFR, but not in the sSFR of the star-forming "main sequence." Previous derivations showed a nearly constant sSFR of $\sim 2\ \mathrm{Gyr}^{-1}$ for galaxies in the redshift range $2 < z < 7$, suggesting relatively inefficient early star formation and exponential growth in SFRs and stellar masses with cosmic time. Recent estimates of reduced stellar masses were derived after correcting for nebular emission in broadband photometry and appear to require some evolution in the high-z sSFR (Stark et al. 2013, González et al. 2014). At these epochs, the global sSFR decreases with increasing cosmic time t as sSFR $\sim 4/t\ \mathrm{Gyr}^{-1}$, a consequence of the power-law scaling of our SFRD, $\psi(t) \propto t^{1.9}$.

5.6. Cosmic Metallicity

According to Equation 4, the sum of the heavy elements stored in stars and in the gas phase at any given time, $Z\rho_g + \langle Z_* \rangle \rho_*$, is equal to the total mass of metals produced over cosmic history, $y\rho_*$. It can be useful to express this quantity relative to the baryon density,

$$Z_b(z) \equiv \frac{y\rho_*(z)}{\rho_b}, \tag{18}$$

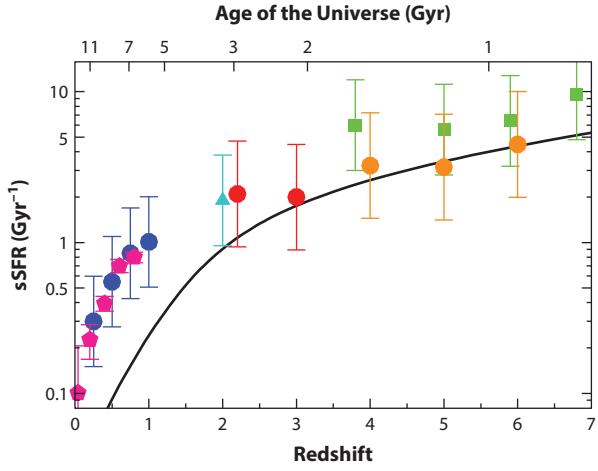

Figure 13

The mean specific star-formation rate (sSFR $\equiv$ SFR/M_*) for galaxies with estimated stellar masses in the range $10^{9.4}$–10^{10} $M_\odot$. The values are from Daddi et al. (2007) (*cyan triangle*), Noeske et al. (2007) (*blue dots*), Damen et al. (2009) (*magenta pentagons*), Reddy & Steidel (2009) (*red dots*), González et al. (2014) (*orange dots*), and Stark et al. (2013) (*green squares*). The error bars correspond to systematic uncertainties. The high-redshift points from González et al. (2014) and Stark et al. (2013) have been corrected upward owing to the effect of optical emission lines on the derived stellar masses, using the "RSF with emission lines" model of González et al. (2014) and the "fixed Hα EW" model of Stark et al. (2013). The curve shows the predictions from our best-fit star-formation history.

where $\rho_b = 2.77 \times 10^{11} \Omega_b h^2\, M_\odot\, \mathrm{Mpc}^{-3}$. The evolution of the mean metallicity of the Universe, Z_b, predicted by our model SFH is plotted in **Figure 14**. The global metallicity is $Z_b \simeq 0.09\ (y/Z_\odot)$ solar at the present epoch (note that this is the same value derived by Madau et al. 1998b). It drops to $Z_b \simeq 0.01(y/Z_\odot)$ solar at $z = 2.5$, i.e., the star-formation activity we believe to have taken place between the Big Bang and $z = 2.5$ (2.5 Gyr later) was sufficient to enrich the Universe as a whole to a metallicity of $\sim$1% solar (for $y \simeq Z_\odot$). Note that the metal production term $y\rho_*$ (and therefore Z_b) depends only weakly on the IMF (at a fixed luminosity density): Salpeter-based mass-to-light ratios are 1.64 times higher than those based on Chabrier. This is counterbalanced by Salpeter-based net metal yields that are a factor of $\sim$2 lower than those based on Chabrier (see Section 2).

Figure 14 also shows the metallicity of a variety of astrophysical objects at different epochs. The mass-weighted average stellar metallicity in the local Universe, $\langle Z_*(0)\rangle = (1.04 \pm 0.14)\, Z_\odot$ (Gallazzi et al. 2008), is plotted together with the metallicity of three different gaseous components of the distant Universe: (*a*) galaxy clusters, the largest bound objects for which chemical enrichment can be thoroughly studied and perhaps the best example in nature of a "closed box"; (*b*) the damped Lyα absorption systems that originate in galaxies and dominate the neutral-gas content of the Universe; and (*c*) the highly ionized circumgalactic and intergalactic gas that participates in the cycle of baryons in and out of galaxies in the early Universe.

The iron mass in clusters is several times larger than could have been produced by CC SNe if stars formed with a standard IMF, a discrepancy that may indicate an IMF in clusters that is skewed toward high-mass stars (e.g., Portinari et al. 2004) and/or to enhanced iron production by Type Ia SNe (e.g., Maoz & Gal-Yam 2004). The damped Lyα absorption systems are detected in absorption (i.e., have no luminosity bias), and their large optical depths at the Lyman limit eliminate the need for uncertain ionization corrections to deduce metal abundances. Their metallicity is

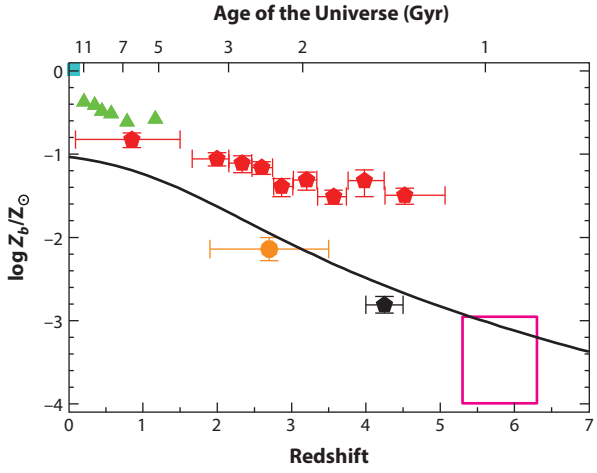

Figure 14

Mean metallicity of the Universe (in solar units): (*solid curve*) mass of heavy elements ever produced per cosmic baryon from our model SFH, for an assumed IMF-averaged yield of $y = 0.02$; (*turquoise square*) mass-weighted stellar metallicity in the nearby Universe from the SDSS (Gallazzi et al. 2008); (*green triangles*) mean iron abundances in the central regions of galaxy clusters (Balestra et al. 2007); (*red pentagons*) column density-weighted metallicities of the damped Lyα absorption systems (Rafelski et al. 2012); (*orange dot*) metallicity of the IGM as probed by OVI absorption in the Lyα forest (Aguirre et al. 2008); (*black pentagon*) metallicity of the IGM as probed by CIV absorption (Simcoe 2011); (*magenta rectangle*) metallicity of the IGM as probed by CIV and CII absorption (Ryan-Weber et al. 2009, Becker et al. 2011, Simcoe et al. 2011). Abbreviations: IGM, intergalactic medium; IMF, initial mass function; SDSS, Sloan Digital Sky Survey; SFH, star-formation history.

determined with the highest confidence from elements such as O, S, Si, Zn, and Fe and decreases with increasing redshift down to ≈1/600 solar to $z \sim 5$ (e.g., Rafelski et al. 2012). The enrichment of the circumgalactic medium, as probed in absorption by CIII, CIV, SiIII, SiIV, OVI, and other transitions, provides us with a record of past star formation and of the impact of galactic winds on their surroundings. **Figure 14** shows that the ionization-corrected metal abundances from OVI absorption at $z \sim 3$ (Aguirre et al. 2008) and CIV absorption at $z \sim 4$ (Simcoe 2011) track well the predicted mean metallicity of the Universe, i.e., that these systems are an unbiased probe of the cosmic baryon cycle.

The Universe at redshift 6 remains one of the most challenging observational frontiers, as the high opacity of the Lyα forest inhibits detailed studies of hydrogen absorption along the line-of-sight to distant quasars. In this regime, the metal lines that fall longwards of the Lyα emission take on a special significance as the only tool at our disposal to recognize individual absorption systems, whether in galaxies or the IGM, and probe cosmic enrichment following the earliest episodes of star formation. Here, we use recent surveys of high- and low-ionization intergalactic absorption to estimate the metallicity of the Universe at these extreme redshifts. According to Simcoe et al. (2011) (see also Ryan-Weber et al. 2009), the comoving mass density of triply ionized carbon over the redshift range 5.3–6.4 is (expressed as a fraction of the critical density) $\Omega_{\rm CIV} = (0.46 \pm 0.20) \times 10^{-8}$. Over a similar redshift range, CII absorption yields $\Omega_{\rm CII} = 0.9 \times 10^{-8}$ (Becker et al. 2011). The total carbon metallicity by mass, $Z_{\rm C}$, at $\langle z \rangle = 5.8$ implied by these measurements is

$$Z_{\rm C} = \frac{\Omega_{\rm CIV} + \Omega_{\rm CII}}{\Omega_b} \times \frac{\rm C}{\rm C_{II} + C_{IV}} \simeq 3 \times 10^{-7} \frac{\rm C}{\rm C_{II} + C_{IV}}, \qquad (19)$$

where (CII + CIV)/C is the fraction of carbon that is either singly or triply ionized. In **Figure 14**, we plot Z_C in units of the mass fraction of carbon in the Sun, $Z_{C\odot} = 0.003$ (Asplund et al. 2009). The lower bound to the rectangle centered at redshift 5.8 assumes no ionization correction, i.e., (CII + CIV)/C = 1. To derive the upper bound, we adopt the conservative limit (CII + CIV)/C $\geq$ 0.1; this is the minimum fractional abundance reached by CII + CIV under the most favorable photoionization balance conditions at redshift 6. [To obtain this estimate, we have computed photoionization models based on the CLOUDY code (Ferland et al. 1998) assuming the UV radiation background at $z = 6$ of Haardt & Madau (2012) and a range of gas overdensities $0 < \log\delta < 3$.] If the ionization state of the early metal-bearing IGM is such that most of the C is either singly or triply ionized, then most of the heavy elements at these epochs appear to be "missing" compared with the expectations based on the integral of the cosmic SFH (Pettini 2006, Ryan-Weber et al. 2009). Conversely, if CII and CIV are only trace ion stages of carbon, then the majority of the heavy elements produced by stars 1 Gyr after the Big Bang ($z = 6$) may have been detected already.

A simple argument can also be made against the possibility that our best-fit SFH significantly overpredicts the cosmic metallicity at these early epochs. The massive stars that explode as Type II SNe and seed the IGM with metals are also the sources of nearly all of the Lyman-continuum (LyC) photons produced by a burst of star formation. It is then relatively straightforward to link a given IGM metallicity to the minimum number of LyC photons that must have been produced up until that time. The close correspondence between the sources of metals and photons makes the conversion from one to the other largely independent of the details of the stellar IMF (Madau & Shull 1996). Specifically, the energy emitted in hydrogen ionizing radiation per baryon, $E_{\rm ion}$, is related to the average cosmic metallicity by

$$E_{\rm ion} = \eta m_p c^2 Z_b, \qquad 20.$$

where $m_p c^2 = 938$ MeV is the rest mass of the proton and η is the efficiency of conversion of the heavy element rest mass into LyC radiation. For stars with $Z_* = Z_\odot/50$, one derives $\eta = 0.014$ (Schaerer 2002, Venkatesan & Truran 2003). An average energy of 22 eV per LyC photon together with our prediction of $Z_b = 7 \times 10^{-4} Z_\odot$ (assuming a solar yield) at redshift 6 implies that approximately 8 LyC photons per baryon were emitted by early galaxies prior to this epoch. Although at least one photon per baryon is needed for reionization to occur, this is a reasonable value because the effect of hydrogen recombinations in the IGM and within individual halos will likely boost the number of photons required. A global metallicity at $z = 6$ that was much lower than our predicted value would effectively create a deficit of UV radiation and leave the reionization of the IGM unexplained. In Section 5.8 below, we link the production of LyC photons to stellar mass, show that the efficiency of LyC production decreases with increasing Z_*, and discuss early star formation and the epoch of reionization in more detail.

5.7. Black Hole Accretion History

Direct dynamical measurements show that most local massive galaxies host a quiescent massive black hole in their nuclei. Their masses correlate tightly with the stellar velocity dispersion of the host stellar bulge, as manifested in the $M_{\rm BH} - \sigma_*$ relation of spheroids (Ferrarese & Merritt 2000, Gebhardt et al. 2000). It is not yet understood whether such scaling relations were set in primordial structures and maintained throughout cosmic time with a small dispersion or which physical processes established such correlations in the first place. Nor it is understood whether the energy released during the luminous quasar phase has a global impact on the host, generating

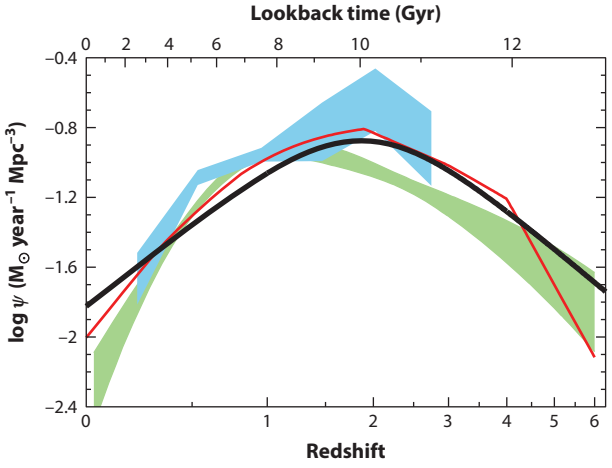

Figure 15

Comparison of the best-fit star-formation history (*thick solid curve*) with the massive black hole accretion history from X-ray [*red curve* (Shankar et al. 2009); *light green shading* (Aird et al. 2010)] and infrared (*light blue shading*) (Delvecchio et al. 2014) data. The shading indicates the $\pm 1\sigma$ uncertainty range on the total bolometric luminosity density. The radiative efficiency has been set to $\epsilon = 0.1$. The comoving rates of black hole accretion have been scaled up by a factor of 3,300 to facilitate visual comparison to the star-formation history.

large-scale galactic outflows and quenching star formation (Di Matteo et al. 2005), or just modifies gas dynamics in the galactic nucleus (Debuhr et al. 2010).

Here, we consider a different perspective on the link between the assembly of the stellar component of galaxies and the growth of their central black holes. The cosmic mass accretion history of massive black holes can be inferred using Soltan's argument (Soltan 1982), which relates the quasar bolometric luminosity density to the rate at which mass accumulates into black holes,

$$\dot{\rho}_{\rm BH}(z) = \frac{1-\epsilon}{\epsilon c^2} \int L\phi(L, z) {\rm d}L, \qquad (21)$$

where ϵ is the efficiency of conversion of rest-mass energy into radiation. In practice, bolometric luminosities are typically derived from observations of the AGN emission at X-ray, optical or IR wavelengths, scaled by a bolometric correction. In **Figure 15**, several recent determinations of the massive black hole mass growth rate are compared with the cosmic SFRD (Equation 15). Also shown is the accretion history derived from the hard X-ray LF of Aird et al. (2010), assuming a radiative efficiency $\epsilon = 0.1$ and a constant bolometric correction of 40 for the observed 2–10 KeV X-ray luminosities. This accretion rate peaks at lower redshift than does the SFRD and declines more rapidly from $z \approx 1$ to 0. However, several authors have discussed the need for luminosity-dependent bolometric corrections, which in turn can affect the derived accretion history (e.g., Marconi et al. 2004, Hopkins et al. 2007, Shankar et al. 2009). Moreover, although the hard X-ray LF includes unobscured as well as moderately obscured sources that may not be identified as AGN at optical wavelengths, it can miss Compton thick AGN, which may be identified in other ways, particularly using IR data. Delvecchio et al. (2014) have used deep *Herschel* and *Spitzer* survey data in GOODS-S and COSMOS to identify AGN by SED fitting. This is a potentially powerful method but depends on reliable decomposition of the IR emission from AGN and star formation.

Black hole mass growth rates derived from the bolometric AGN LFs of Shankar et al. (2009) and Delvecchio et al. (2014) are also shown in **Figure 15**. These more closely track the cosmic

SFH, peaking at $z \approx 2$, and suggest that star formation and black hole growth are closely linked at all redshifts (Boyle & Terlevich 1998, Silverman et al. 2008). However, the differences between accretion histories published in the recent literature would caution that it is premature to consider this comparison to be definitive.

5.8. First Light and Cosmic Reionization

Fundamental to our understanding of how the Universe evolved to its present state is the epoch of "first light," the first billion years after the Big Bang when the collapse of the earliest baryonic objects—the elementary building blocks for the more massive systems that formed later—determined the "initial conditions" of the cosmological structure formation process. The reionization in the all-pervading IGM—the transformation of neutral hydrogen into an ionized state—is a landmark event in the history of the early Universe. Studies of Lyα absorption in the spectra of distant quasars show that the IGM is highly photoionized out to redshift $z \gtrsim 6$ (for a review, see Fan et al. 2006), whereas polarization data from the *Wilkinson Microwave Anisotropy Probe* constrain the redshift of any sudden reionization event to be significantly higher, $z = 10.5 \pm 1.2$ (Jarosik et al. 2011). It is generally thought that the IGM is kept ionized by the integrated UV emission from AGN and star-forming galaxies, but the relative contributions of these sources as a function of epoch are poorly known (e.g., Madau et al. 1999, Faucher-Giguère et al. 2008, Haardt & Madau 2012, Robertson et al. 2013).

Establishing whether massive stars in young star-forming galaxies were responsible for cosmic reionization requires a determination of the early history of star formation, of the LyC flux emitted by a stellar population, and of the fraction of hydrogen-ionizing photons that can escape from the dense sites of star formation into the low-density IGM. We can use stellar population synthesis to estimate the comoving volumetric rate at which photons above 1 Ryd are emitted from star-forming galaxies as

$$\dot{n}_{\rm ion} = I_{\rm ion} \times \psi(t), \tag{22}$$

where $\dot{n}_{\rm ion}$ is expressed in units of $\mathrm{s^{-1}\ Mpc^{-3}}$ and ψ in units of $\mathrm{M_\odot\ year^{-1}\ Mpc^{-3}}$. The LyC photon yield $I_{\rm ion}$ is plotted in **Figure 16** for our reference Salpeter IMF and for a wide range of metallicities spanning from extremely metal-poor to metal-rich stars (Schaerer 2003). The yield increases with decreasing metallicity by more than a factor of 3. Integrating Equation 22 over time and dividing by the mean comoving hydrogen density $\langle n_{\rm H} \rangle = 1.9 \times 10^{-7}\ \mathrm{cm^{-3}}$, we can write the total number of stellar LyC photons emitted per hydrogen atom since the Big Bang as

$$\mathcal{N}_{\rm ion}(z) \equiv \frac{n_{\rm ion}}{\langle n_{\rm H} \rangle} = I_{\rm ion} \times 7.8 \times 10^{-60} \times \rho_*(z), \tag{23}$$

where $\rho_*(z)$ is the cosmic SMD. [Within purely stellar radiation or energetic X-ray photons, either the total number of ionizing photons produced or the total radiated energy, respectively, is what matters for reionization. This is because, in a largely neutral medium, each photoionization produces a host of secondary collisional ionizations, with approximately one hydrogen secondary ionization for every 37 eV of energy in the primary photoelectron (Shull & van Steenberg 1985). As the medium becomes more ionized, however, an increasing fraction of this energy is deposited as heat.] **Figure 16** depicts the quantity $\mathcal{N}_{\rm ion}$ at $z > 6$ according to our best-fit SFH for the range of stellar metallicities $0 < Z_* < Z_\odot$. Cosmological reionization requires at least one LyC photon per hydrogen atom escaping into the intergalactic space, i.e., $\mathcal{N}_{\rm ion} \langle f_{\rm esc} \rangle > 1$. The exact number depends on the rate of radiative recombinations in a clumpy IGM. Here, the escape fraction $\langle f_{\rm esc} \rangle$ is the angle-averaged, absorption cross-section-weighted, and luminosity-weighted

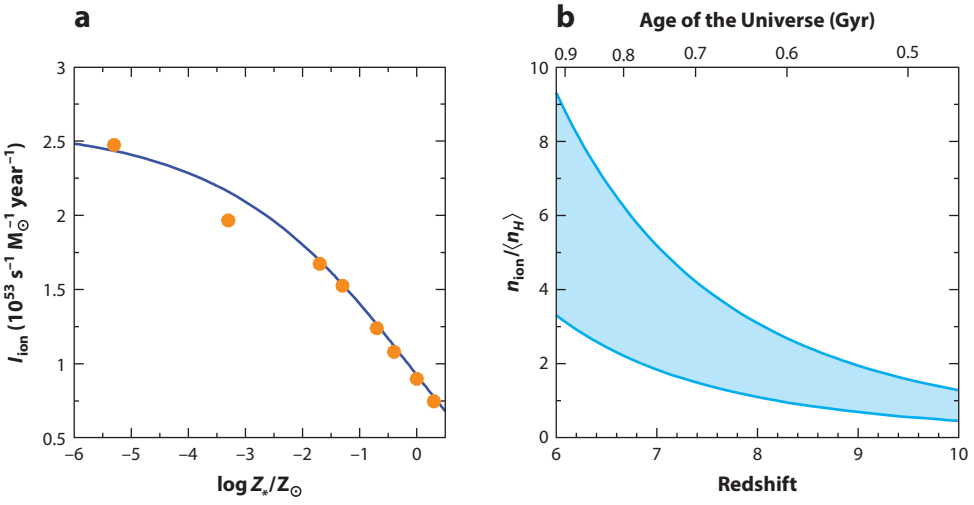

Figure 16

(*a*) Metallicity dependence of the ionizing photon yield, $I_{\rm ion}$, for a stellar population with a Salpeter IMF (initial mass function) and constant star-formation rate. The points show the values given in table 4 of Schaerer (2003), computed for a Salpeter IMF in the $1-100\,M_\odot$ range, and divided by a mass conversion factor of 2.55 to rescale to a mass range $0.1-100\,M_\odot$. The solid curve shows the best-fitting function, $\log I_{\rm ion} = [(0.00038 Z_*^{0.227} + 0.01858)]^{-1} - \log(2.55)$. (*b*) Number of H-ionizing photons emitted per hydrogen atom since the Big Bang, $n_{\rm ion}/\langle n_{\rm H}\rangle$, according to our best-fit star-formation history. The shaded area is delimited by stellar populations with metallicities $Z_* = Z_\odot$ (lower boundary) and $Z_* = 0$ (upper boundary).

fraction of ionizing photons that leaks into the IGM from the dense star-forming regions within galaxies.

Figure 16 shows the well-known result that, even if the emission of LyC photons at early cosmic times was dominated by extremely low-metallicity stars, escape fractions in excess of 20% would be required to reionize the Universe by redshift 6–7 (e.g., Bolton & Haehnelt 2007, Ouchi et al. 2009, Bunker et al. 2010, Finkelstein et al. 2012b, Haardt & Madau 2012). Although the mechanisms regulating the escape fraction of ionizing radiation from galaxies and its dependence on cosmic time and luminosity are unknown, these leakage values are higher than typically inferred from observations of LBGs at $z \sim 3$ (e.g., Nestor et al. 2013, Vanzella et al. 2012, and references therein).

The "reionization budget" is made even tighter by two facts. First, the volume-averaged hydrogen recombination timescale in the IGM,

$$\langle t_{\rm rec}\rangle = (\chi\,\langle n_{\rm H}\rangle \alpha_B\, C_{\rm IGM})^{-1} \simeq 3.2\ {\rm Gyr}\left(\frac{1+z}{7}\right)^{-3} C_{\rm IGM}^{-1}, \qquad (24)$$

is ~60% of the expansion timescale $H^{-1} = H_0^{-1}[\Omega_M(1+z)^3+\Omega_\Lambda]^{-1/2}$ at $z = 10$, i.e., close to two ionizing photons per baryon are needed to keep the IGM ionized. Here, α_B is the recombination coefficient to the excited states of hydrogen, $\chi = 1.08$ accounts for the presence of photoelectrons from singly ionized helium, and $C_{\rm IGM}$ is the clumping factor of ionized hydrogen. The above estimate assumes a gas temperature of 2×10^4 K and a clumping factor for the IGM, $C_{\rm IGM} = 1 + 43\,z^{-1.71}$, that is equal to the clumpiness of gas below a threshold overdensity of 100 found

at $z \geq 6$ in a suite of cosmological hydrodynamical simulations (Pawlik et al. 2009; see also Shull et al. 2012). Second, the rest-frame UV continuum properties of very high redshift galaxies appear to show little evidence for the "exotic" stellar populations (e.g., extremely subsolar metallicities or top-heavy IMFs) that would significantly boost the LyC photon yield (e.g., Finkelstein et al. 2012a, Dunlop et al. 2013). Although improved knowledge of the SFRD beyond redshift 9 may help to better characterize this photon shortfall, the prospects of a direct observational determination of the escape fraction of ionizing photons leaking into the IGM at these early epochs look rather bleak, as the Universe becomes opaque to LyC radiation above redshift 4.

6. CONCLUDING REMARKS

The cosmic history of star formation is one of the most fundamental observables in astrophysical cosmology. We have reviewed the range of complementary techniques and theoretical tools that are allowing astronomers to map the transformation of gas into stars, the production of heavy elements, and the reionization of the Universe from the cosmic dark ages to the present epoch. Under the simple assumption of a universal IMF, there is reasonable agreement between the global SMD inferred at any particular time and the time integral of all the preceding instantaneous star-formation activity, although modest offsets may still point toward systematic uncertainties. A consistent picture is emerging, whereby the SFRD peaked ~3.5 Gyr after the Big Bang and dropped exponentially at $z < 1$ with an e-folding timescale of 3.9 Gyr. The Universe was a much more active place in the past: Stars formed at a peak rate approximately nine times higher than is seen today. Approximately 25% of the present-day SMD formed at $z > 2$, before the peak of the SFRD, and another 25% formed since $z = 0.7$, i.e., roughly over the last half of the Universe's age. From the peak of the SFRD at $z \approx 2$ to the present day, and perhaps earlier as well, most stars formed in galaxies that obey a relatively tight SFR-M_* correlation, and only a small fraction formed in starbursts with significantly elevated specific SFRs. The smooth evolution of this dominant main-sequence galaxy population suggests that the evolution of the cosmic SFH is primarily determined by a balance between gas accretion and feedback processes, both closely related to galaxy mass, and that stochastic events such as merger-driven starbursts play a relatively minor role. The growth histories of the stellar component of galaxies and their central black holes are similar in shape, suggesting broad coevolution of black holes and their host galaxies. The rise of the mean metallicity of the Universe to 0.001 solar by redshift six, 1 Gyr after the Big Bang, appears to have been accompanied by the production of fewer than 10 hydrogen LyC photons per baryon, indicating a rather tight budget for cosmological reionization. The SFRD at $z \approx 7$ was approximately the same as that of today, at $z \approx 0$, but only 1% of today's SMD was formed during the epoch of reionization.

As far as the observations and data are concerned, there is still room for improvement in both SFRD and SMD measurements at virtually every redshift, from the local Universe to the epoch of reionization (Section 4.6). That said, it would be somewhat surprising if new measurements changed the picture dramatically at $z < 1$; it is more likely that stellar population modeling, e.g., for deriving stellar masses or SFRs, could still change the details of the picture during the decline and fall of the cosmic SFH. Indeed, at all redshifts, limitations of our methods for interpreting light as mass may play a significant, even dominant, role in the error budget for the analyses described in this review. The peak era of cosmic star formation has been extensively mapped, and yet even with the current data (**Figure 9**), it is still hard to accurately pinpoint the redshift of maximum SFRD within a range $\Delta z = 1$. Our fitting function (Equation 15) places this peak at $z \approx 1.85$, which is plausible but still uncertain. Uncertainties in the faint-end slope of the IRLF and in extinction corrections for the UVLF still dominate at this peak era of cosmic star formation.

Although evidence seems to point clearly to a steady increase in the SFRD from $z = 8$ to $z \approx 2$, our direct knowledge of dust-obscured star formation at these redshifts is, for the most part, limited to the rarest and most ultraluminous galaxies, leaving considerable uncertainty about how much SFRD we may be missing in the UV census of that early phase of galaxy evolution. At $z > 4$, our galaxy surveys have been strongly biased toward UV-bright galaxies and may underestimate both SFRDs and SMDs. Even for UV-selected galaxies, the measurements at $z \geq 8$ are very new and likely uncertain, unsupported by spectroscopic confirmation to date. In addition to measuring redshifts, spectroscopy from the JWST will help clarify basic issues about nebular line emission and the degree to which it has affected the photometric analyses that have been carried out to date.

Painstaking though all this vast effort has been, it does miss a crucial point. It says little about the inner workings of galaxies, i.e., their "metabolism" and the basic process of ingestion (gas infall and cooling), digestion (star formation), and excretion (outflows). Ultimately, it also says little about the mapping from dark matter halos to their baryonic components. Its roots are in optical-IR astronomy, statistics, stellar populations, and phenomenology, rather than in the physics of the ISM, self-regulated accretion and star formation, stellar feedback, and SN-driven galactic winds. It provides a benchmark against which to compare semianalytic modeling and hydrodynamical simulations of galaxy formation, but it offers little guidance in identifying the smaller-scale basic mechanisms that determine the rate of conversion of gas into stars and lead to the grandiose events in the history of the Universe described in this review.

A variety of physical processes are thought to shape the observed distribution of galaxy properties, ranging from those responsible for galaxy growth (e.g., star formation and galaxy merging) to those that regulate such growth (e.g., energetic feedback from SNe, AGN, and the UV radiation background). However, many of these processes likely depend primarily on the mass of a galaxy's dark matter halo. Relating the stellar masses and SFRs of galaxies to the masses and assembly histories of their parent halos is a crucial piece of the galaxy formation and evolution puzzle. With the accumulation of data from large surveys and from cosmological numerical simulations, several statistical methods have been developed over the past decade to link the properties of galaxies to the underlying dark matter structures (e.g., Berlind & Weinberg 2002, Yang et al. 2003, Vale & Ostriker 2004). One of them, the "abundance matching" technique, assumes in its simplest form a unique and monotonic relation between galaxy light and halo mass, and it reproduces galaxy clustering as a function of luminosity over a wide range in redshift (e.g., Conroy et al. 2006, Guo et al. 2010, Moster et al. 2010). Modern versions of this approach (Behroozi et al. 2013, Moster et al. 2013) have shown that (*a*) halos of mass $\sim 10^{12}\,M_\odot$ are the most efficient at forming stars at every epoch, with baryon conversion efficiencies of 20–40% that fall rapidly at both higher and lower masses; (*b*) in halos similar to that of the Milky Way, approximately half of the central stellar mass is assembled after redshift 0.7; and (*c*) in low-mass halos, the accretion of satellites contributes little to the assembly of their central galaxies, whereas in massive halos more than half of the central stellar mass is formed "ex situ." These studies represent promising advances, albeit with serious potential shortcomings (e.g., Guo & White 2013, Zentner et al. 2013). The assumption of a monotonic relation between stellar mass and the mass of the host halo is likely incorrect in detail, and it predicts only numerically converged properties on scales that are well resolved in simulations. The matching procedure requires minimal assumptions and avoids an explicit treatment of the physics of galaxy formation. As such, it provides relatively little new insight into this physics. In the version of this technique by Behroozi et al. (2013), for example, the cosmic SFH is reproduced by construction.

As of this writing, a solid interpretation of the cosmic SFH from first principles is still missing (for a recent review, see Mac Low 2013). Generically, one expects that star formation may be limited at early times by the build-up of dark matter halos and quenched at low redshift as densities

decline from Hubble expansion to the point where gas cooling is inhibited. These two regimes could then lead to a peak in the SFH at intermediate redshifts (Hernquist & Springel 2003). A decade ago, hydrodynamical simulations predicted that the peak in star-formation activity should occur at a much higher redshift, $z \gtrsim 5$, than is actually observed (Springel & Hernquist 2003, Nagamine et al. 2004). Theoretical modeling has been unable to correctly forecast the evolution of the SFRD because of the large range of galaxy masses that contribute significantly to cosmic star formation and the difficulty in following the feedback of energy into the ISM and circumgalactic medium from stellar radiation, SN explosions, and accreting massive black holes. Gas cooling in an expanding Universe is an intrinsically unstable process because cooling acts to increase the density of the gas, which in turn increases the cooling rate. Systems collapsing at low redshift have low mean densities and long cooling times, whereas systems collapsing at higher redshifts have higher mean densities and cool catastrophically. Without feedback processes that transfer energy to the ISM and reheat it, one is faced with the classical overcooling problem—the unphysical cooling of hot gas in the poorly resolved inner regions of galaxies—and with the consequent overproduction of stars at early times. And yet, a completely satisfactory treatment of feedback in hydrodynamical simulations that capture large cosmological volumes remains elusive, as these mechanisms operate on scales too small to be resolved and must therefore be incorporated via ad hoc recipes that are too simplistic to capture the complex subgrid physics involved (e.g., Schaye et al. 2009).

In-depth knowledge of the mechanisms responsible for suppressing star formation in small halos (e.g., Governato et al. 2010, Krumholz & Dekel 2012, Kuhlen et al. 2012), more powerful supercomputers, better algorithms, as well as more robust numerical implementations of stellar feedback (e.g., Agertz et al. 2013) all now appear as crucial prerequisites for predicting more realistic SFHs. Newer and deeper observations from the ground and space should improve our measurements of the galaxy population and its integrated properties, especially at and beyond the current redshift frontier where data remain sparse. It seems likely, however, that the most important contribution of new surveys and better modeling will be toward a detailed understanding of the physics of galaxy evolution, not simply its demographics.

DISCLOSURE STATEMENT

The authors are not aware of any affiliations, memberships, funding, or financial holdings that might be perceived as affecting the objectivity of this review.

ACKNOWLEDGMENTS

This review has benefited from many discussions with and the help of J. Aird, R. Chary, C. Conroy, O. Cucciati, D. Elbaz, S. Faber, H. Ferguson, A. Gallazzi, V. González, A. Klypin, K.-S. Lee, D. Maoz, P. Oesch, M. Pettini, J. Pforr, L. Pozzetti, J. Primack, J.X. Prochaska, M. Rafelski, A. Renzini, B. Robertson, M. Schenker, and D. Stark. Support for this work was provided by the National Science Foundation (NSF) through grant OIA-1124453, by NASA through grant NNX12AF87G (P.M.), and by NOAO, which is operated by the Association of Universities for Research in Astronomy, under a cooperative agreement with the NSF (M.D.).

LITERATURE CITED

Agertz O, Kravtsov AV, Leitner SN, Gnedin NY. 2013. *Ap. J.* 770:25
Aguirre A, Dow-Hygelund C, Schaye J, Theuns T. 2008. *Ap. J.* 689:851

Aird J, Nandra K, Laird ES, et al. 2010. *MNRAS* 401:2531
Alavi A, Siana B, Richard J, et al. 2013. *Ap. J.* 780:143
Appleton PN, Fadda DT, Marleau FR, et al. 2004. *Ap. J. Suppl.* 154:147
Arnouts S, Schiminovich D, Ilbert O, et al. 2005. *Ap. J. Lett.* 619:L43
Arnouts S, Walcher CJ, Le Fevre O, et al. 2007. *Astron. Astrophys.* 476:137
Ashby MLN, Willner SP, Fazio GG, et al. 2013. *Ap. J.* 679:80
Asplund M, Grevesse N, Sauval AJ, Scott P. 2009. *Annu. Rev. Astron. Astrophys.* 47:481
Atek H, Malkan M, McCarthy P. 2010. *Ap. J.* 723:104
Aussel H, Cesarsky CJ, Elbaz D, Stark JL. 1999. *Astron. Astrophys.* 342:313
Babbedge TSR, Rowan-Robinson M, Vaccari M, et al. 2006. *MNRAS* 370:1159
Baldry IK, Driver SP, Loveday J, et al. 2012. *MNRAS* 421:621
Baldry IK, Glazebrook K. 2003. *Ap. J.* 593:258
Baldry IK, Glazebrook K, Driver SP. 2008. *MNRAS* 388:945
Balestra I, Tozzi P, Ettori S, et al. 2007. *Astron. Astrophys.* 462:429
Barger A, Cowie LL, Richards EA. 2000. *Astron. J.* 119:2092
Barger A, Cowie LL, Sanders DB, et al. 1998. *Nature* 394:248
Barger A, Wang W-H, Cowie LL, et al. 2012. *Ap. J.* 761:89
Bastian N, Covey KR, Meyer MR. 2010. *Annu. Rev. Astron. Astrophys.* 48:339
Basu-Zych AR, Lehmer BD, Hornschemeier AE, et al. 2013. *Ap. J.* 762:45
Bazin G, Palanque-Delabrouille N, Rich J, et al. 2009. *Astron. Astrophys.* 499:653
Becker GD, Sargent WLW, Rauch M, Calverley AP. 2011. *Ap. J.* 735:93
Beckwith SVW, Stiavelli M, Koekemoer AM, et al. 2006. *Astron. J.* 132:1729
Behroozi PS, Wechsler RH, Conroy C. 2013. *Ap. J.* 770:57
Bell EF, MacIntosh DH, Katz N, Weinberg MD. 2003. *Ap. J. Suppl.* 149:289
Berlind AA, Weinberg DH. 2002. *Ap. J.* 575:587
Berta S, Magnelli B, Nordon R, et al. 2011. *Astron. Astrophys.* 532:A49
Béthermin M, Le Floc'h E, Olbert O, et al. 2012. *Astron. Astrophys.* 542:A57
Bielby R, Hudelot P, McCracken HJ, et al. 2012. *Astron. Astrophys.* 545:23
Blumenthal GR, Faber SM, Primack JR, Rees MJ. 1984. *Nature* 311:517
Bolton JS, Haehnelt MG. 2007. *MNRAS* 382:325
Botticella MT, Riello M, Cappellaro E, et al. 2008. *Astron. Astrophys.* 479:49
Bouwens RJ, Illingworth GD, Franx M, Ford H. 2007. *Ap. J.* 670:928
Bouwens RJ, Illingworth GD, Labbé I, et al. 2011a. *Nature* 469:504
Bouwens RJ, Illingworth GD, Oesch PA, et al. 2011b. *Ap. J.* 737:90
Bouwens RJ, Illingworth GD, Oesch PA, et al. 2012a. *Ap. J.* 754:83
Bouwens RJ, Illingworth GD, Oesch PA, et al. 2012b. *Ap. J. Lett.* 752:L5
Bowler RAA, Dunlop JS, McLure RJ, et al. 2012. *MNRAS* 426:2772
Boyle BJ, Terlevich RJ. 1998. *MNRAS* 293:L49
Brammer GB, van Dokkum PG, Franx M, et al. 2012. *Ap. J. Suppl.* 200:13
Brammer GB, Whitaker KE, van Dokkum PG, et al. 2011. *Ap. J.* 739:24
Brandt WN, Hasinger G. 2005. *Annu. Rev. Astron. Astrophys.* 43:827
Brinchmann J, Charlot S, White SDM, et al. 2004. *MNRAS* 351:1151
Brinchmann J, Ellis RS. 2000. *Ap. J. Lett.* 536:L77
Bruzual G, Charlot S. 2003. *MNRAS* 344:1000
Bruzual G, Charlot S, González López-zira R, et al. 2013. *Proc. Int. Astron. Union* 295:435
Buat V, Iglesias-Páramo J, Seibert M, et al. 2005. *Ap. J. Lett.* 619:L51
Buat V, Noll S, Burgarella D, et al. 2012. *Astron. Astrophys.* 545:A141
Budavári T, Szalay AS, Charlot S, et al. 2005. *Ap. J. Lett.* 619:L31
Bunker AJ, Wilkins S, Ellis RS, et al. 2010. *MNRAS* 409:855
Burgarella D, Buat V, Gruppioni C, et al. 2013. *Astron. Astrophys.* 554:A70
Calzetti D. 2001. *Publ. Astron. Soc. Pac.* 113:1449
Calzetti D, Armus L, Bohlin RC, et al. 2000. *Ap. J.* 533:682
Calzetti D, Kennicutt RC, Engelbracht CW, et al. 2007. *Ap. J.* 666:870

Calzetti D, Kinney AL, Storchi-Bergmann T. 1994. *Ap. J.* 429:582
Caputi KI, Cirasuolo M, Dunlop JS, et al. 2011. *MNRAS* 413:162
Caputi KI, Dunlop JS, McLure RJ, et al. 2012. *Ap. J.* 750:20
Caputi KI, Lagache G, Yan L, et al. 2007. *Ap. J.* 660:97
Carilli CL, Lee N, Capak P, et al. 2008. *Ap. J.* 689:883
Castellano M, Fontana A, Boutsia K, et al. 2010a. *Astron. Astrophys.* 511:A20
Castellano M, Fontana A, Paris D, et al. 2010b. *Astron. Astrophys.* 524:A28
Chabrier G. 2003. *Publ. Astron. Soc. Pac.* 115:763
Chapman SC, Blain AW, Smail I, Ivison RJ. 2005. *Ap. J.* 622:772
Charlot S, Fall SM. 2000. *Ap. J.* 539:718
Chary R-R, Elbaz D. 2001. *Ap. J.* 556:562
Chary R-R, Stern D, Eisenhardt P. 2005. *Ap. J. Lett.* 635:L5
Chieffi A, Limongi M. 2004. *Ap. J.* 608:405
Coe D, Zitrin A, Carrasco M, et al. 2013. *Ap. J.* 762:32
Cohen JG. 2002. *Ap. J.* 567:672
Cole S, Lacey CG, Baugh CM, Frenk CS. 2000. *MNRAS* 319:168
Cole S, Nordberg P, Baugh CM, et al. 2001. *MNRAS* 326:255
Colless M, Dalton G, Maddox S, et al. 2001. *MNRAS* 328:1039
Condon JJ. 1992. *Annu. Rev. Astron. Astrophys.* 30:575
Condon JJ, Cotton WD, Broderick JJ. 2002. *Astron. J.* 124:675
Connolly AJ, Szalay AS, Dickinson M, Subbarao MU, Brunner RJ. 1997. *Ap. J. Lett.* 486:L11
Conroy C. 2013. *Annu. Rev. Astron. Astrophys.* 51:393
Conroy C, Gunn JE, White M. 2009. *Ap. J.* 699:486
Conroy C, van Dokkum PG. 2012. *Ap. J.* 760:71
Conroy C, Wechsler RH, Kravtson AV. 2006. *Ap. J.* 647:201
Conselice CJ, Bluck AF, Buitrago F, et al. 2011. *MNRAS* 413:80
Cowie LL, Songaila A, Barger AJ. 1999. *Astron. J.* 118:603
Cowie LL, Songaila A, Hu EM, Cohen JG. 1996. *Astron. J.* 112:839
Cucciati O, Tresse L, Ilbert O, et al. 2012. *Astron. Astrophys.* 539:31
Curtis-Lake E, McLure RJ, Dunlop JS, et al. 2013. *MNRAS* 429:302
Daddi E, Cimatti A, Renzini A, et al. 2004. *Ap. J.* 617:746
Daddi E, Dannerbauer H, Krips M, et al. 2009. *Ap. J. Lett.* 695:L176
Daddi E, Dickinson M, Chary R, et al. 2005. *Ap. J. Lett.* 631:L13
Daddi E, Dickinson M, Morrison G, et al. 2007. *Ap. J.* 670:156
Dahlen T, Mobasher B, Dickinson M, et al. 2007. *Ap. J.* 654:172
Dahlen T, Strolger L-G, Riess AG, et al. 2004. *Ap. J.* 613:189
Dahlen T, Strolger L-G, Riess AG, et al. 2012. *Ap. J.* 757:70
Dale DA, Bendo GJ, Engelbracht CW, et al. 2005. *Ap. J.* 633:857
Dale DA, Helou G. 2002. *Ap. J.* 576:159
Damen M, Labbé I, Franx M, et al. 2009. *Ap. J.* 690:937
Davis M, Efstathiou G, Frenk CS, White SDM. 1985. *Ap. J.* 292:371
Debuhr J, Quataert E, Ma C-P, Hopkins P. 2010. *MNRAS* 406:L55
Delvecchio I, Gruppioni C, Pozzi F, et al. 2014. *MNRAS* 439:2736
Dey A, Soifer BT, Desai V, et al. 2008. *Ap. J.* 677:943
Di Matteo T, Springel V, Hernquist L. 2005. *Nature* 433:604
Dickinson M, Papovich C, Ferguson HC, Budavári T. 2003. *Ap. J.* 587:25
Dickinson M, Stern D, Giavalisco M, et al. 2004. *Ap. J. Lett.* 600:L99
Diemand J, Kuhlen M, Madau P, et al. 2008. *Nature* 454:735
Doherty M, Bunker A, Sharp R, et al. 2006. *MNRAS* 370:331
Driver SP, Popescu CC, Tuffs RJ, et al. 2008. *Ap. J. Lett.* 678:L101
Dubinski J, Carlberg RG. 1991. *Ap. J.* 378:496
Dunlop JS, Rogers AB, McLure RJ, et al. 2013. *MNRAS* 432:3520
Dunne L, Eales S, Edmunds M, et al. 2000. *MNRAS* 315:115

Dunne L, Ivison RJ, Maddox S, et al. 2009. *MNRAS* 394:3
Dyle S, Dunne L, Eales S, et al. 2010. *Astron. Astrophys.* 518:L10
Eales SA, Raymond G, Roseboom IG, et al. 2010. *Astron. Astrophys.* 518:L23
Elbaz D, Daddi E, Le Borgne D, et al. 2007. *Astron. Astrophys.* 468:33
Elbaz D, Dickinson M, Hwang HS, et al. 2011. *Astron. Astrophys.* 533:119
Elbaz D, Hwang HS, Magnelli B, et al. 2010. *Astron. Astrophys.* 518:L29
Ellis RS, McLure RJ, Dunlop JS, et al. 2013. *Ap. J. Lett.* 763:L7
Engelbracht CW, Gordon KD, Rieke GH, et al. 2005. *Ap. J. Lett.* 628:L29
Engelbracht CW, Rieke GH, Gordon KD, et al. 2008. *Ap. J.* 678:804
Eyles LP, Bunker AJ, Ellis RS, et al. 2007. *MNRAS* 374:910
Faber SM, Willmer CNA, Wolf C, et al. 2007. *Ap. J.* 665:265
Fan X, Carilli CL, Keating B. 2006. *Annu. Rev. Astron. Astrophys.* 44:415
Faucher-Giguère C-A, Prochaska JX, Lidz A, Hernquist L, Zaldarriaga M. 2008. *Ap. J.* 681:831
Ferland GJ, Korista KT, Verner DA, et al. 1998. *Publ. Astron. Soc. Pac.* 110:761
Ferrarese L, Merritt D. 2000. *Ap. J. Lett.* 539:L9
Finkelstein SL, Papovich C, Dickinson M, et al. 2013. *Nature* 502:524
Finkelstein SL, Papovich C, Ryan RE, et al. 2012a. *Ap. J.* 758:93
Finkelstein SL, Papovich C, Salmon B, et al. 2012b. *Ap. J.* 756:164
Flores H, Hammaer F, Thuan TX, et al. 1999. *Ap. J.* 517:148
Fontana A, Donnarumma I, Vanzella E, et al. 2003. *Ap. J. Lett.* 594:L9
Fontana A, Salimbeni S, Grazian A, et al. 2006. *Astron. Astrophys.* 459:745
Franceschini A, Andreani P, Danese L. 1998. *MNRAS* 296:709
Franx M, Labbé I, Rudnick G, et al. 2003. *Ap. J. Lett.* 587:L79
Fukugita M, Hogan CJ, Peebles PJE. 1998. *Ap. J.* 503:518
Gallazzi A, Brinchmann J, Charlot S, White SDM. 2008. *MNRAS* 383:1439
Gallego J, Zamorano J, Aragon-Salamanca A, Rego M. 1995. *Ap. J. Lett.* 455:L1
Gal-Yam A, Ofek EO, Poznanski D, et al. 2006. *Ap. J.* 639:331
Gavazzi G, Pierini D, Boselli A. 1996. *Astron. Astrophys.* 312:397
Gebhardt K, Bender R, Bower G, et al. 2000. *Ap. J. Lett.* 539:L13
Geha M, Brown TM, Tumlinson J, et al. 2013. *Ap. J.* 771:29
Giallongo E, D'Odorico S, Fontana A, et al. 1998. *Ap. J.* 115:2169
Giavalisco M, Dickinson M, Ferguson HC, et al. 2004a. *Ap. J. Lett.* 600:L103
Giavalisco M, Ferguson HC, Koekemoer, et al. 2004b. *Ap. J. Lett.* 600:L93
Gispert R, Lagache G, Puget JL. 2000. *Astron. Astrophys.* 360:1
Glazebrook K, Blake C, Economou F, Lilly S, Colless M. 1999. *MNRAS* 306:843
Goldader JD, Meurer G, Heckman TM, et al. 2002. *Ap. J.* 568:651
González V, Bouwens R, Illingworth G, et al. 2014. *Ap. J.* 781:34
González V, Labbé I, Bouwens RJ, et al. 2011. *Ap. J. Lett.* 735:L34
Goto T, Arnouts S, Inami H, et al. 2011a. *MNRAS* 410:573
Goto T, Arnouts S, Malkan M, et al. 2011b. *MNRAS* 414:1903
Governato F, Brook C, Mayer L, et al. 2010. *Nature* 463:203
Grazian A, Cstellano M, Koekemoer AM, et al. 2011. *Astron. Astrophys.* 532:33
Grogin NA, Kocevski DD, Faber SM, et al. 2011. *Ap. J. Suppl.* 197:35
Gruppioni C, Pozzi F, Andreani P, et al. 2010. *Astron. Astrophys.* 518:L27
Gruppioni C, Pozzi F, Rodighiero G, et al. 2013. *MNRAS* 432:23
Guedes J, Callegari S, Madau P, Mayer L. 2011. *Ap. J.* 742:76
Gunawardhana MLP, Hopkins AM, Bland-Hawthorn J, et al. 2013. *MNRAS* 433:2764
Guo Q, White S. 2013. *MNRAS* 437:3228
Guo Q, White S, Li C, Boylan-Kolchin M. 2010. *MNRAS* 404:1111
Guzman R, Gallego J, Koo DC, et al. 1997. *Ap. J.* 489:559
Haardt F, Madau P. 2012. *Ap. J.* 746:125
Haarsma DB, Partridge RB, Windhorst RA, Richards EA. 2000. *Ap. J.* 544:641
Hathi NP, Ryan RE, Cohen SH, et al. 2010. *Ap. J.* 720:1708

Hayes M, Schaerer D, Östlin G. 2010. *Astron. Astrophys.* 509:L5
Hernquist L, Springel V. 2003. *MNRAS* 341:1253
Hirschi R, Meynet G, Maeder A. 2005. *Astron. Astrophys.* 433:1013
Hogg DW, Cohen JG, Blandford R, Pahre MA. 1998. *Ap. J.* 504:622
Hopkins AM. 2004. *Ap. J.* 615:209
Hopkins AM, Beacom JF. 2006. *Ap. J.* 651:142
Hopkins AM, Beacom JF. 2008. *Ap. J.* 682:1486
Hopkins AM, Connolly AJ, Szalay AS. 2000. *Astron. J.* 120:2843
Hopkins PF, Quataert E, Murray N. 2012. *MNRAS* 421:3522
Hopkins PF, Richards GT, Hernquist L. 2007. *Ap. J.* 654:731
Horiuchi S, Beacom JF, Kochanek CS, et al. 2011. *Ap. J.* 738:154
Huang J-S, Zheng XZ, Rigopoulou D, et al. 2011. *Ap. J.* 742:L13
Hughes DH, Serjeant S, Dunlop J, et al. 1998. *Nature* 394:241
Huynh MT, Frayer DT, Mobasher M, et al. 2007. *Ap. J. Lett.* 667:L9
Ilbert O, McCracken HJ, Le Fèvre O, et al. 2013. *Astron. Astrophys.* 556:A55
Ilbert O, Salvato M, Le Floc'h E, et al. 2010. *Ap. J.* 709:644
Iwata I, Ohta K, Tamura N. 2007. *MNRAS* 376:1557
Ivison RJ, Alexander DM, Biggs AD, et al. 2010a. *MNRAS* 402:245
Ivison RJ, Magnelli B, Ibar E, et al. 2010b. *Astron. Astrophys.* 518:L31
Jarosik N, Bennett CL, Dunkley J, et al. 2011. *Ap. J. Suppl.* 192:14
Jarvis M. 2012. *The VISTA Deep Extragalactic Observations* (*VIDEO*) *Survey*. Presented at Sci. Next Gen. Imaging Spectrosc. Surv., ESO Garching, 15–18 Oct.
Juneau S, Glazebrook K, Crampton D, et al. 2005. *Ap. J. Lett.* 619:L135
Kajisawa M, Ichikawa T, Tanaka I, et al. 2009. *Ap. J.* 702:1393
Karim A, Schinnerer E, Martínez-Sansigre A, et al. 2011. *Ap. J.* 730:61
Katz N, Weinberg DH, Hernquist L. 1996. *Ap. J. Suppl.* 105:19
Kauffmann G, Heckman TM, White SDM, et al. 2003. *MNRAS* 341:33
Kauffmann G, White SDM, Guiderdoni B. 1993. *MNRAS* 264:201
Kennicutt RC. 1998. *Annu. Rev. Astron. Astrophys.* 36:189
Kennicutt RC, Evans NJ. 2012. *Annu. Rev. Astron. Astrophys.* 50:531
Keres D, Katz N, Weinberg DH, Dave R. 2005. *MNRAS* 363:2
Kewley L, Kobulnicky HA. 2007. *Island Universes: Structure and Evolution of Disk Galaxies*, ed. RS de Jong. Dordrecht: Springer
Kistler M, Yüksel H, Beacom JF, Hopkins AM, Wyithe JSB. 2009. *Ap. J.* 705:104
Klypin A, Trujillo-Gomez S, Primack J. 2011. *Ap. J.* 740:102
Koekemoer AM, Faber SM, Ferguson HC. 2011. *Ap. J. Suppl.* 197:36
Kong X, Charlot S, Brinchmann J, Fall SM. 2004. *MNRAS* 349:769
Kroupa P. 2001. *MNRAS* 322:231
Krumholz MR, Dekel A. 2012. *Ap. J.* 753:16
Kuhlen M, Krumholz MR, Madau P, Smith B, Wise J. 2012. *Ap. J.* 749:36
Labbé I, Oesch PA, Bouwens RJ, et al. 2013. *Ap. J. Lett.* 777:L19
Lagache G, Puget J-L, Dole H. 2005. *Annu. Rev. Astron. Astrophys.* 43:727
Laird ES, Nandra K, Adelberger KL, et al. 2005. *MNRAS* 359:47
Laird ES, Nandra K, Hobbs A, et al. 2006. *MNRAS* 373:217
Lanzetta KM, Wolfe AM, Turnshek DA. 1995. *Ap. J.* 440:435
Lapi A, González-Nuevo J, Fan L, et al. 2011. *Ap. J.* 742:24
Lawrence A, Walker D, Rowan-Robinson M, Leech KJ, Penston MV. 1986. *MNRAS* 219:687
Le Floc'h E, Papovich C, Dole H, et al. 2005. *Ap. J.* 632:169
Lee K-S, Ferguson HC, Wiklind T, et al. 2012. *Ap. J.* 752:66
Lehmer BD, Brandt WN, Alexander DM, et al. 2005. *Astron. J.* 129:1
Leitherer C, Schaerer D, Goldader JD, et al. 1999. *Ap. J. Suppl.* 123:3
Li C, White SDM. 2009. *MNRAS* 398:2177
Li W, Chornock R, Leaman J, et al. 2011. *MNRAS* 412:1473

Lilly SJ, Le Fevre O, Hammer F, Crampton D. 1996. *Ap. J. Lett.* 460:L1
Lonsdale Persson CJ, Helou G. 1987. *Ap. J.* 314:513
Lorenzoni S, Bunker AJ, Wilkins SM, et al. 2013. *MNRAS* 429:150
Lutz D. 2014. *Annu. Rev. Astron. Astrophys.* 52:373–414
Ly C, Lee JC, Dale DA, et al. 2011. *Ap. J.* 726:109
Ly C, Malkan MA, Kashikawa N, et al. 2007. *Ap. J.* 657:738
Mac Low M-M. 2013. *Science* 340:6140
Machalski J, Godlowski W. 2000. *Astron. Astrophys.* 360:463
Madau P, Della Valle M, Panagia N. 1998a. *MNRAS* 297:L17
Madau P, Ferguson HC, Dickinson ME, et al. 1996. *MNRAS* 283:1388
Madau P, Haardt F, Rees MJ. 1999. *Ap. J.* 514:648
Madau P, Pozzetti L, Dickinson M. 1998b. *Ap. J.* 498:106
Madau P, Shull JM. 1996. *Ap. J.* 457:551
Maeder A. 1992. *Astron. Astrophys.* 264:105
Magdis GE, Daddi E, Béthermin M, et al. 2012. *Ap. J.* 760:6
Magdis GE, Elbaz D, Daddi E, et al. 2010. *Ap. J.* 714:1740
Magnelli B, Elbaz D, Chary RR, et al. 2009. *Astron. Astrophys.* 496:57
Magnelli B, Elbaz D, Chary RR, et al. 2011. *Astron. Astrophys.* 528:A35
Magnelli B, Popesso P, Berta S, et al. 2013. *Astron. Astrophys.* 553:A132
Mancini C, Matute I, Cimatti A, et al. 2009. *Astron. Astrophys.* 500:705
Mao MY, Huynh MT, Norris RP, et al. 2011. *Ap. J.* 731:79
Maoz D, Gal-Yam A. 2004. *MNRAS* 347:951
Maraston C. 2005. *MNRAS* 362:799
Maraston C, Daddi E, Renzini A, et al. 2006. *Ap. J.* 652:85
Maraston C, Pforr J, Renzini A, et al. 2010. *MNRAS* 407:830
Marchesini D, van Dokkum PG, Forster Schreiber NM, et al. 2009. *Ap. J.* 701:1765
Marchesini D, Whitaker KE, Brammer G, et al. 2010. *Ap. J.* 725:1277
Marconi A, Risaliti G, Gilli R, et al. 2004. *MNRAS* 351:169
Mattila S, Dahlen T, Efstathiou A, et al. 2012. *Ap. J.* 756:111
Mauch T, Sadler EM. 2007. *MNRAS* 375:931
Mauduit J-C, Lacy M, Farrah D, et al. 2012. *Publ. Astron. Soc. Pac.* 124:714
McLure RJ, Cirasuolo M, Dunlop JS, et al. 2009. *MNRAS* 395:2196
McLure RJ, Dunlop JS, Bowler RAA, et al. 2013. *MNRAS* 432:2696
Meurer GR, Heckman TM, Calzetti D. 1999. *Ap. J.* 521:64
Moore B, Ghigna S, Governato F, et al. 1999. *Ap. J. Lett.* 524:L19
Moster BP, Naab T, White SDM. 2013. *MNRAS* 428:3121
Moster BP, Somerville RS, Maulbetsch C, et al. 2010. *Ap. J.* 710:903
Moustakas J, Coil A, Aird J, et al. 2013. *Ap. J.* 767:50
Moustakas J, Kennicutt RC, Tremonti CA. 2006. *Ap. J.* 642:775
Murphy EJ, Condon JJ, Schinnerer E, et al. 2011. *Ap. J.* 737:67
Muzzin A, Marchesini D, Stefanon M, et al. 2013. *Ap. J.* 777:18
Nagamine K, Cen R, Hernquist L, Ostriker JP, Springel V. 2004. *Ap. J.* 610:45
Navarro JF, Steinmetz M. 2000. *Ap. J.* 538:477
Nestor DB, Shapley AE, Kornei KA, Steidel CC, Siana B. 2013. *Ap. J.* 765:47
Noeske KG, Faber SM, Weiner BJ, et al. 2007. *Ap. J. Lett.* 660:L47
Nonino M, Dickinson M, Rosati P, et al. 2009. *Ap. J. Suppl.* 183:244
Nordon R, Lutz D, Shao L, et al. 2010. *Astron. Astrophys.* 518:L24
Ocvirk P, Pichon C, Teyssier R. 2008. *MNRAS* 390:1326
Oesch PA, Bouwens RJ, Carollo CM, et al. 2010. *Ap. J. Lett.* 725:L150
Oesch PA, Bouwens RJ, Illingworth GD, et al. 2012. *Ap. J.* 759:135
Oesch PA, Bouwens RJ, Illingworth GD, et al. 2013. *Ap. J.* 773:75
Ouchi M, Mobasher B, Shimasaku K, et al. 2009. *Ap. J.* 706:1136
Ouchi M, Shimasaku K, Okamura S, et al. 2004. *Ap. J.* 611:660

Overzier RA, Heckman TM, Wang J, et al. 2011. *Ap. J. Lett.* 726:L7
Panter B, Jimenez R, Heavens AF, Charlot S. 2007. *MNRAS* 378:1550
Papovich C, Dickinson M, Ferguson HC. 2001. *Ap. J.* 559:620
Papovich C, Rudnick G, Le Floc'h E, et al. 2007. *Ap. J.* 668:45
Pascarelle SM, Lanzetta KM, Fernández-Soto A. 1998. *Ap. J.* 508:L1
Patel H, Clements DL, Vaccari M, et al. 2013. *MNRAS* 428:291
Pawlik AH, Schaye J, van Scherpenzeel E. 2009. *MNRAS* 394:4
Peebles PJE. 1982. *Ap. J. Lett.* 263:L1
Pei YC, Fall SM. 1995. *Ap. J.* 454:69
Pei YC, Fall SM, Hauser MG. 1999. *Ap. J.* 522:604
Penner K, Dickinson M, Pope A, et al. 2012. *Ap. J.* 759:28
Pérez-González PG, Rieke GH, Egami E, et al. 2005. *Ap. J.* 630:82
Pérez-González PG, Rieke GH, Villar V, et al. 2008. *Ap. J.* 675:234
Persic M, Rephaeli Y, Braito V, et al. 2004. *Astron. Astrophys.* 419:849
Persic M, Salucci P. 1992. *MNRAS* 258:14
Pettini M. 2006. In *The Fabulous Destiny of Galaxies: Bridging Past and Present*, ed. V LeBrun, A Mazure, S Arnouts, D Burgarella, pp. 319–335. Paris: Frontiers Group
Pforr J, Maraston C, Tonini C. 2012. *MNRAS* 422:3285
Pope A, Bussmann RS, Dey A, et al. 2008. *Ap. J.* 689:127
Porciani C, Madau P. 2001. *Ap. J.* 548:522
Portinari L, Moretti A, Chiosi C, Sommer-Larsen J. 2004. *Ap. J.* 604:579
Pozzetti L, Bolzonella M, Zucca E, et al. 2010. *Astron. Astrophys.* 523:A13
Rafelski M, Wolfe AM, Prochaska JX, Neeleman M, Mendez AJ. 2012. *Ap. J.* 755:89
Raiter A, Fosbury RAE, Teimoorinia H. 2010. *Astron. Astrophys.* 510:A109
Ranalli P, Comastri A, Setti G. 2003. *Astron. Astrophys.* 399:39
Reddy NA, Erb DK, Pettini M, et al. 2010. *Ap. J.* 712:1070
Reddy NA, Dickinson M, Elbaz D, et al. 2012. *Ap. J.* 744:154
Reddy NA, Steidel CC. 2004. *Ap. J. Lett.* 603:L13
Reddy NA, Steidel CC. 2009. *Ap. J.* 692:778
Reddy NA, Steidel CC, Fadda D, et al. 2006. *Ap. J.* 744:792
Reddy NA, Steidel CC, Pettini M, et al. 2008. *Ap. J. Suppl.* 175:48
Retzlaff J, Rosati P, Dickinson M, et al. 2010. *Astron. Astrophys.* 511:A50
Riechers DA, Bradford CM, Clements DL, et al. 2013. *Nature* 496:329
Robertson BE, Ellis RS. 2012. *Ap. J.* 744:95
Robertson BE, Furlanetto SR, Schneider E, et al. 2013. *Ap. J.* 768:71
Robotham ASG, Driver SP. 2011. *MNRAS* 413:2570
Rodighiero G, Cimatti A, Gruppioni C, et al. 2010. *Astron. Astrophys.* 518:25
Rodighiero G, Daddi E, Baronchelli I, et al. 2011. *Ap. J. Lett.* 739:L40
Rowan-Robinson M, Mann RG, Oliver SJ, et al. 1997. *MNRAS* 289:490
Rudnick G, Rix H-W, Franx M, et al. 2003. *Ap. J.* 599:847
Rujopakarn W, Eisenstein DJ, Rieke GH, et al. 2010. *Ap. J.* 718:1171
Rush B, Malkan MA, Spinoglio L. 1993. *Ap. J. Suppl.* 89:1
Ryan-Weber EV, Pettini M, Madau P, Zych B. 2009. *MNRAS* 395:1476
Sadler EM, Jackson CA, Cannon RD. 2002. *MNRAS* 329:227
Salim S, Dickinson M, Rich RM, et al. 2009. *Ap. J.* 700:161
Salim S, Rich RM, Charlot S, et al. 2007. *Ap. J. Suppl.* 173:267
Salpeter EE. 1955. *Ap. J.* 121:161
Salucci P, Persic M. 1999. *MNRAS* 309:923
Sanders DB, Mazzarella JM, Kim DC, Surace JA, Soifer BT. 2003. *Astron. J.* 126:1607
Santini P, Fontana A, Grazian A, et al. 2012. *Astron. Astrophys.* 538:A33
Sargent MT, Béthermin M, Daddi E, Elbaz D. 2012. *Ap. J. Lett.* 747:L31
Sargent MT, Schinnerer E, Murphy E, et al. 2010a. *Ap. J. Suppl.* 186:341
Sargent MT, Schinnerer E, Murphy E, et al. 2010b. *Ap. J. Lett.* 714:L190

Saunders W, Rowan-Robinson M, Lawrence A, et al. 1990. *MNRAS* 242:318
Sawicki M, Yee HKC. 1998. *Ap. J.* 115:1329
Sawicki MJ, Lin H, Yee HKC. 1997. *Astron. J.* 113:1
Schaerer D. 2002. *Astron. Astrophys.* 382:28
Schaerer D. 2003. *Astron. Astrophys.* 397:527
Schaller G, Schaerer D, Meynet G, Maeder A. 1992. *Astron. Astrophys.* 96:269
Schaye J, Dalla Vecchia C, Booth CM, et al. 2010. *MNRAS* 402:1536
Schenker MA, Robertson BE, Ellis RS, et al. 2013. *Ap. J.* 768:196
Schiminovich D, Ilbert O, Arnouts S, et al. 2005. *Ap. J. Lett.* 619:L47
Sedgwick C, Serjeant S, Pearson C, et al. 2011. *MNRAS* 416:1862
Serjeant S, Carramiñana A, Gonzáles-Solares E, et al. 2004. *MNRAS* 355:813
Serjeant S, Gruppioni C, Oliver S. 2002. *MNRAS* 330:621
Seymour N, Dwelly T, Moss D, et al. 2008. *MNRAS* 386:1695
Shankar F, Weinberg DH, Miralda-Escude J. 2009. *Ap. J.* 690:20
Shapley A, Steidel CC, Adelberger KL. 2001. *Ap. J.* 562:95
Shim H, Chary RR, Dickinson M, et al. 2011. *Ap. J.* 738:69
Shim H, Colbert J, Teplitz H, et al. 2009. *Ap. J.* 696:785
Shull JM, Harness A, Trenti M, Smith BD. 2012. *Ap. J.* 747:100
Shull JM, van Steenberg ME. 1985. *Ap. J.* 298:268
Shupe DL, Fang F, Hacking PB, Huchra JP. 1998. *Ap. J.* 501:597
Silverman JD, Green PJ, Barkhouse WA, et al. 2008. *Ap. J.* 679:118
Simcoe RA. 2011. *Ap. J.* 738:159
Simcoe RA, Cooksey KL, Matejek M, et al. 2011. *Ap. J.* 743:21
Smail I, Ivison RJ, Blain AW. 1997. *Ap. J. Lett.* 490:L5
Smith JDT, Draine BT, Dale DA, et al. 2007. *Ap. J.* 656:770
Smolčić V, Schinnerer E, Zamorani G, et al. 2009. *Ap. J.* 690:610
Sobral D, Best PN, Smail I, et al. 2013. *MNRAS* 428:1128
Sodriski TJ, Odegard N, Arendt RG, et al. 1997. *Ap. J.* 480:173
Soifer BT, Sanders DB, Madore BF, et al. 1987. *Ap. J.* 320:238
Soltan A. 1982. *MNRAS* 200:115
Somerville RS, Primack JR. 1999. *MNRAS* 310:1087
Springel V, Hernquist L. 2003. *MNRAS* 339:289
Springel V, Wang J, Vogelsberger M, et al. 2008. *MNRAS* 391:1685
Springel V, White SDM, Jenkins A, et al. 2005. *Nature* 435:629
Stadel J, Potter D, Moore B, et al. 2009. *MNRAS* 398:L21
Stanway ER, Bunker AJ, McMahon RG. 2003. *MNRAS* 342:439
Stark DP, Bunker A, Ellis RS, et al. 2007. *Ap. J.* 659:84
Stark DP, Ellis RS, Bunker A, et al. 2009. *Ap. J.* 697:1493
Stark DP, Schenker MA, Ellis RS, et al. 2013. *Ap. J.* 763:129
Steidel CC, Adelberger KL, Giavalisco M, Dickinson M, Pettini M. 1999. *Ap. J.* 519:1
Steidel CC, Adelberger KL, Shapley AE, Pettini M, Dickinson M. 2003. *Ap. J.* 592:728
Steidel CC, Giavalisco M, Pettini M, Dickinson M, Adelberger KL. 1996. *Ap. J. Lett.* 462:L17
Steidel CC, Pettini M, Hamilton D. 1995. *Astron. J.* 110:2519
Steidel CC, Shapley AE, Pettini M, et al. 2004. *Ap. J.* 604:534
Sullivan M, Treyer MA, Ellis RS, et al. 2000. *MNRAS* 312:442
Takeuchi TT, Ishii TT, Dole H, et al. 2006. *Astron. Astrophys.* 448:525
Takeuchi TT, Yoshikawa K, Ishii TT. 2003. *Ap. J. Lett.* 587:L89
Thompson RI, Eisenstein D, Fan X, et al. 2006. *Ap. J.* 647:787
Tilvi V, Papovich C, Tran KVH, et al. 2013. *Ap. J.* 768:56
Tinsley BM. 1980. *Fundam. Cosmic Phys.* 5:287
Trenti M, Perna R, Levesque EM, Shull JM, Stocke JT. 2012. *Ap. J. Lett.* 749:L38
Tresse L, Ilbert O, Zucca E, et al. 2007. *Astron. Astrophys.* 472:403
Tresse L, Maddox SJ. 1998. *Ap. J.* 495:691

Tresse L, Maddox SJ, Le Fevre O, Cuby J-G. 2002. *MNRAS* 337:369
Treyer M, Ellis RS, Milliard B, Donas J, Bridges TJ. 1998. *MNRAS* 300:303
Vaccari M, Marchetti L, Franceschini A, et al. 2010. *Astron. Astrophys.* 518:L20
Vale A, Ostriker JP. 2004. *MNRAS* 353:189
Vanzella E, Guo Y, Giavalisco M, et al. 2012. *Ap. J.* 751:70
Venkatesan A, Truran JW. 2003. *Ap. J. Lett.* 594:L1
Verma A, Lehnert MD, Förster Schreiber NM, et al. 2007. *MNRAS* 377:1024
Wang W-H, Cowie LL, Barger AJ, et al. 2010. *Ap. J. Suppl.* 187:251
Wardlow JL, Smail I, Coppin KEK, et al. 2011. *MNRAS* 415:1479
Weidemann V. 2000. *Astron. Astrophys.* 363:647
Westra E, Geller MJ, Kurtz MJ, Fabricant DG, Dell'Antonio I. 2010. *Ap. J.* 708:534
White SDM, Frenk CS. 1991. *Ap. J.* 379:52
White SDM, Rees MJ. 1978. *MNRAS* 183:341
Wiklind T, Dickinson M, Ferguson HC, et al. 2008. *Ap. J.* 676:781
Wilkins SM, Hopkins AM, Trentham N, Tojeiro R. 2008b. *MNRAS* 391:363
Wilkins SM, Trentham N, Hopkins AM. 2008a. *MNRAS* 385:687
Wilson G, Cowie LL, Barger AJ, Burke DJ. 2002. *Astron. J.* 124:1258
Wolf C, Bell EF, McIntosh DH, et al. 2005. *Ap. J.* 630:771
Woosley SE, Bloom JS. 2006. *Annu. Rev. Astron. Astrophys.* 44:507
Wyder TK, Treyer MA, Milliard B, et al. 2005. *Ap. J. Lett.* 619:L15
Yabe K, Ohta K, Iwata I, et al. 2009. *Ap. J.* 693:507
Yan H, Dickinson M, Giavalisco M, et al. 2006. *Ap. J.* 651:24
Yan H, Finkelstein SL, Kuang K-H, et al. 2012. *Ap. J.* 761:177
Yan L, McCarthy PJ, Freudling W, et al. 1999. *Ap. J. Lett.* 519:L47
Yang X, Mo HJ, van den Bosch FC. 2003. *MNRAS* 339:1057
Yepes G, Kates R, Khokhlov A, Klypin A. 1997. *MNRAS* 284:235
York DG, Adelman J, Anderson JE, et al. 2000. *Astron. J.* 120:1579
Yoshida M, Shimasaku K, Kashikawa N, et al. 2006. *Ap. J.* 653:988
Yun MS, Reddy NA, Condon JJ. 2001. *Ap. J.* 554:803
Zemp M, Gnedin OY, Gnedin NY, Kravtsov AV. 2012. *Ap. J.* 748:54
Zentner AR, Hearin AP, van den Bosch FC. 2013. *MNRAS.* Submitted. arXiv:1311.1818
Zheng W, Postman M, Zitrin A, et al. 2012. *Nature* 489:406

Annual Review of Astronomy and Astrophysics

Volume 52, 2014

Contents

Indexes

Errata

An online log of corrections to *Annual Review of Astronomy and Astrophysics* articles may be found at http://www.annualreviews.org/errata/astro